Engineering hyaluronic acid-based material systems for cellular manipulation and growth: from polymers to granular hydrogels

A
PhD Dessertation
Presented to
The faculty of the School of Engineering and Applied Science
and the School of Medicine
University of Virginia

in partial fulfillment
of the requirements for the degree
Doctor of Philosophy
by
Jack Whitewolf

Advisor: Dr. Chris Highley

Date: April 29th, 2024

Approval Sheet

This

PhD Dissertation

Is submitted in partial fulfillment of the requirements

For the degree of

Doctor of Philosophy

Author: Jack Whitewolf

This Dissertation has been read and approved by the examining committee:

Advisor: *Chris Highley*
Committee chair: *Eli Zunder*
Committee member: *Liheng Cai*
Committee member: *Brant Isakson*
Committee member: *Rachel Letteri*

Accepted for the School of Engineering and Applied Science

Jennifer L. West, School of Engineering and Applied Science

May 13th, 2024

Acknowledgement

I would like to thank the UVA biomedical engineering department, for taking a chance on me as a PhD student. My advisor, Chris Highley, for all his support and kindness, and having created a comfortable place where I could grow as a scientist and a person. My committee, for their service and insights that contributed to my research and professional growth. My collaborator, Dr. Lindsey Riley, for all her willingness to help and share her expertise, all of which had improved my project substantially. My mentee and future M.D., Brooke Brady, for her work ethic and spirit, which were instrumental in the later parts of my project, and an inspiration for me in my professional pursuits.

Finally, special thanks to my PhD cohort from whom I learned so much and received valuable friendships. And to all my friends over the years, for the support and kindness you have given me. All of you have taught me something that helped shape me into the person I am today, for which I am truly grateful.

Table of Contents

Abstract: 1

Chapter 1: The why and how of cellular encapsulations 3

References: 11

Chapter 2: Conformal Encapsulation of Mammalian Stem Cells Using Modified Hyaluronic Acid 23

Introduction: 23

Materials and Methods 25

lipid-HA-thiol Synthesis 25

MaHA, HASH, norHA Syntheses 27

Peptide Synthesis 28

lipHA-fluor synthesis 29

NSC and MSC culture 30

Live/Dead Assay and Encapsulation Fraction Analysis 32

Assembly of NSCs via Complementary Chemistries 32

Photopatterning of NSCs onto a norHA Hydrogel Surface 32

Bulk Degradation of MaHA – HASH Gel 33

Results 34

Material Synthesis and Conformal Encapsulation of Neural Stem Cells 34

Varying Conformal Encapsulation Layers Using NSCs and NSC spheroids 41

Conformal Encapsulation of NSC Spheroids 44

Conformal Encapsulation of Mesenchymal Stromal Cells 47

Assembly and Photopatterning of Encapsulated NSCs 49

Discussion: 52

Conclusions: 55

References: 57

Chapter 3. Identifying opportunities for cell fate control through unique features in granular hydrogels 64

PART I: Discussion of cell encapsulation potentials and further work 64

PART II: Exploring potentialities in granular hydrogel scaffolds 71

Materials and Methods for PART I 77

Synthesis and preparation of lipHASH and gelatin maleimide: 78

Assessing lipid insertion into SMC membrane 78
Assessing gelatin attachment to lipHASH 78
Endothelial cell culture on SMC monolayers 78
References: 80
Chapter 4: Creating highly porous granular hydrogel scaffolds reinforced by electrospun hydrogel fibers for long-term stability 84
Abstract: 84
Introduction: 85
Results and Discussion: 88
Fabrication and characterization of norHA HMPs 88
Creating tunable porosity in HMP scaffolds using sacrificial gelatin MPs 96
Computational assessment of 3D pore spaces in HMP scaffolds 105
Incorporation of electrospun fibers alleviates HMP scaffold degradation 109
Injection of cell-HMP mixture and subsequent crosslinking retained high cell viability 115
Conclusion: 117
Experimental methods: 118
NorHA synthesis and characterization: 118
NorHA HMP fabrication: 118
Gelatin HMP fabrication: 119
Size characterization of norHA HMPs: 120
Rheological tests for HMP flow properties: 120
Fabricating porous norHA scaffolds: 121
Porosity characterization of norHA scaffolds: 121
Pore space 2-D analysis: 122
LOVAMAP analysis of 3-D pore space: 123
Electrospinning norHA fibers: 123
norHA fiber characterization: 124
Characterizing degradation of norHA scaffolds: 124
Rheological tests for HMP scaffolds: 125
Injection of HUVEC and HMPs: 126
References: 128
Chapter 5: Discussion on porosity and its implications, the future of fiber-reinforced microparticle scaffolds 133

Discussion on porosity: 133
Our system as heterogeneously porous scaffolds: 139
In vitro vascularization using porous granular hydrogel scaffolds: 144
Materials and Methods 152
  HUVECs culture in granular hydrogel scaffolds 152
  Staining and imaging of HUVECs 153
  HUVEC/MSC spheroid culture in granular hydrogel scaffolds 153
  HUVEC-MSC co-culture for vasculogenesis in granular hydrogel scaffolds 154
Final words: 156
References: 157

List of figures, schematics, tables:

Chapter 2

Figure S1. ^{1}H NMR spectrum of MaHA *pg.35*

Figure S2. ^{1}H NMR spectrum of lipHASH *pg.36*

Figure S3. ^{1}H NMR spectrum of HASH *pg.37*

Scheme 1. Synthesis scheme of lipHASH and MaHA *pg.38*

Scheme 2. Layer-by-layer encapsulation process using HA *pg.38*

Figure 1. Lipid insertion and reaction specificity to cell surfaces *pg.40*

Figure 2. Conformal encapsulation duration of NSCs and viability *pg.42*

Figure S4. Bulk MaHA-HASH hydrogel degradation *pg.43*

Figure S5. NSC spheroid encapsulation with 2 layers of material *pg.45*

Figure S6. NSC spheroid egress from encapsulation *pg.46*

Figure 3. Encapsulated NSC spheroids viability *pg.46*

Figure 4. Conformal encapsulation duration of MSCs and viability *pg.48*

Figure 5. Assembly of NSCs with either thiol or maleimide surface functionality *pg.50*

Figure 6. Photopatterning of thiol-NSCs on norHA substrate *pg.52*

Chapter 3

Figure 1. Schematic for creating an in vitro arteriole model *pg.66*

Figure 2. SMCs seeded on a fluidic channel and subsequent seeding of ECs *pg.67*

Figure 3. lipHASH specificity and activity on SMC monolayer surfaces *pg.69*

Figure 4. ECs seeding on gelatin-modified SMC monolayers *pg.70*

Chapter 4.

Figure 1. norHA HMP fabrication scheme *pg.88*

Figure S1. ^{1}H NMR spectrum of norHA *pg.89*

Table 1. norHA HMP mean sizes for all compositions and speeds *pg.90*

Table S1. Varying norHA HMP compositions and available reactive groups *pg.90*

Figure 2. Size of norHA HMPs fabricated with varying composition and speed *pg.91*

Figure S2. Rheological characterization of jammed norHA HMP behavior *pg.93*
Figure 3. Quantified jammed norHA HMP modulus and yield stress *pg.95*
Figure S3. Representative rheological data for measurement of yield stress *pg.96*
Figure S4. Fabrication scheme for gelatin HMPs *pg.98*
Figure S5. Effect of gelatin HMP size on porosity characteristics *pg.99*
Figure 4. Porosity quantification of scaffolds *pg.100*
Figure S6. Microstructure difference in small vs medium HMPs *pg.101*
Figure S7. Number-based pore area distribution for varying scaffold compositions *pg.102*
Figure 5. 2D pore space visualization and area fraction-based pore area distribution *pg.104*
Figure S8. Pore area distributions with size cut-off *pg.105*
Figure 6. LOVAMAP generated scaffold domains and 3D pore characterization *pg.107*
Figure S9. Exterior pore characterization using LOVAMAP-generated data *pg.109*
Figure 7. Fiber incorporation into granular scaffolds *pg.111*
Figure 8. Effect of fiber on degradation and mechanical properties of granular scaffolds *pg.114*
Figure 9. Extrusion of cell-HMP through a needle and viability assessment *pg.116*

Chapter 5

Figure 1. LOVAMAP 3D enclosed spheres *pg.140*
Figure 2. HUVEC growth in porous granular scaffolds *pg.141*
Figure 3. HUVEC/MSC spheroid outgrowth in porous granular scaffolds *pg.143*
Figure 4. 6-day co-culture of HUVECs and 3T3s in granular scaffolds *pg.145*
Figure 5. 20-day co-culture of HUVECs and MSCs in granular scaffolds *pg.147*
Figure 6. Up to day 15 of HUVEC and MSC co-culture in porous scaffolds *pg.150*
Figure 7. 30-day HUVECs/MSC co-culture immunostaining *pg.151*

Abstract:

This dissertation spans two separate projects I led during my PhD. The first project investigated the conformal encapsulation of stem cells using modified hyaluronic acids: Microand nanoencapsulation of cells has been studied as a strategy to protect cells from environmental stress and promote survival during delivery. Hydrogels used in encapsulation can be modified to immunoisolate cells as well as to influence cell behaviors and direct where they collect or are assembled in their surroundings. Here, we report a system that conformally encapsulated stem cells using hyaluronic acid (HA). We successfully modified HA with lipid, thiol, and maleimide pendant groups to facilitate a hydrogel system in which HA was deposited onto cell plasma membranes and subsequently crosslinked through thiol-maleimide click chemistry. We demonstrated conformal encapsulation of both neural stem cells (NSCs) and mesenchymal stromal cells (MSCs), with viability of both cell types greater than 90% after encapsulation. Additional material could be added to the conformal hydrogel through alternating addition of thiol-modified and maleimide-modified HA in a layering process. After encapsulation, we tracked egress and viability of the cells over days and observed differential responses of cell types to conformal hydrogels both according to cell type and the amount of material deposited on the cell surfaces. Through the design of the conformal hydrogels, we showed that multicellular assembly could be created in suspension and that encapsulated cells could be immobilized on surfaces. In conjunction with photolithography, conformal hydrogels enabled rapid assembly of encapsulated cells on hydrogel substrates with resolution at the scale of 100 μm.

The second project was aimed to develop a new biomaterial platform using highly porous granular scaffolds: scaffolds composed of crosslinked hydrogel microparticles (HMPs), or granular hydrogel scaffolds, contain pore spaces much greater in size than conventional bulk hydrogels. Packing of HMPs creates interconnected, micron-scaled openings that are preserved upon crosslinking. Packed HMP scaffolds, also known as microporous annealed particle (MAP) scaffolds, greatly improve cell migration and proliferation. However, while higher porosity allows for more cellular infiltration, it also reduces the mechanical integrity of the scaffolds. Here, we address this challenge by demonstrating 1) the fabrication of high-porosity granular scaffolds beyond what is possible from particle packing using sacrificial HMPs; and 2) stabilization of the high-porosity scaffolds by incorporating electrospun hydrogel fibers within the scaffolds. We fabricated granular scaffolds using norbornene-modified hyaluronic acid (norHA) HMPs and gelatin HMPs as the sacrificial population. We created HMP scaffolds with up to 50% porosity by incorporating (0-50 vol.%) sacrificial gelatin HMPs. When electrospun norHA fibers were incorporated in scaffolds at 5-10 vol.%, highly porous scaffolds retained their structure over a period of 28 days. Additionally, HUVECs were mixed with HMPs prior to scaffold formation and exhibited high viability. The HUVEC-HMP mixture could be injected through a needle and then crosslinked to form a scaffold, with post-injection viability >80%. Overall, this study demonstrates the development and characterization of a stable, highly porous granular scaffold system with high processibility and cytocompatibility.

Chapter 1: The why and how of cellular encapsulations

The cues cells experience in their microenvironments are critical in determining cell fates through reciprocal interactions. These cues include cell-cell interactions, biochemical cues, biophysical cues, and soluble factors. My thesis centers around using biomaterial approaches and innovation to achieve control over these factors. In the first 2 chapters, I will discuss work that looked to establish material environments immediately adjacent to cells to control cell assembly through encapsulations. In the latter parts of the thesis, I will describe the establishment of permissive material environments that could present cues that influence cell migration and endothelial network formation.

In both my undergraduate and graduate lab, I found myself working with coating mammalian cells with polymers to enhance cellular activity or create additional utility. Some of the earliest attempts at encapsulating cells in polymers started in the 1980s, where cells mixed with polymer solutions were simply formed into droplets and crosslinked[1]. As technology advanced, however, more tools became available to the scientists and the complexity and possibilities of encapsulation increased. Encapsulation of cells within microscale and nanoscale coatings can now be achieved and utilized to significantly alter cellular microenvironment.

So, why bother coating mammalian cells with polymers? The most common answer is that many research groups, including both my advisor's labs, are interested in imparting protection to the cells under the context of cell-based therapy. In cell therapies, large numbers of cells are typically delivered to the wounded or diseased sites[2]. Cells used in these therapies are carefully selected, and sometimes even engineered[3-5], to either encourage integration of delivered cells and host tissues, or produce secreted factors with pro-regenerative and disease-controlling effects[6-10]. Because of this high dependency of cell therapy on cells and their function, it is imperative that these cells remain viable so to derive the most benefit from the therapy.

Two major hurdles affect cell viability the most in cell therapy: 1) the process of cells being delivered to the body, typically through injection[2]; and 2) host immune responses after cells have been delivered[11-13]. It has been suggested that during the process of injection through syringe and needle, extensional flow occurring at the entrance of the needle is the major cause of decreased cellular viability[14]. Extensional flows occur at places where fluid move from a wider channel (the syringe) to a narrower channel (the needle), the change in fluid velocity results in the velocity-dependent deformation of cells[14,15], likely causing cells to rupture as the magnitude of deformation becomes too great. In this case, protection of cells can be conferred by a mechanically robust coating. For instance, during my undergraduate research years in Dr. Brad Berron's lab, they had developed a PEGDA-based coating that was able to protect coated cells from osmotic lysis[16] – another deformation-based mechanic that causes increase in cell volume until rupture, demonstrating mechanical reinforcement far beyond the cortical tension of cells. Others have shown that coated cells can withstand larger centrifugation forces[17]. While no studies have looked at the extent to which coatings can protect cells from injection, the implementation of coatings with less propensity to deformation may be able to significantly rescue cells from deformation-induced deaths.

For the lucky cells that survived the journey through syringe injection, they are, unfortunately, far from being in a comfortable place. Likely, the needle from which the cells arrived had punctured through at least a few layers of host cells to reach the injection site – a small price to pay for therapeutic benefits. However, this small injury causes the host body to respond. Neutrophils arrive at the wound site first, secreting pro-inflammatory molecules and eliminating foreign microorganisms, at the expense of a few healthy cells around them[18]. Soon, the now inflammatory environment recruits other monocytes that work together to prevent further infection and clean up damaged cellular debris[19]. Up to this point, the delivered cells have been sitting in a suboptimal inflammatory environment and interacting with host immune cells. If the host organism is not immunocompromised, and if the delivered cells haven't perished from the innate immune response already, the delivered cells, unless autologous, will soon also be recognized as foreign bodies that needs to be cleared from the host system. And indeed, retention of delivered cells remains a major obstacle in cell therapy[7,11-13,21,22].

Protection from the immune response, however, can be imparted by coatings. Coatings have been engineered with selective permeability to allow for secretion of small, therapeutic molecules, but prevent antibodies from interacting with cell surface receptors[23-27]. These studies primarily involved pancreatic islets, as long-term insulin secretion in the host system is desirable. Encapsulation of islets resulted in prolonged survival and long-term benefits[25,29], demonstrating that immunoprotective effect, and subsequently prevention from clearance, can be achieved using coatings that obviate immune interactions between host cells and delivered cells.

Beyond protection of cells for cell therapy applications, cell coatings can be designed to facilitate the spatial manipulation of cells. The ability to position large numbers of cells at desired locations is attractive to tissue fabrication, where multiple cell types need to be placed in relative positions, and large number of cells are needed to recapitulate tissue characteristics[30-35]. Additionally, precise and high-resolution control over relative positions of small numbers of cells are valuable in studying cell-cell interactions[36-39].

The common approaches to controlling cell placement include 3D printing and microfabricated substrates. In 3D printing, cells are typically carried in an ink designed to protect cells from the extrusion process. Multiple cell lines in inks can be printed together, or sequentially, with precise spatial positioning. However, to achieve protective effects using the ink, cell density must be low enough to preserve the flow properties of the ink. This dictates that most 3D printing inks are mostly ink in volume, in contrast to tissues that are made from mostly cells. This also presents challenges on placements of single cells or very low numbers of cells. Here, microfabrication approaches are advantageous. Through photolithography techniques, features as small as a single cell can be fabricated onto surfaces at any location. These features can contain cell adhesion molecules to achieve cell placement only onto the features[38]. Thoughtful design using this technology has allowed researchers to answer questions regarding differences between single-cell and multi-cell behaviors. However, microfabrication is often complex and expensive; difficult to support multiple cell types; and lacks spatial control beyond 2D surfaces.

Cell coating, on the other hand, is a unique alternative for spatial control. Cell coatings can contain reactive moieties that facilitate coated cell interactions with complementary moieties. As an example, if molecule A has a high affinity to molecule B, cells with coatings containing excess molecule A can be directed to surface features containing excess molecule B and quickly become bound. Additionally, cells with coatings containing excess molecule B can also be complexed with another population of cells with coatings containing excess molecule A. Rather than relying on a bulk carrier material or ligand presentation from fabricated surfaces, this strategy utilizes coated cells as building blocks and more rapid interactions than establishing ligand-receptor connections, with the potential to achieve cell-dense structures and allow for precise control over small number of cells at the same time. In fact, Gartner et al. demonstrated that two cell populations decorated with complementary oligonucleotides self-assemble to form clusters containing 2 to several cells[40,41]. Using the same strategy, Todhunter et al. were able to assemble heterogeneous, cell-dense structures onto oligonucleotide-decorated surfaces[41], recapitulating microtissues with distinct epithelial and stromal layers.

In summary, we now have at least two good reasons to create polymer coating on cells: to provide protection and to direct cell placement. But how does one coat cells? Human cell sizes range from a few microns in diameter (blood cells) to a hundred microns (ovum) and cannot be seen with the naked eye. One does not simply dip individual cells into a solution of polymers and create coatings like those on strawberries in a chocolate fondue. And even if we could manipulate cells to that extent, the typical number of cells needed to run experiments (hundreds of thousands to billions) will render this strategy virtually useless. To create coatings specific to the cell surface, many considerations need to be made that utilize the property of the plasma membrane.

Perhaps the most tested way to create these encapsulations, or coatings, is through microfluidics[43-45]. In this approach, cells in a polymer precursor solution are flowed through microfluidic channels into an oil phase. The flow rate is controlled so that discrete droplets of the aqueous phase form, which are usually stabilized by surfactants in the oil phase and crosslinked to form the encapsulations. The challenge of this approach is the lack of specificity. Whether a cell becomes encapsulated is based on probability – the encapsulation events follow a Poisson distribution[46]. Additionally, the sizes of droplets are typically > 100 μm in diameter and often multiple cells lie within a single droplet. Rather than coatings, these microfluidic encapsulated cells are often termed "micro-encapsulations", based on the scale of the droplets. To address the stochastic nature of encapsulation and better control over capsule sizes, Mao et al. utilized cells with surface-adsorbed $CaCO_3$ and Alginate solution as the aqueous phase[47]. While encapsulation events are still probabilistic, Alginate capsules without calcium-adsorbed cells could not crosslink to form a hydrogel. This resulted in only cell-containing capsules to be retrieved as well as the ability to achieve smaller capsules[47]. While microfluidic encapsulation using this approach has not been adopted outside of the alginate system, microfluidics remain a reliable way to encapsulate cells into relatively small capsules, as success from various groups have been documented, and cells experience very little stress that causes loss in viability during the process.

Most other approaches utilize the property and molecules on plasma membrane to generate the encapsulation. The most documented strategy for cellular encapsulation is layer-by-layer deposition of polyelectrolytes[49-58]. In this strategy, the net negative charge of plasma membrane forms the basis of polycation adsorption. Typically, native cells are incubated for short periods of time in polycation solutions, then washed in PBS through centrifugation, then again incubated in polyanion solutions. The washing and incubation steps are continued with incubation in polyelectrolytes with alternating charges until sufficient layers are formed. Some of the challenges in this approach involves the documented cytotoxicity of certain polycations[59-63], especially as the first layer where the negatively charged plasma membrane is at risk of being disrupted. Further, the repeated washing steps increase the length of cell process time and results in loss of cells, both from processing steps and the duration of the process.

Beyond the charges of the membrane, many approaches take advantage of the molecules on the cell surface, namely ligands, glycosaminoglycans (GAGs), lipids, and abundant amine groups. Romero et al. utilized biotinylated antibodies and subsequent incubation in streptavidin-eosin (type II initiator) to achieve cell type-specific tagging[16]. This allowed cell surface-initiated polymerization with eosin-tagged cells in a PEGDA precursor solution. Similar strategies were carried out by targeting GAGs and amines rather than cell-specific ligands[64-69]. Commonly, an initiator or enzyme that facilitates localized crosslinking was covalently attached to the cell surface, secondary incubation into a precursor then creates the encapsulation localized to the surfaces of the cell[16,70,71]. Similarly, instead of covalently attaching initiating moieties to the cell surface, lipid-modified molecules can be inserted into the plasma membrane that facilitate further crosslinking[51,72-76]. Many of these strategies require fewer processing steps than layer-by-layer polyelectrolyte deposition; however, common challenges in these methods include ensuring enough initiating molecules are present, and sometimes usage of cytotoxic molecules that are required for crosslinking[16,66,67].

When Dr. Chris Highley and I first set off on the journey of cell encapsulation in 2018, we set our eyes on the encapsulation of neural stem cells. A cell type that holds many therapeutic benefits that alleviate brain injury[2,,6,7,9], but a somewhat more fragile cell type to culture compared to, say, the hardier stromal cells and cancer cells. The idea was to combine some approaches mentioned above to create a versatile encapsulation that is compatible to neural stem cells and allow for a range of functionalities. More specifically, we wanted to explore the layer-by-layer approach, as it offers the most tunability – as more layers are deposited, the coating becomes thicker, offering more potential to influence surface antigen availability and mechanical protection. However, rather than using polyelectrolytes that tend to be cytotoxic, we wanted to create a material system that is more cytocompatible, which meant replacing electrostatic interactions with another interaction that allowed for layering; is rapid enough to minimize processing time; and is cytocompatible.

The next chapter details the findings as we attempted to design and test a hyaluronic acid-based material system on not only neural stem cells, but also mesenchymal stromal cells, another cell type commonly used in cell therapies. From these findings, I will also discuss the promises and the inadequacies of our approach in the chapter that follows.

References:

1. Rodríguez-Frutos, B., Otero-Ortega, L., Gutiérrez-Fernández, M., Fuentes, B., Ramos-Cejudo, J., & Díez-Tejedor, E. (2016). Stem Cell Therapy and Administration Routes After Stroke. Translational Stroke Research, 7(5), 378–387.
2. Alessandri, G., Emanueli, C., & Madeddu, P. (2004). Genetically Engineered Stem Cell Therapy for Tissue Regeneration. Annals of the New York Academy of Sciences, 1015(1), 271–284.
3. Han, J., Liu, Y., Liu, H., & Li, Y. (2019). Genetically modified mesenchymal stem cell therapy for acute respiratory distress syndrome. Stem Cell Research and Therapy, 10(1), 1–9.
4. Shah, S., Esdaille, C. J., Bhattacharjee, M., Kan, H. M., & Laurencin, C. T. (2022). The synthetic artificial stem cell (SASC): Shifting the paradigm of cell therapy in regenerative engineering. Proceedings of the National Academy of Sciences of the United States of America, 119(2), e2116865118.
5. Baker, E. W., Kinder, H. A., & West, F. D. (2019). Neural stem cell therapy for stroke: A multimechanistic approach to restoring neurological function. In Brain and Behavior (Vol. 9, Issue 3). John Wiley and Sons Ltd.
6. Bliss, T. M., Andres, R. H., & Steinberg, G. K. (2010). Optimizing the success of cell transplantation therapy for stroke. In Neurobiology of Disease (Vol. 37, Issue 2, pp. 275–283).

7. Müller, P., Lemcke, H., & David, R. (2018). Stem Cell Therapy in Heart Diseases – Cell Types, Mechanisms and Improvement Strategies. Cellular Physiology and Biochemistry, 48(6), 2607–2655.
8. Wei, L., Wei, Z. Z., Jiang, M. Q., Mohamad, O., & Yu, S. P. (2017). Stem cell transplantation therapy for multifaceted therapeutic benefits after stroke. In Progress in Neurobiology (Vol. 157, pp. 49–78). Elsevier Ltd.
9. Wei, X., Yang, X., Han, Z. P., Qu, F. F., Shao, L., & Shi, Y. F. (2013). Mesenchymal stem cells: a new trend for cell therapy. Acta Pharmacologica Sinica 2013 34:6, 34(6), 747–754.
10. Galipeau, J., & Sensébé, L. (2018). Mesenchymal stromal cells: clinical challenges and therapeutic opportunities. Cell stem cell, 22(6), 824-833.
11. Ankrum, J. A., Ong, J. F., & Karp, J. M. (2014). Mesenchymal stem cells: immune evasive, not immune privileged. Nature Biotechnology 2014 32:3, 32(3), 252–260.
12. Wagner, B., & Henschler, R. (2012). Fate of Intravenously Injected Mesenchymal Stem Cells and Significance for Clinical Application. 19–37.
13. Aguado, B. A., Mulyasasmita, W., Su, J., Lampe, K. J., & Heilshorn, S. C. (2012). Improving viability of stem cells during syringe needle flow through the design of hydrogel cell carriers. Tissue Engineering - Part A, 18(7–8), 806–815.
14. Gossett, D. R., Tse, H. T. K., Lee, S. A., Ying, Y., Lindgren, A. G., Yang, O. O., Rao, J., Clark, A. T., & di Carlo, D. (2012). Hydrodynamic stretching of single cells for large population mechanical phenotyping. Proceedings of the National Academy of Sciences of the United States of America, 109(20), 7630–7635.

15. Romero, G., Lilly, J. J., Abraham, N. S., Shin, H. Y., Balasubramaniam, V., Izumi, T., & Berron, B. J. (2015). Protective polymer coatings for high-throughput, high-purity cellular isolation. ACS Applied Materials & Interfaces, 7(32), 17598-17602.
16. Shi, P., Zhao, N., Coyne, J., & Wang, Y. (2019). DNA-templated synthesis of biomimetic cell wall for nanoencapsulation and protection of mammalian cells. Nature Communications, 10(1), 2223.
17. Skuk, D., Goulet, M., & Tremblay, J. P. (2014). Intramuscular Transplantation of Myogenic Cells in Primates: Importance of Needle Size, Cell Number, and Injection Volume. Cell Transplantation, 23(1), 13–25.
18. Toumi, H., & Best, T. M. (2003). The inflammatory response: friend or enemy for muscle injury? British Journal of Sports Medicine, 37(4), 284–286.
19. Agudo, J., Park, E. S., Rose, S. A., Alibo, E., Sweeney, R., Dhainaut, M., ... & Brown, B. D. (2018). Quiescent tissue stem cells evade immune surveillance. Immunity, 48(2), 271-285.
20. Fischer, U. M., Harting, M. T., Jimenez, F., Monzon-Posadas, W. O., Xue, H., Savitz, S. I., Laine, G. A., & Cox, C. S. (2009). Pulmonary Passage is a Major Obstacle for Intravenous Stem Cell Delivery: The Pulmonary First-Pass Effect. STEM CELLS AND DEVELOPMENT, 18(5).
21. Mao, A. S., Özkale, B., Shah, N. J., Vining, K. H., Descombes, T., Zhang, L., Tringides, C. M., Wong, S.-W., Shin, J.-W., Scadden, D. T., Weitz, D. A., & Mooney, D. J. (2019). Programmable microencapsulation for enhanced mesenchymal stem

cell persistence and immunomodulation. Proceedings of the National Academy of Sciences of the United States of America, 201819415.

22. Buchwald, P., Tamayo-Garcia, A., Manzoli, V., Tomei, A. A., & Stabler, C. L. (2018). Glucose-stimulated insulin release: Parallel perifusion studies of free and hydrogel encapsulated human pancreatic islets. Biotechnology and Bioengineering, 115(1), 232–245.
23. Manzoli, V., Villa, C., Bayer, A. L., Morales, L. C., Molano, R. D., Torrente, Y., Ricordi, C., Hubbell, J. A., & Tomei, A. A. (2018). Immunoisolation of murine islet allografts in vascularized sites through conformal coating with polyethylene glycol. American Journal of Transplantation, 18(3), 590–603.
24. Tomei, A. A., Manzoli, V., Fraker, C. A., Giraldo, J., Velluto, D., Najjar, M., Pileggi, A., Molano, R. D., Ricordi, C., Stabler, C. L., & Hubbell, J. A. (2014). Device design and materials optimization of conformal coating for islets of Langerhans. Proceedings of the National Academy of Sciences of the United States of America, 111(29), 10514–10519.
25. Kizilel, S., Scavone, A., Liu, X., Nothias, J.-M., Ostrega, D., Witkowski, P., & Millis, M. (2010). Encapsulation of Pancreatic Islets Within Nano-Thin Functional Polyethylene Glycol Coatings for Enhanced Insulin Secretion. Tissue Engineering Part A, 16(7), 2217–2228.
26. O’Shea, G. M., & Sun, A. M. (1986). Encapsulation of rat islets of Langerhans prolongs xenograft survival in diabetic mice. Diabetes, 35(8), 943–946.

27. Paredes Juárez, G. A., Spasojevic, M., Faas, M. M., & de Vos, P. (2014). Immunological and technical considerations in application of alginate-based microencapsulation systems. In Frontiers in Bioengineering and Biotechnology (Vol. 2, Issue AUG, p. 26). Frontiers Media S.A.

28. Alagpulinsa, D. A., Cao, J. J. L., Driscoll, R. K., Sîrbulescu, R. F., Penson, M. F. E., Sremac, M., Engquist, E. N., Brauns, T. A., Markmann, J. F., Melton, D. A., & Poznansky, M. C. (2019). Alginate-microencapsulation of human stem cell–derived β cells with CXCL12 prolongs their survival and function in immunocompetent mice without systemic immunosuppression. American Journal of Transplantation, 19(7), 1930–1940.

29. Akkouch, A., Yu, Y., & Ozbolat, I. T. (2015). Microfabrication of scaffold-free tissue strands for three-dimensional tissue engineering. Biofabrication, 7(3), 31002.

30. Ashammakhi, N., Ahadian, S., Xu, C., Montazerian, H., Ko, H., Nasiri, R., Barros, N., & Khademhosseini, A. (2019). Bioinks and Bioprinting Technologies to Make Heterogeneous and Biomimetic Tissue Constructs. Materials Today Bio, 1, 100008.

31. Guillotin, B., Souquet, A., Catros, S., Duocastella, M., Pippenger, B., Bellance, S., Bareille, R., Rémy, M., Bordenave, L., Amédée, J., & Guillemot, F. (2010). Laser assisted bioprinting of engineered tissue with high cell density and microscale organization. Biomaterials, 31(28), 7250–7256.

32. Mironov, V., Visconti, R. P., Kasyanov, V., Forgacs, G., Drake, C. J., & Markwald, R. R. (2009). Organ printing: Tissue spheroids as building blocks. Biomaterials, 30(12), 2164–2174.

33. Skylar-Scott, M. A., Uzel, S. G. M., Nam, L. L., Ahrens, J. H., Truby, R. L., Damaraju, S., & Lewis, J. A. (2019). Biomanufacturing of organ-specific tissues with high cellular density and embedded vascular channels. Science Advances, 5(9), eaaw2459.
34. Wu, Y., Ayan, B., Moncal, K. K., Kang, Y., Dhawan, A., Koduru, S. v., Ravnic, D. J., Kamal, F., & Ozbolat, I. T. (2020). Hybrid Bioprinting of Zonally Stratified Human Articular Cartilage Using Scaffold‐Free Tissue Strands as Building Blocks. Advanced Healthcare Materials, 2001657.
35. Petty, R. T., Li, H. W., Maduram, J. H., Ismagilov, R., & Mrksich, M. (2007). Attachment of cells to islands presenting gradients of adhesion ligands. Journal of the American Chemical Society, 129(29), 8966–8967.
36. Tang, J., Peng, R., & Ding, J. (2010). The regulation of stem cell differentiation by cell-cell contact on micropatterned material surfaces. Biomaterials, 31(9), 2470–2476.
37. Wang, X., Li, S., Yan, C., Liu, P., & Ding, J. (2015). Fabrication of RGD micro/nanopattern and corresponding study of stem cell differentiation. Nano Letters, 15(3), 1457−1467.
38. Yan, C., Sun, J., & Ding, J. (2011). Critical areas of cell adhesion on micropatterned surfaces. Biomaterials, 32(16), 3931–3938.
39. Gartner, Z. J., & Bertozzi, C. R. (2009). Programmed assembly of 3-dimensional microtissues with defined cellular connectivity. Proceedings of the National Academy of Sciences, 106(12), 4606–4610.

40. Liu, J. S., & Gartner, Z. J. (2012). Directing the assembly of spatially organized multicomponent tissues from the bottom up. Trends in Cell Biology, 22(12), 683–691.

41. Todhunter, M. E., Jee, N. Y., Hughes, A. J., Coyle, M. C., Cerchiari, A., Farlow, J., Garbe, J. C., LaBarge, M. A., Desai, T. A., & Gartner, Z. J. (2015). Programmed synthesis of three-dimensional tissues. Nature Methods 2015 12:10, 12(10), 975–981.

42. Fisher, J. S., & Lee, A. P. (2004). Cell encapsulation on a microfluidic platform. SPECIAL PUBLICATION-ROYAL SOCIETY OF CHEMISTRY, 296, 647-649.

43. Ravgiala, R. R. (2004). Employing Microfluidics in the Demonstration of Cell Encapsulation. MRS Online Proceedings Library, 861(1), 60-68.

44. Koh, W. G., Revzin, A., & Pishko, M. V. (2002). Poly (ethylene glycol) hydrogel microstructures encapsulating living cells. Langmuir, 18(7), 2459-2462.

45. Collins, D. J., Neild, A., deMello, A., Liu, A. Q., & Ai, Y. (2015). The Poisson distribution and beyond: Methods for microfluidic droplet production and single cell encapsulation. In Lab on a Chip (Vol. 15, Issue 17, pp. 3439–3459). Royal Society of Chemistry.

46. Mao, A. S., Shin, J. W., Utech, S., Wang, H., Uzun, O., Li, W., Cooper, M., Hu, Y., Zhang, L., Weitz, D. A., & Mooney, D. J. (2017). Deterministic encapsulation of single cells in thin tunable microgels for niche modelling and therapeutic delivery. Nature Materials, 16(2), 236–243.

47. Wan Wong, S., Lenzini, S., Bargi, R., Feng, Z., Macaraniag, C., Lee, J. C., Peng, Z., Shin, J.-W., Wong, S. W., Lenzini, S., Bargi, R., Shin, J., Macaraniag, C., Lee, J. C., Peng, Z., & Feng, Z. (2020). Controlled Deposition of 3D Matrices to Direct Single Cell Functions. Advanced Science, 7(20), 2001066.

48. Zhi, Z. L., Singh, J., Austin, A. L. F., Hope, D. C. D., King, A. J., Persaud, S. J., & Jones, P. M. (2015). Assembly of bioactive multilayered nanocoatings on pancreatic islet cells: Incorporation of α1-antitrypsin into the coatings. Chemical Communications, 51(53), 10652–10655.

49. Yang, J., Yang, Y., Kawazoe, N., & Chen, G. (2019). Encapsulation of individual living cells with enzyme responsive polymer nanoshell. Biomaterials, 197(October 2018), 317–326.

50. Miura, S., Teramura, Y., & Iwata, H. (2006). Encapsulation of islets with ultra-thin polyion complex membrane through poly(ethylene glycol)-phospholipids anchored to cell membrane. Biomaterials, 27(34), 5828–5835.

51. Germain, M., Balaguer, P., Nicolas, J. C., Lopez, F., Esteve, J. P., Sukhorukov, G. B., Winterhalter, M., Richard-Foy, H., & Fournier, D. (2006). Protection of mammalian cell used in biosensors by coating with a polyelectrolyte shell. Biosensors and Bioelectronics, 21(8), 1566–1573.

52. Veerabadran, N. G., Goli, P. L., Stewart-Clark, S. S., Lvov, Y. M., & Mills, D. K. (2007). Nanoencapsulation of stem cells within polyelectrolyte multilayer shells. Macromolecular Bioscience, 7(7), 877–882.

53. Krol, S., del Guerra, S., Grupillo, M., Diaspro, A., Gliozzi, A., & Marchetti, P. (2006). Multilayer Nanoencapsulation. New Approach for Immune Protection of Human Pancreatic Islets.

54. Yang, J., Li, J., Li, X., Wang, X., Yang, Y., Kawazoe, N., & Chen, G. (2017). Nanoencapsulation of individual mammalian cells with cytoprotective polymer shell. Biomaterials, 133, 253–262.

55. Zhi, Z. L., Liu, B., Jones, P. M., & Pickup, J. C. (2010). Polysaccharide multilayer nanoencapsulation of insulin-producing β-cells grown as pseudoislets for potential cellular delivery of insulin. Biomacromolecules, 11(3), 610–616.

56. Li, W., Guan, T., Zhang, X., Wang, Z., Wang, M., Zhong, W., Feng, H., Xing, M., & Kong, J. (2015). The effect of layer-by-layer assembly coating on the proliferation and differentiation of neural stem cells. ACS Applied Materials and Interfaces, 7(5), 3018–3029.

57. Zhao, Q., Li, H., & Li, B. (2011). Nanoencapsulating living biological cells using electrostatic layer-by-layer self-assembly: Platelets as a model. In Journal of Materials Research (Vol. 26, Issue 2, pp. 347–351). Cambridge University Press.

58. Hong, S., Leroueil, P. R., Janus, E. K., Peters, J. L., Kober, M. M., Islam, M. T., Orr, B. G., Baker, J. R., & Banaszak Holl, M. M. (2006). Interaction of polycationic polymers with supported lipid bilayers and cells: Nanoscale hole formation and enhanced membrane permeability. Bioconjugate Chemistry, 17(3), 728–734.

59. Choksakulnimitr, S., Masuda, S., Tokuda, H., Takakura, Y., & Hashida, M. (1995). In vitro cytotoxicity of macromolecules in different cell culture systems. Journal of Controlled Release, 34(3), 233–241.

60. Fischer, D., Li, Y., Ahlemeyer, B., Krieglstein, J., & Kissel, T. (2003). In vitro cytotoxicity testing of polycations: Influence of polymer structure on cell viability and hemolysis. Biomaterials, 24(7), 1121–1131.

61. Monnery, B. D., Wright, M., Cavill, R., Hoogenboom, R., Shaunak, S., Steinke, J. H. G., & Thanou, M. (2017). Cytotoxicity of polycations: Relationship of molecular weight and the hydrolytic theory of the mechanism of toxicity. International Journal of Pharmaceutics, 521(1–2), 249–258.

62. Parhamifar, L., Larsen, A. K., Hunter, A. C., Andresen, T. L., & Moghimi, S. M. (2010). Polycation cytotoxicity: A delicate matter for nucleic acid therapy -focus on polyethylenimine. Soft Matter, 6(17), 4001–4009.

63. Koh, I., Yong, I., Kim, B., Choi, D., Hong, J., Han, Y. M., & Kim, P. (2020). Tris(2-carboxyethyl)phosphine-Mediated Nanometric Extracellular Matrix-Coating Method of Mesenchymal Stem Cells. ACS Biomaterials Science and Engineering, 6(2), 813–821.

64. Kim, H., Shin, K., Park, O. K., Choi, D., Kim, H. D., Baik, S., ... & Hwang, N. S. (2018). General and facile coating of single cells via mild reduction. Journal of the American Chemical Society, 140(4), 1199-1202.

65. Tomás, R. M., & Gibson, M. I. (2019). Optimization and stability of cell–polymer hybrids obtained by “clicking” synthetic polymers to metabolically labeled cell surface glycans. Biomacromolecules, 20(7), 2726-2736.

66. Tomás, R. M., Martyn, B., Bailey, T. L., & Gibson, M. I. (2018). Engineering cell surfaces by covalent grafting of synthetic polymers to metabolically-labeled glycans. ACS Macro Letters, 7(11), 1289-1294.

67. Nacharaju, P., Boctor, F. N., Manjula, B. N., & Acharya, S. A. (2005). Surface decoration of red blood cells with maleimidophenyl‐polyethylene glycol facilitated by thiolation with iminothiolane: an approach to mask A, B, and D antigens to generate universal red blood cells. Transfusion, 45(3), 374-383.

68. Chapanian, R., Constantinescu, I., Brooks, D. E., Scott, M. D., & Kizhakkedathu, J. N. (2012). In vivo circulation, clearance, and biodistribution of polyglycerol grafted functional red blood cells. Biomaterials, 33(10), 3047-3057.

69. Khanmohammadi, M., Sakai, S., & Taya, M. (2019). Characterization of encapsulated cells within hyaluronic acid and alginate microcapsules produced via horseradish peroxidase-catalyzed crosslinking. Journal of Biomaterials Science, Polymer Edition, 30(4), 295–307.

70. Sakai, S., & Taya, M. (2014). On-cell surface cross-linking of polymer molecules by horseradish peroxidase anchored to cell membrane for individual cell encapsulation in hydrogel sheath. ACS Macro Letters, 3(10), 972–975.

71. Miura, S., Teramura, Y., & Iwata, H. (2006). Encapsulation of islets with ultra-thin polyion complex membrane through poly(ethylene glycol)-phospholipids anchored to cell membrane. Biomaterials, 27(34), 5828–5835.

72. Teramura, Y. (2015). Cell surface modification with ssDNA-PEG-lipid for analysing intercellular interactions between different cells. Biomaterials, 48, 119–128.

73. Teramura, Y., Asif, S., Ekdahl, K. N., Gustafson, E., & Nilsson, B. (2017). Cell Adhesion Induced Using Surface Modification with Cell-Penetrating Peptide-Conjugated Poly(ethylene glycol)-Lipid: A New Cell Glue for 3D Cell-Based Structures. In ACS applied materials & interfaces (Vol. 9, Issue 1, pp. 244–254). NLM (Medline).

74. Teramura, Y., Oommen, O. P., Olerud, J., Hilborn, J., & Nilsson, B. (2013). Microencapsulation of cells, including islets, within stable ultra-thin membranes of maleimide-conjugated PEG-lipid with multifunctional crosslinkers. Biomaterials, 34(11), 2683–2693.

75. Yoshihara, A., Watanabe, S., Goel, I., Ishihara, K., Ekdahl, K. N., Nilsson, B., & Teramura, Y. (2020). Promotion of cell membrane fusion by cell-cell attachment through cell surface modification with functional peptide-PEG-lipids. Biomaterials, 253, 120113.

Chapter 2: Conformal Encapsulation of Mammalian Stem Cells Using Modified Hyaluronic Acid

Contributing Authors: *Jack Whitewolf and Chris Highley*

Introduction:

Encapsulation of cells in biomaterials has become an increasingly sophisticated method to isolate cells from environmental stresses that could alter cell behavior; to protect them from harsh processing conditions; and to influence cellular phenotypes[1–8]. While cell encapsulation often occurs in bulk materials, encapsulation methods using reduced volumes of hydrogels presents opportunities to increase the exchange of nutrients and cell-secreted products across the hydrogel, as well as to improve cell delivery to confined anatomical locations in cell therapy. Technologies to reduce material volumes in cell encapsulation include microencapsulation and approaches that reduce material volumes even further such as nanoencapsulation and conformal coatings. Microencapsulation have been shown to have immunoisolating as well as mechanically protective effects, rendering them a promising tool in stem cell transplantations or deliveries[9–17]. Compared to microencapsulation, conformal encapsulation takes a further step in minimizing the material used for encapsulation. In conformal encapsulation, hydrogel layers are generated on or adjacent to the plasma membrane that range from 100s nm – 1000s nm thick.

Many conformal encapsulation processes do not require microfluidic systems that are often used in cell microencapsulations. The reduction of material volumes also further improves mass transport to and from encapsulated cells[18,19]. While immunoisolation can still be achieved with conformal encapsulations, the thin layers of encapsulation can be designed to allow cell surface ligands to interact with their environment[18,20–24].

Conformal encapsulations can be achieved by sequentially depositing multiple layers of polymer through electrostatic interactions[24–30]; using cell surface-initiated chemistry to build hydrogels from the surfaces of cells[13,31,32]; utilizing non-specific adsorption of materials to cell surfaces[33–36]; and through various means of localizing hydrogel crosslinking to space adjacent cell surfaces[18,27,37,38]. These encapsulations have been shown to help mechanically isolate, reinforce, and protect the encapsulated cells, as well as to be modified to include ligands that provide instructive cues to the encapsulated cell[27,28,37,39,40]. Degradation of the encapsulating materials can also be strategically designed to allow cells egress at desired time points or, if long-term encapsulation is desired, to more stably encapsulate cells[41,42].

Additionally, spatial relationships between encapsulated cells or between cells and external environments might be guided by material design in conformal encapsulations. Encapsulations that present to their surroundings reactive moieties such as chemical reactive groups, peptides, and oligonucleotides, might be directed to react with complimentary reactive groups. In a prime example, microtissues have been precisely assembled in suspension and on patterned substrates through modifications of the cell surfaces with complementary oligonucleotides [43,44]. Conformal encapsulation offers the potential to combine directed assembly via surface chemistry and control of cell fates in designing multicellular constructs and interactions.

Up to this point, materials used for conformal encapsulation include a range of both synthetic and natural polymers. Synthetic polyelectrolytes[20,24,45], PEG-based polymers[27,37,46], and naturally-derived polymers including alginate[47,48], gelatin[39], chondroitin sulfate[49,50] and hyaluronic acid (HA)[25,26,28,45,51] have been used, often in conjunction, to encapsulate mammalian cells. Here, we report a material system for encapsulation based entirely on HA for the first time. HA, a major extracellular matrix (ECM) glycosaminoglycan, plays important roles in development and wound healing[52]. HA is an attractive platform for engineering cellular microenvironments as it can be readily modified with diverse functionalities; actively promotes cell survival; and is biodegradable through the enzyme hyaluronidase[52,53]. In this paper, we modified HA with lipid groups and click chemistry groups to enable HA deposition onto the cell membrane and to allow for subsequent click reactions. Using these modified HAs, we conformally encapsulated neural stem cells (NSCs) as well as mesenchymal stromal cells (MSCs) to demonstrate the encapsulation capability of modified HAs. By utilizing the chemical groups present on the encapsulation material, we were also able to demonstrate the potential for conformal encapsulations to direct assembly between encapsulated cells in suspension, as well as assembly of cells onto patterned surfaces using photochemistry.

Materials and Methods

lipid-HA-thiol Synthesis

Lipidand thiol-modified hyaluronic acid (lipHASH) was synthesized in three steps. First, lipid-modified HA (lipHA) was synthesized. Second, 3,3’-dithiopropionic acid (DTA) was conjugated to lipHA. Third, the disulfide in the DTA moiety was cleaved to yield lipHASH.

In the first step, hyaluronic acid (HA) sodium salt (Lifecore, 82kDa) was dissolved at 20 mg/mL in deionized (DI) water to achieve a concentration of 2% w/v. Exchange of Na^+ for H^+ was achieved by adding 3 g of Dowex 50W x 8 ion exchange resin (Sigma Aldrich) to the solution for each 1 g of HA and stirring for 3 hr. Resin was removed by filtration, and the remaining solution titrated to pH 7 with tert-butylammonium (TBA) hydroxide (Fisher Scientific, 0.4M in water) to produce HA-TBA[54]. HA-TBA solution frozen and lyophilized to yield dry polymer. Next, to synthesize lipHA, HA-TBA was dissolved in anhydrous dimethylsulfoxide (DMSO, Sigma Aldrich, anhydrous, >99.9%) at 20 mg/mL under nitrogen. For each molar of disaccharide unit of HA, 0.01 mol of 1,2-Dipalmitoyl-sn-glycero-3-phosphoethanolamine (DPPE, Sigma Aldrich, >97%) was dissolved in reagent grade ethanol (Sigma Aldrich, <0.003% water) at 75 °C at 2 mg/mL, then added to HA-TBA solution. Finally, a 10:1 molar ratio of (Benzotriazol-1-yloxy)tris(dimethylamino)phosphonium hexafluorophosphate (BOP, Sigma Aldrich, 97%) to DPPE was dissolved in DMSO and added to the reaction mixture. The mixture was stirred at 40 °C overnight. After the reaction, the mixture was placed in a 5000 MWCO membrane (Cole Palmer) and dialyzed against deionized (DI) water for 1 day, then filtered to remove precipitated excess reagent. The solution was purified by ultrafiltration (Millipore Sigma, Amicon Stirred Cells). The resulting lipHA solution was converted to lipHA-TBA using the same ion exchange method described above and lyophilized. To synthesize the lipHA-dithiopropionic acid intermediate product, lipHA-TBA, 3,3'-dithiopropionic acid (Sigma Aldrich, 99%), and 4-(Dimethylamino) pyridine (DMAP, Sigma Aldrich, >99%) were dissolved at 20 mg/mL in anhydrous DMSO under nitrogen at 45 °C. Di-tert-butyl decarbonate (Boc2O, Sigma Aldrich, >99%) was then added to the dissolved reaction mixture. The reaction proceeded for 20 hr at 45 °C. The molar ratios of lipHA-TBA:DTA:DMAP:Boc2O were 1:3.75:1.875:0.75 for synthesizing lipHASH used in conformal encapsulation and cell assembly and 1:5:2.5:1 for synthesizing material used in photo-patterning. The reaction solution was then dialyzed and ultrafiltered as described above to yield DTA-modified lipHA. To produce lipHASH, 1,4-dithiothreitol (DTT, Sigma Aldrich, 97%) was added to the DTA-modified lipHA solution at 1:1 w/w DTT to HA. After the DTT was dissolved, the pH was adjusted to pH 8.5 using 1 M NaOH and maintained for 2 hr. The pH was then adjusted to pH 3.5 to quench the reaction and prevent further disulfides from forming. The final mixture was ultrafiltered with starting pH 3.5 and finally flash frozen for later use.

MaHA, HASH, norHA Syntheses

Maleimide-modified HA (MaHA) was made as previously described 55. Briefly, HA-TBA was synthesized as described above. HA-TBA and N-(2-Aminoethyl)maleimide trifluoroacetate salt (Sigma Aldrich, >95%) were dissolved in DMSO. HA-TBA was dissolved at 20 mg/mL of DMSO, and the molar ratio of HA disaccharide units to MA was 1:0.3. BOP was dissolved in DMSO and added dropwise into the reaction mixture. The reaction was allowed to proceed for 3 hr at room temperature, then dialyzed and ultrafiltered as described above. Thiol-modified HA (HASH) was made as previously described 56. HA-TBA, 3,3’-dithiopropionic acid, and DMAP were dissolved in DMSO at 45 °C. Then, Boc2O was added and the reaction was allowed to proceed for 20 hr at

45 °C. The molar ratio of HA-TBA:DTA:DMAP:Boc2O was 1:5:2.5:1. The conjugated DTA was subsequently reduced using DTT as described above. Norbornene-modified HA (norHA) was made as previously described 57. Briefly, 5-norbornene-2-carboxylic acid (Sigma Aldrich, mixture of endo and exo, predominantly endo, 98%) was coupled anhydrously to HA-TBA in DMSO via Boc2O conjugation to yield norHA, purification was done through dialysis in DI water.

Peptide Synthesis

All peptides used in this study were synthesized using a Liberty Blue (CEM) automated, microwave-assisted solid phase peptide synthesizer using Fmoc chemistry. Briefly, Rink amide resin (Advanced Chemtech, 100–200 mesh, 1% DVB) was swollen with dimethylformamide (DMF, Aldrich, ACS reagent grade), and the immobilized Fmoc group removed with 20% (v/v) piperidine in dimethylformamide. Fmoc-protected amino acids (Advanced ChemTech, 0.2 M in DMF, 5 equivalents relative to theoretical available sites on the resin) and the coupling agents diisopropylcarbodiimide (DIC, Aldrich, 99%, 1 M in DMF) and Oxyma Pure (Advanced ChemTech, 1 M in DMF) were added to the reaction vessel and heated to 90 °C for 4 min. The Fmoc deprotection and coupling steps were repeated to build the peptide from the C-terminus to the N-terminus. For fluorescent peptides, 5(6)carboxyfluorescein (Sigma Aldrich, >95%) was added last onto the N-terminus. The resultant peptides were cleaved from the resin with a cocktail of 92.5% trifluoroacetic acid (TFA, Aldrich, 99%), 2.5% triisopropylsilane (TIPS, Aldrich, 99%), 2.5% 2,2(ethylenedioxy) diethanethiol (DODT, Aldrich, 95%), and 2.5% DI water, and then isolated by precipitation into cold diethyl ether (Aldrich, ACS reagent, contains butylated hydroxytoluene as inhibitor) and centrifugation. After removal of ether under vacuum, the peptides were resuspended in DI water, frozen in liquid nitrogen, lyophilized, and stored at 20 °C as powders until ready for use. High performance liquid chromatography (HPLC) was used to determine peptide purity.

lipHA-fluor synthesis

lipHA, synthesized as described above, was functionalized with hydrazides to which fluorescein isothiocyanate (FITC) was directly conjugated. First, lipHA-hydrazide (lipHA-ADH) was synthesized by combining lipHA, N-hydroxysuccinimide (NHS, Thermo Fisher, 99%), and adipic acid dihydrazide (ADH, Sigma Aldrich, >98%) in DI water at a molar ratio of lipHA (disaccharide units):NHS:ADH 1:2:5. LipHA was dissolved at 10 mg/mL. 1-Ethyl-3-(3-dimethylaminopropyl)carbodiimide (EDC, Sigma, Aldrich, >98%) was then dissolved in DI water and added to the solution mixture at equimolar ratio to NHS. The pH of the reaction mixture was then titrated to 6 using 1M HCl and 1M NaOH. The reaction was allowed to proceed overnight. To purify lipHA-ADH, the resulting solution was dialyzed for 3 days in DI water and lyophilized. To convert hydrazide groups to fluorescent moieties, lipHA-ADH was dissolved at 0.5 wt% in 0.1 M dibasic disodium phosphate buffer (Sigma Aldrich, ACS reagent grade) and an equimolar quantity of fluorescein isothiocyanate (FITC, Sigma Aldrich, isomer I, >90%) to single disaccharide units of HA was dissolved at 0.5 wt% in DMSO and added to lipHA-ADH solution. The reaction was allowed to proceed overnight. The mixture was then dialyzed for 3 days and lyophilized.

NSC and MSC culture

Rat hippocampal NSCs (Millipore Sigma) were cultured on tissue culture flasks coated with poly-L-ornithine (Sigma Aldrich, poly-L-ornithine hydrobromide, MW 30,000 – 70,000), then laminin (Sigma Aldrich, 1-2 mg/mL in Tris-buffered saline) to support NSC attachment. The NSC culture medium was DMEM with reduced glutamine (Thermo Fisher), B27 supplement (Thermo Fisher, B27 50X), and 1x antibiotic-antimycotic (anti-anti, Thermo Fisher, Antibiotic-Antimycotic (100X)). Medium was changed every two days and bFGF (PeproTech, Recombinant Human FGF-basic) was maintained at a concentration of 20ng/mL for each media change. MSCs (Lonza) were cultured in MEM alpha (Sigma Aldrich) medium supplemented with 10% fetal bovine serum (Thermo Fisher) and 1x anti-anti. Culture medium was changed every 2 days during the course of culture. All cell lines were cultured in a humidified incubator with 5% CO2 at 37°C. To harvest NSCs, flasks were treated with 3 mL of Accutase™ (Biolegend) after media aspiration and were incubated for 3 min to allow enzymatic detachment. For MSCs, 4 mL of 0.05% Trypsin (Fisher Scientific) was added to each flask after media aspiration and washing with PBS, and a 5 min incubation was used. The harvested cells were subsequently centrifuged to form pellets and resuspended in medium for continued passaging or in desired solutions for experimental use.

Conformal Encapsulation of NSCs, MSCs, and NSC spheroidsNSCs and MSCs were encapsulated by first incubating the cells in 0.5 mg/mL lipHASH solution for 30 min at

4 °C. 1 mL of lipHASH solution was used for each 1-2 million NSCs or MSCs. The cells were then centrifuged at 300 g for 5 min and washed with 10 mL of Dulbecco's phosphate buffered saline (DPBS, Fisher Scientific, no calcium, no magnesium) once. For the second layer of encapsulation, the washed cells were resuspended in a 5 mg/mL MaHA solution and incubated for 15 min at 4 °C. After incubation, the cells were centrifuged at 450 g for 3 min, then washed once with 10 mL of DPBS. For a third layer of encapsulating material, cells were incubated in 5 mg/mL HASH solution for 15 mins at 4 °C, then centrifuged at 450 g for 3 min and washed with 10 mL DPBS once. For encapsulations of four layers and more, the steps described above were repeated with alternating incubations in MaHA or HASH solutions. All solutions were made by dissolving modified HA in DPBS, then filtering the solution through a 0.45 µm syringe filter followed by a 0.22 µm sterile filter for sterilization. To enable fluorescent imaging of multilayered coatings, MaHA was covalently modified by a cysteine-containing peptide that was end-conjugated with rhodamine B (GCGKKK-RhoB). The peptide was dissolved in DPBS at 10 mg/mL then added to a 5 mg/mL MaHA solution prior to sterilization. Peptide was added to give a 3% degree of substitution relative to total HA disaccharide units. For encapsulation of NSC spheroids, the spheroids were collected by centrifuging at 200 g for 5 minutes. All centrifuge spins after washes were adjusted to 200 g and 5 minutes. Spheroids were resuspended by gentle trituration via pipetting of the spheroid pellet. The rest of the encapsulation procedures were the same as in single NSC encapsulations.

Live/Dead Assay and Encapsulation Fraction Analysis

After encapsulation, NSCs or MSCs were cultured in 24 well plates for 3 days. Fluorescence around cells – resulting from labeling MaHA as described above – as well as cell shape were used as metrics to assess if the cells stayed in encapsulation. Microscopy images were taken and encapsulated cells, as well as cells that appeared unencapsulated in culture, were counted over 3 days to track the fraction of cells that stayed in encapsulation. For live/dead staining, calcein AM/ethidium homodimer (LIVE/DEAD™ Viability/Cytotoxicity Kit, for mammalian cells) were used. Each day, multiple wide field microscopy (Leica DMi8 Widefield) images were taken for each well after live/dead staining, live and dead cells were counted for all the images, and the cells from that day were disposed.

Assembly of NSCs via Complementary Chemistries

NSCs were split into two groups and encapsulated in either lipHASH (single-layer encapsulation) or lipHASH and MaHA (2-layer encapsulation). After washing with DPBS, the cells were allowed to assemble through centrifugation. The cells were mixed at a ratio of 1:5 MaHA to lipHASH. Cell suspensions were centrifuged at 300 g for 5 min, and the pellet was resuspended by gentle pipetting without replacing the medium in which they were suspended.

Photopatterning of NSCs onto a norHA Hydrogel Surface

NSCs were encapsulated in a layer of lipHASH as described above. After washing with DPBS, the encapsulated cells were suspended at a density of 5 million cells/mL in a solution consisting of a photoinitiator lithium phenyl-2,4,6-trimethylbenzoylphosphinate

(LAP, Sigma Aldrich, >95%) at 1mM in DPBS. 100 µL of the cell solution was then pipetted onto the norHA gel and a photomask was positioned on top of the solution. Fabrication of norHA hydrogel was conducted as previously described 58. Briefly, glass coverslips were functionalized with 3-(mercaptopropyl) trimethoxysilane (MTS, Sigma Aldrich, 95%) The coverslips were then washed sequentially in dichloromethane (DCM,Sigma Aldrich, >99.8%), 70% ethanol in water, and DI water. norHA hydrogels were created on coverslips from a solution consisting of 5% (w/v) norHA, 1 mM LAP and DTT. The solution was crosslinked by irradiation for 2 min at 365 nm (10 mW/cm2, Omnicure). The NSCs were allowed to settle to the hydrogel's surface over 10 min, then the NSCs on the gels were exposed under 20mW/cm^2 UV light through the photomask for 1 min. This induced crosslinking between pendant norbornene moieties on the hydrogel surface and thiols on the lipHASH coating. The photomask was then removed and the hydrogel washed with DPBS 3 times to remove non-attached cells.

Bulk Degradation of MaHA – HASH Gel

Bulk gels were made by mixing HASH and MaHA solutions together to achieve a final concentration of 5 mg/mL for both materials. HASH and MaHA solutions were made separately at 10 mg/mL. 100 µL of MaHA solution was added to the bottom of 96 well plates. Then, 100µL of HASH solution was added to the MaHA solution and mixed with a pipette. Gelation occurred within 10 seconds. The gels were then transferred to transwell inserts and cultured for 7 days in a 24-well plate with enough PBS to cover the gel. The mass of gels was measured every day and compared to their original mass.

Results

Material Synthesis and Conformal Encapsulation of Neural Stem Cells

LipHASH and MaHA were synthesized as illustrated in Scheme 1. HASH was synthesized from HA via the same Boc2O reaction used to synthesize lipHASH from lipHA. All HA derivatives were characterized using 1H NMR (Supplemental Fig S1-S3.). The lipid chosen for our modification has previously been shown to be able to insert into cell membranes[43]; we modified HA with an average of 1 lipid per HA chain in aiming to maximize the conformational freedom of lipHA attached to the cell membrane. Our syntheses yielded a ~ 0.3 degree of substitution for both HASH and MaHA.

Our approach to creating a multilayered conformal encapsulation is illustrated in Scheme 2, where the pendant lipids that were conjugated to the HA backbone in lipHASH inserted into the plasma membrane to create a lipHASH first layer with free thiols available for reaction. Then, via maleimide-thiol click chemistry, MaHA could be conjugated to the first layer to create a two-layer encapsulation formed by the crosslinking of a thin HA-based hydrogel around the cell. Unreacted maleimide moieties in the second layer then served to crosslink to a subsequent layer of HASH, with continuing build-up of the hydrogel encapsulation possible through further conjugation of alternating layers of MaHA and HASH.

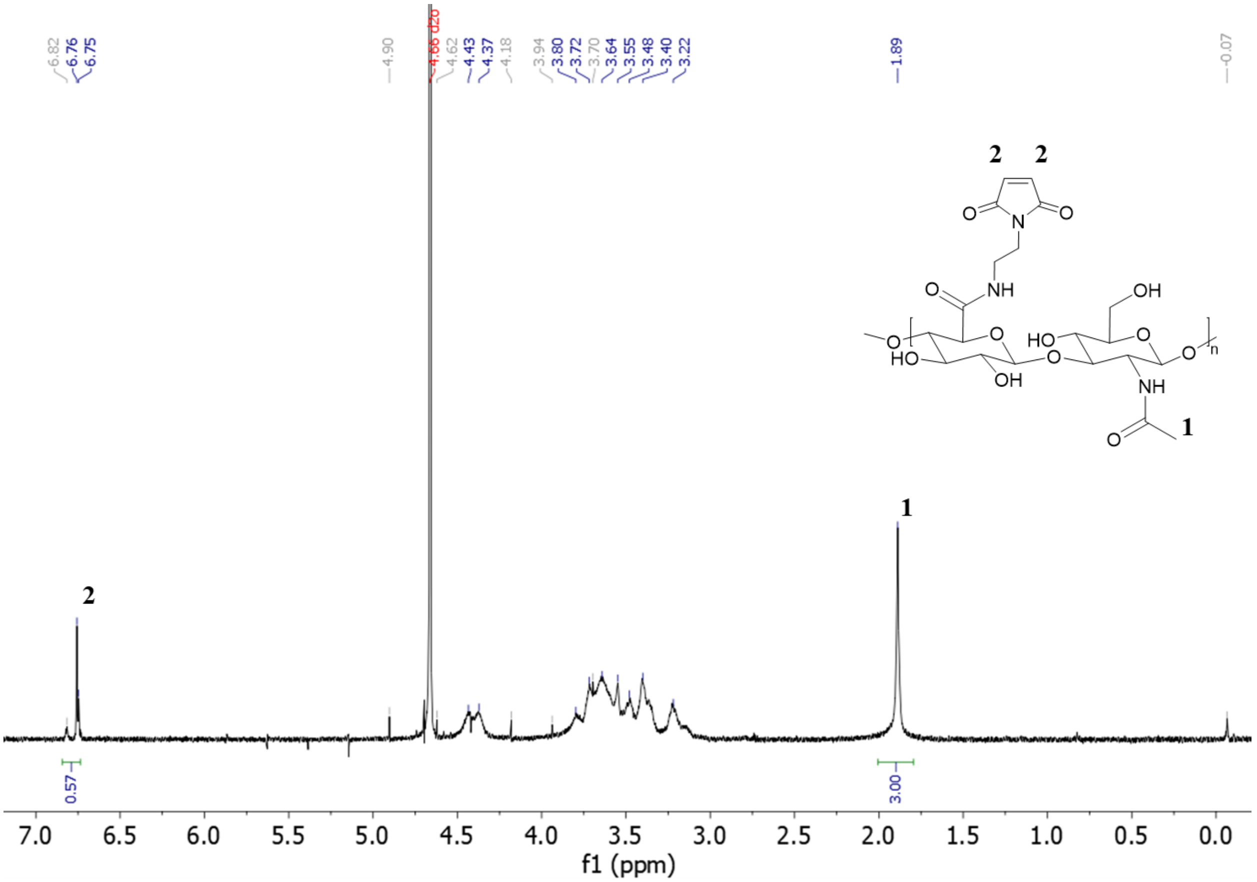

Figure S1. ^{1}H NMR spectrum of MaHA

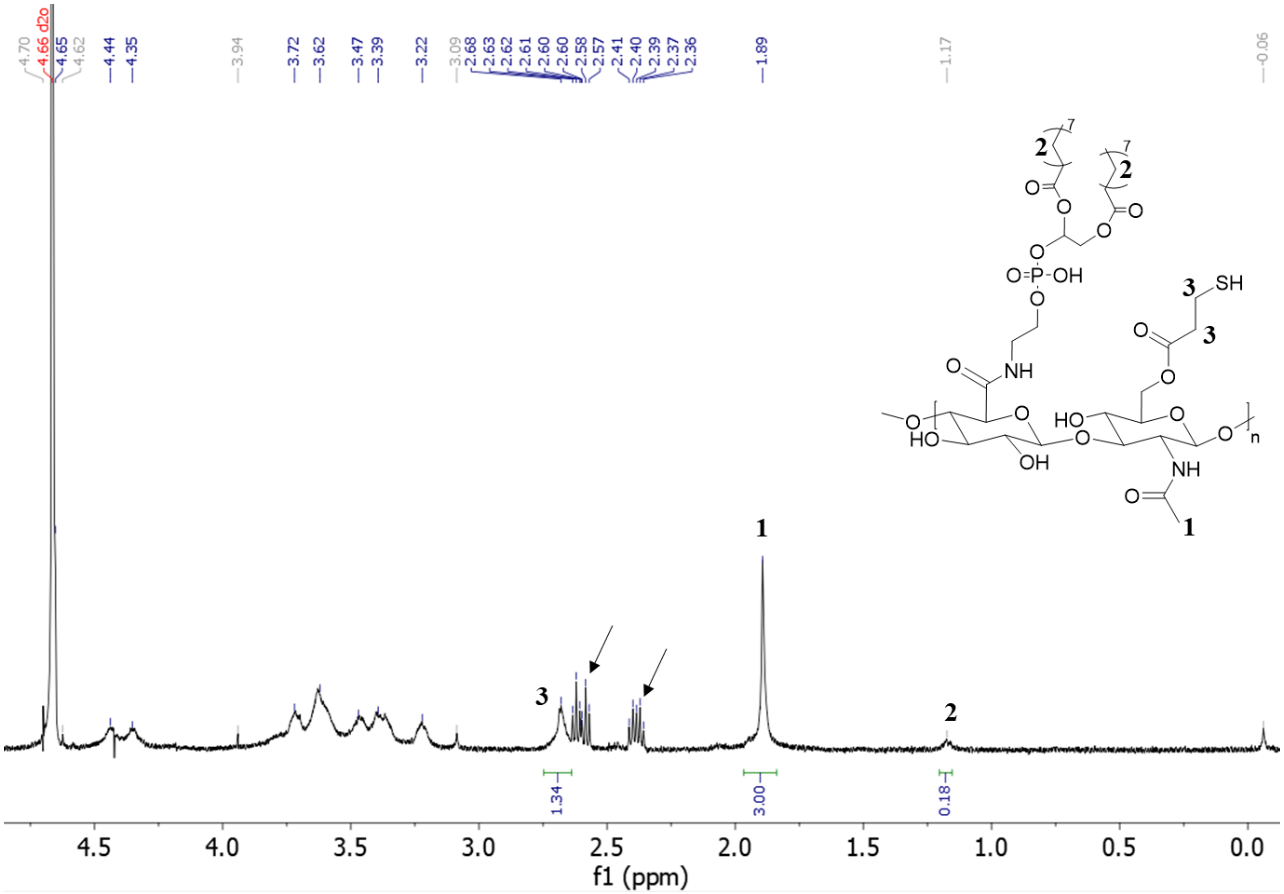

Figure S2. ^{1}H NMR spectrum of lipHASH

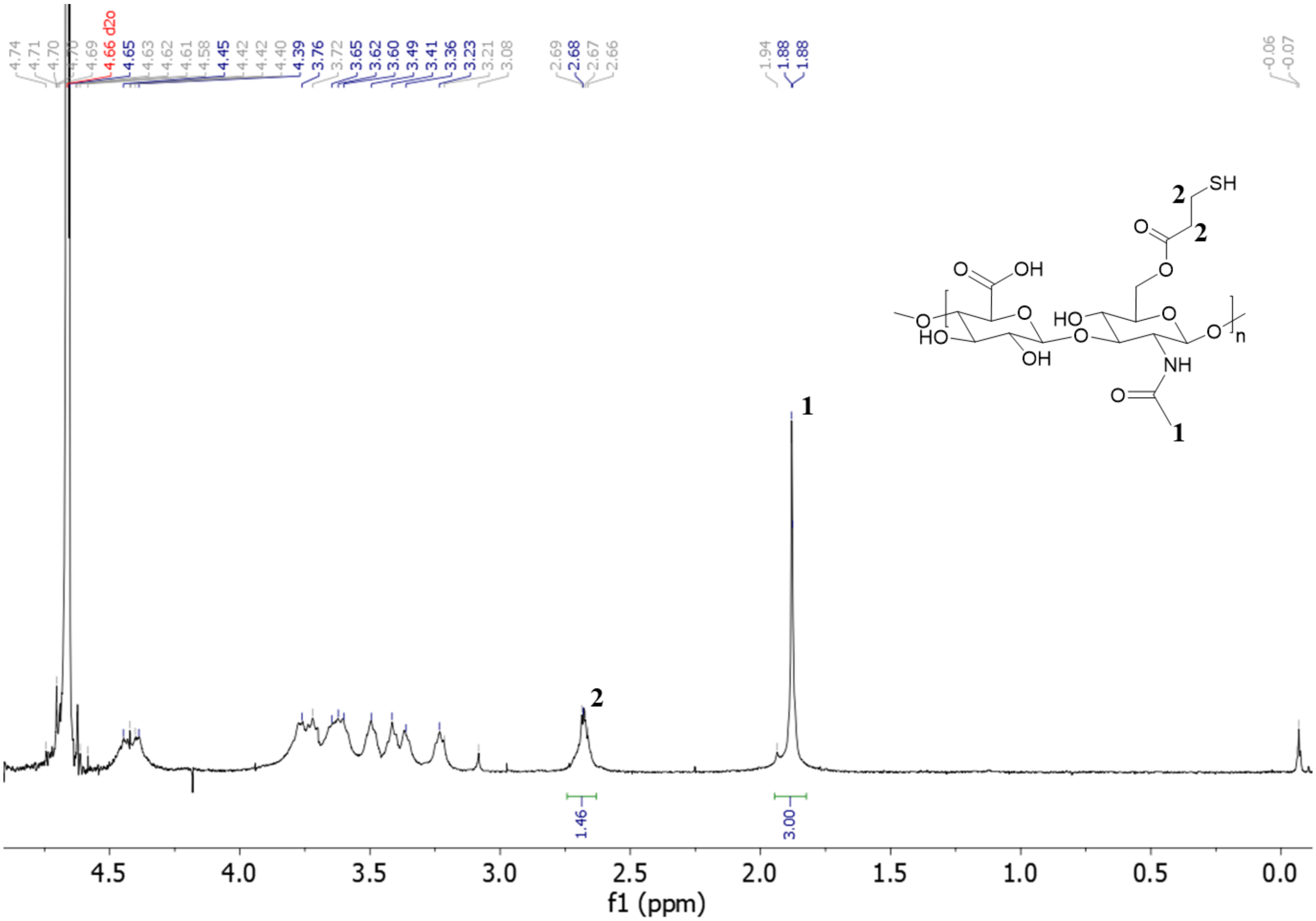

Figure S3. ^{1}H NMR spectrum of HASH

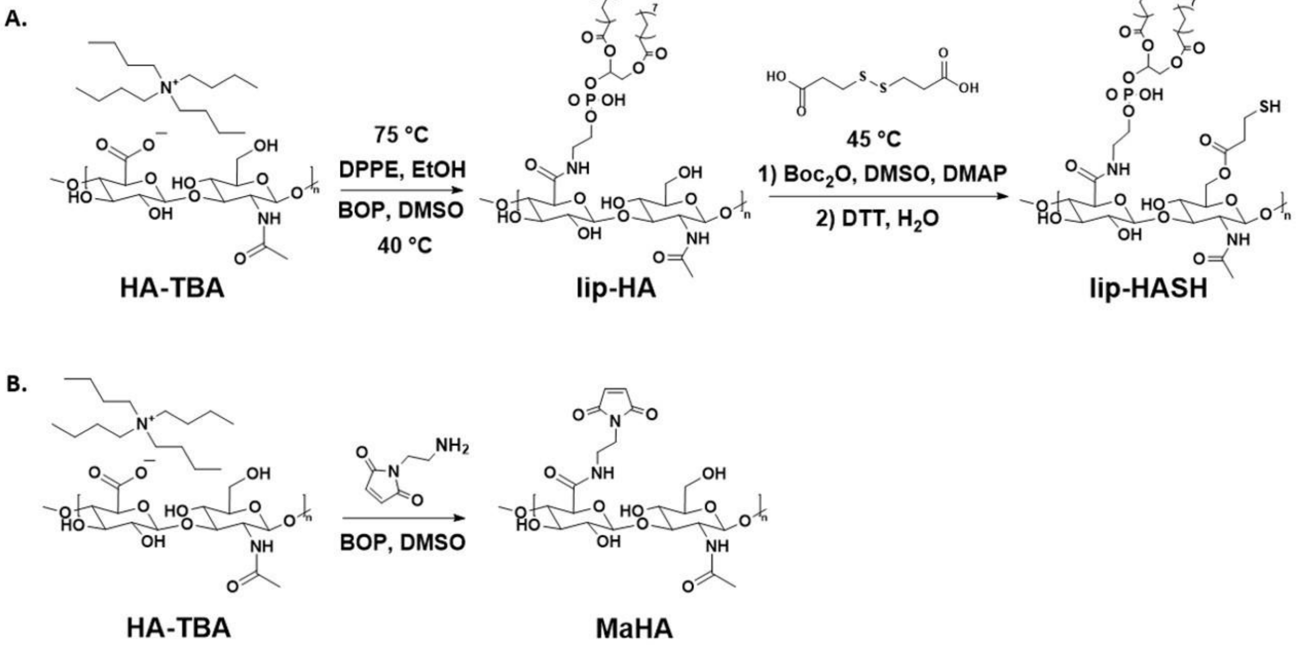

Scheme 1 A) Synthesis of lipHASH. HA-TBA is the tert-butyl ammonium salt of HA, generated through ion exchange as described above. lipHA is synthesized first, then lipHA-dithiol is made in the same way as HA-dithiol; and the dithiol (shown above the second step arrow) is subsequently cleaved using DTT to generate pendant thiol group. **B)** Synthesis of MaHA.

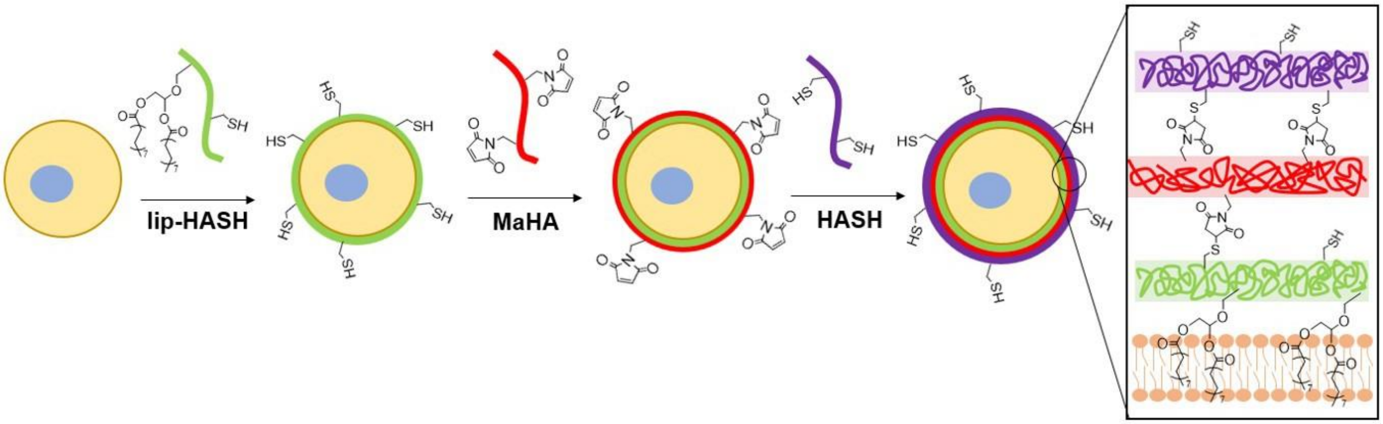

Scheme 2. The process of conformal cell encapsulation. lipHASH is deposited onto the cell membrane by hydrophobic interaction, then maleimide-thiol click chemsitry is utilized for subsequent conjugations to deposit more layers of HA (final covalent bonds formed and the interaction of the conjugated lipids with the cell membrane are shown on the right)

To confirm the association of lipHA with the cell membrane, we synthesized FITC-conjugated lipHA (lipHA-FITC) to enable visualization of lipHA by fluorescent microscopy. NSCs incubated with lipHA-FITC exhibited a clear fluorescent ring around cells, indicating of lipHA-FITC localization at the cell surfaces (Fig. 1A). To confirm the addition of the second encapsulation layer using MaHA, we tagged MaHA with rhodamine B (RhoB-MaHA). Encapsulation of NSCs using non-fluorescent lipHASH and then RhoB-MaHA also showed clear fluorescence on NSCs (Figure 1B). We next conducted experiments to rule out potential contributions of auto-fluorescence and non-specific interactions (Figure 1C), such as adsorption of HA to the cell surface or the reaction of maleimides (in MaHA) to matters present on the cell surface. NSCs were first incubated in PBS (control), lipHA-FITC (non-thiol containing, fluorescent group), or an 80:20 mixture of lipHASH and lipHA-FITC (lipHASH for reactivity and lipHA-FITC for fluorescence). We expected the control group to show little or no fluorescence; and both lipHA-FITC containing groups to show strong fluorescence in the FITC channel due to lipid insertion of modified HAs into the plasma membrane. We also expected that NSCs incubated with only lipHA-FITC would show a stronger fluorescence due to the higher number of FITC-containing molecules. After the first incubation, NSCs were washed and incubated again in PBS (control) or RhoB-MaHA (all other groups). We expected that NSCs incubated in PBS to show little or no RhoB signal. For NSCs incubated in lipHA-FITC, if non-specific interactions were few, little or no RhoB signal should likewise be expected. However, for NSCs incubated in lipHASH and lipHA-FITC, stronger RhoB signal should be expected due to reactivity between RhoB-MaHA and lipHASH. We quantified fluorescence intensity of FITC and

RhoB using ImageJ and saw that both lipHA-FITC-containing groups showed significant

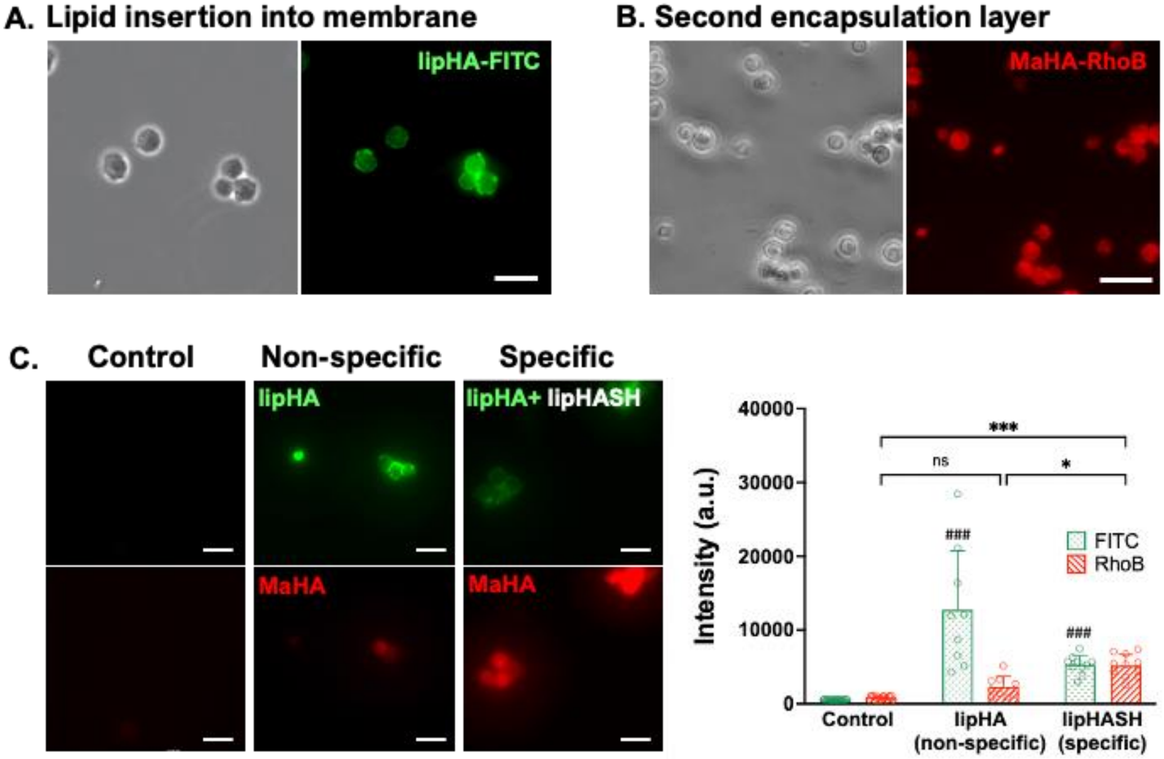

Fig. 1 A) NSCs encapsulated in a layer of FITC-tagged lipHA. **B)** Fluorescence from MaHA around NSCs after 1 day of culture post encapsulation. **C)** Left panels: Representative images of FITC (top row) and RhoB (bottom rjow) channels for NSCs incubated in PBS (left), lipHA-FITC then RhoB-MaHA (middle), and mixture of lipHA-FITC + lipHASH then RhoB-MaHA (right). Right: quantification of standardized fluorescence among three groups. # denotes significant differences of FITC when compared to control group. n = 88 cells were used for statistical testing using Welch's ANOVA and Dunnett's T3 test. Scale bars = 50 μm. For all figures: *$p < 0.05$, **$p < 0.01$, ***$p < 0.001$.

increases in fluorescence intensity compared to the PBS control. We also saw no significant increase in RhoB signal when RhoB-MaHA incubation followed lipHA-FITC incubation, suggesting minimal non-specific interactions. On the other hand, significantly higher RhoB signal was observed in NSCs incubated with lipHASH before RhoB-MaHA incubation.

Varying Conformal Encapsulation Layers Using NSCs and NSC spheroids

We next considered the conformal hydrogel's stability over time and effects on viability in NSC encapsulations. Since a minimum of 2 layers of material are needed to form a crosslinked network, NSCs were encapsulated with 2, 3, or 4 layers of modified HA and cultured over multiple days. To visualize the encapsulating hydrogel, we used RhoB-labeled MaHA and HASH tagged with Atto 488-maleimide. As expected, fluorescence in both channels were detected around the encapsulated NSCs after 2 layers of encapsulation (Fig. 2A). Next, NSCs were encapsulated with 3 layers and 4 layers of alternating MaHA and HASH. Live/dead stain using calcein AM and ethidium homodimer showed that over 94% cells remained viable immediately after encapsulation (Fig. 2B).

After encapsulations, were cultured on surfaces treated for adherent NSC culture. We quantified cell egress from encapsulation based on the fraction of NSCs that lost the fluorescent HA at their plasma membranes, and we visually confirmed adherence to the planar surface by the extension of small processes and loss of spherical morphology seen in suspension culture while encapsulated. We saw that for 2 layers of encapsulation, egress occurred within 24 hours. The time needed for egress increased for 3 layers of encapsulation, with the fraction of cells encapsulated remaining higher compared to 2 layers over subsequent days in culture (Fig. 2C). No significant cell egress occurred during multi-day culture when cells were surrounded by a 4-layer conformal hydrogel. To further assess the stability of the encapsulation, bulk hydrogels of MaHA and HASH were made at the same concentration used for cell encapsulation, and the degradation of the bulk gel was tracked over a period of 7 days (Supplemental Fig S4). The degradation of the bulk

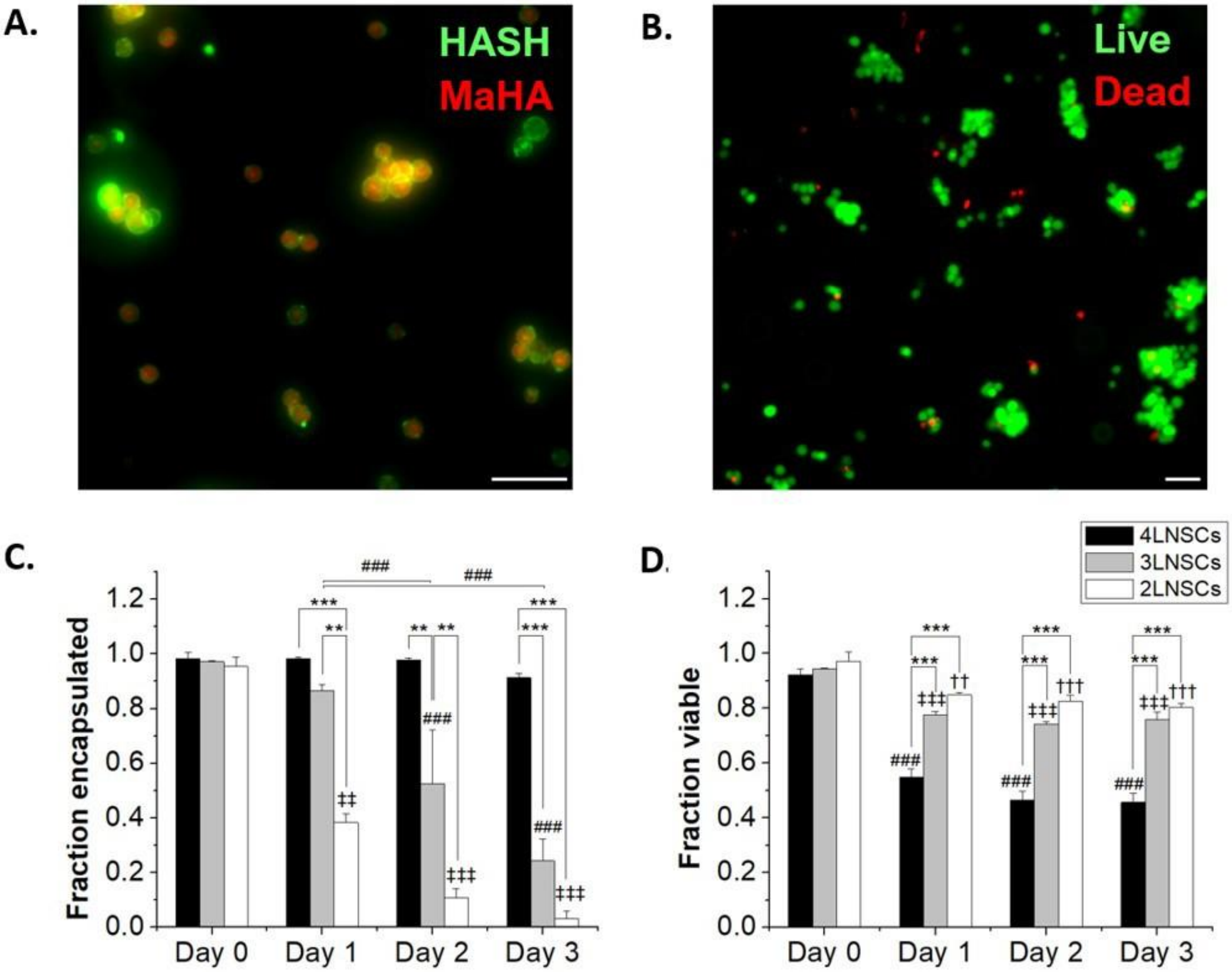

Fig. 2 A) NSCs encapsulated in RhoB-tagged MaHA and then Atto 488-tagged HASH. **B)** Representative image of live/dead staining immediately after encapsulation. **C)** The fraction of NSCs that remained encapsulated over 3-day culture periods. **D)** The fraction of NSCs that remained viable over 3-day encapsulation periods. For both C and D, * denotes significant differences within groups. For C, and ‡ denotes significant differences of 3-layer and 4 layer-encapsulated NSCs compared to Day 0, respectively. For D, #, ‡, and † denotes significant differences of 2-layer, 3-layerand 4-layer-encapsulated NSCs compared to Day 0, respectively. Two-way ANOVA and Tukey's Post hoc tests were run for statistical testing. There are at least 3 replicates for each group, and for each replicate, n > 468 cells were counted. A total of 12,282 cells and 7,587 cells were used to assess encapsulation fraction and viability fraction, respectively. All scale bars = 50 μm.

gel occurred slowly, with 80% of the gel remaining at day 3, suggesting that while degradation occurs, cell egress is likely also facilitated by other active mechanisms such as cytoskeletal movement and enzymatic degradation.

We tracked NSC viability over 3 days in culture: in the group with a 2 layered HA hydrogel, NSCs retained >80% viability over 3 days as they were able to exit the encapsulation and proliferate. In groups with 3 layers and 4 layers of encapsulations, we observed viability decreases concomitant with reduced egress. NSCs exhibited 75.8 ± 2.8% and 45.7 ± 3.4% viability after 3 days in culture when encapsulated in 3 layers and 4 layers of HA, respectively.

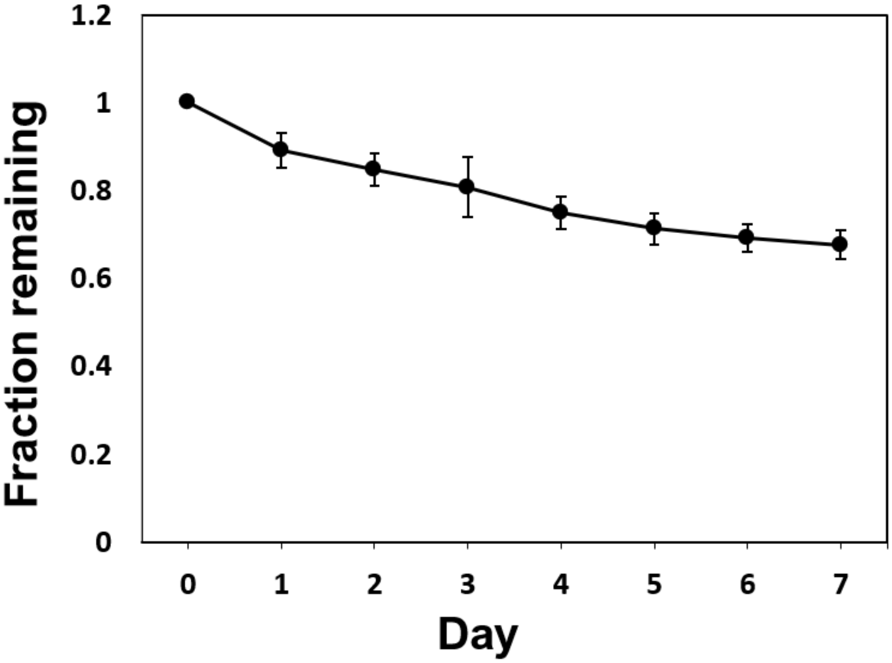

Figure S4. MaHA-HASH gel degradation. Gel degradation was assessed by tracking the weight of the MaHA-HASH gels for 7 days. The weight of the gels was normalized to their original weight at day 0. n=3 replicates were done for the degradation, for each replicate, >5 gels were made as repeats.

One potential factor for the loss of cell viability could be the reduced cell-to-cell contacts mediated by increasing layers of encapsulations. To elucidate the impact of cell-cell interactions on cell survival, we cultured NSCs on non-adherent plates to form NSC spheroids. These spheroids were then encapsulated similarly to NSCs, by incubation sequentially in solutions of lipHASH, MaHA, and HASH. NSC spheroids with 2 layer, 3 layer, and 4 layers of encapsulations were created. Similar to NSCs, the NSC spheroids showed strong fluorescence on Day 0 covering all spheroids (Figure S5). After 2 days, in 2-layer encapsulation groups, cells on the perimeter of the spheroids appeared to have no fluorescent signals, suggesting proliferation of and growth of NSC spheroids and egress of NSCs from the encapsulation (Supplemental Fig S5-S6). However, for all encapsulation groups, viability of the spheroids over the 3-day culture period was above 90% (Figure 3), assessed using a live/dead kit. This suggests that established cellular contacts could enhance the survivability of encapsulated NSCs.

Conformal Encapsulation of NSC Spheroids

In encapsulating single NSCs, we observed that NSCs that formed clusters appeared to have higher viability than single NSCs, presumably due to cell-cell contact and signaling. To assess whether clustering of NSCs facilitated survival, we cultured NSCs into spheroids and encapsulated the spheroids using the same materials. Spheroids were encapsulated with 2, 3, or 4 layers of modified HA and cultured over multiple days, rhodamine B was conjugated to MaHA and thus incorporated into the encapsulation for visualization. The encapsulation and viability of spheroids were tracked over 3 days for comparison with single NSCs.

Strong fluorescence was observed on Day 0 around all spheroids. After the initial encapsulation, cells that appear to be on the exterior of the fluorescently labeled conformal encapsulation can be observed (Supplemental Fig S5-S6). Viability of the spheroids were assessed over the 3-day culture period using a live/dead kit (Figure 3A, B). High viability (>90%) was observed across all groups at all time points.

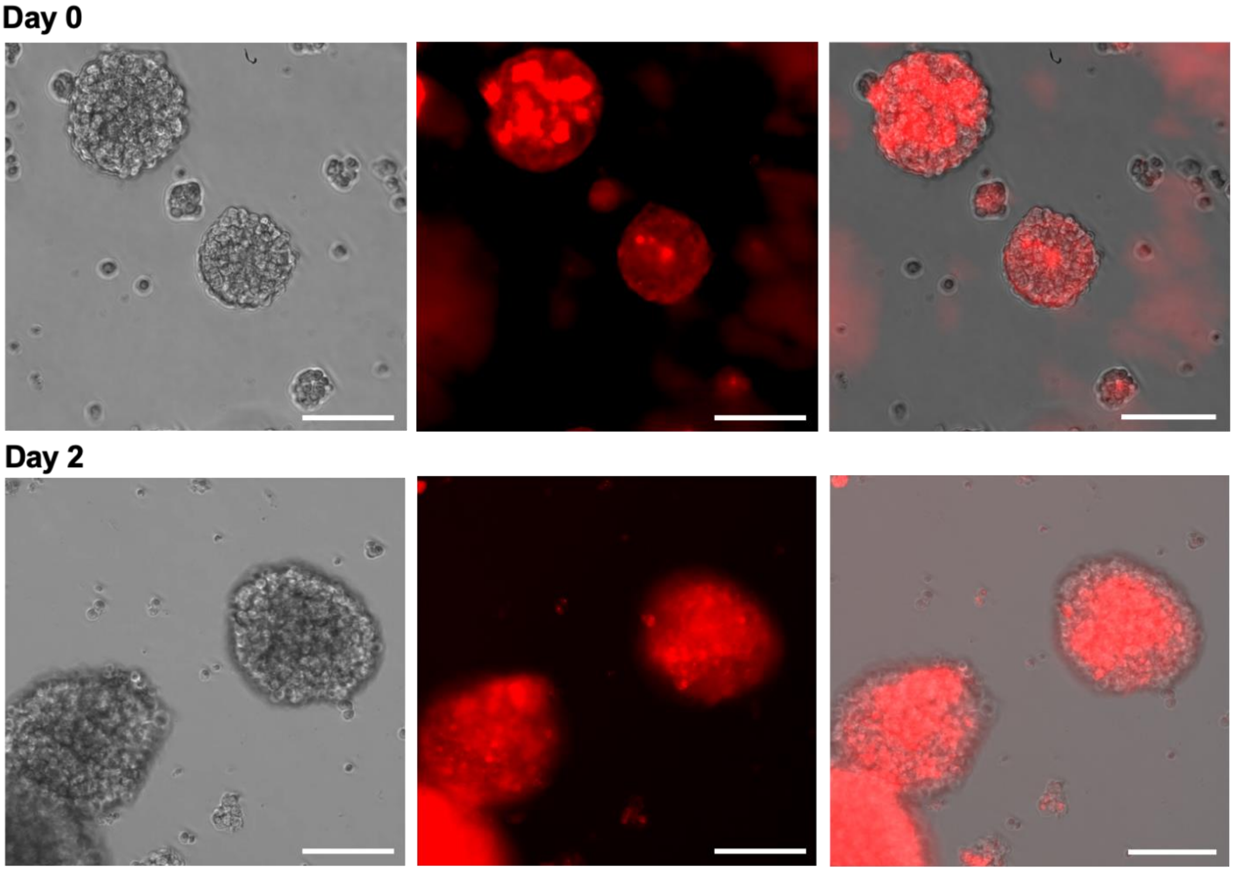

Figure S5. NSC spheroids encapsulated with 2 layers of material on Day 0 (Top row) and Day 2 (Bottom row). From left to right: phase contrast image of NSC spheroids; fluorescent image of spheroids coated in rhoB-conjugated MaHA; and merged image of both phase contrast and fluorescent channel. Scale bar = 100 µm.

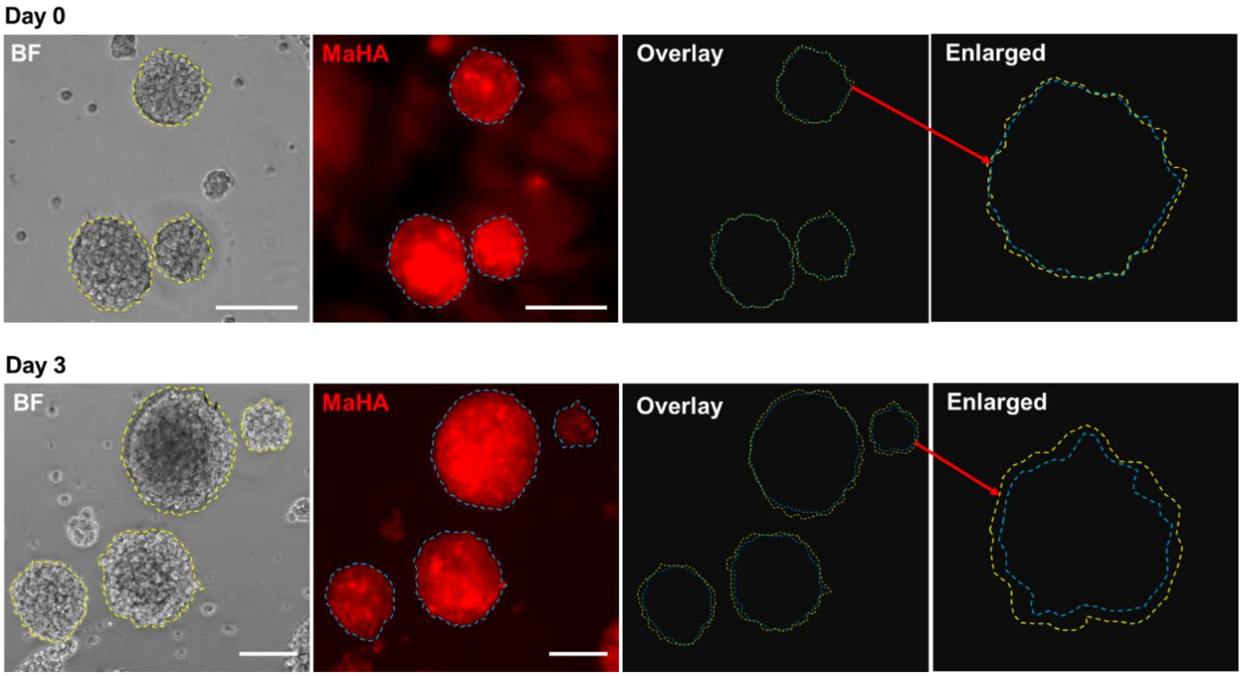

Figure S6. Comparing NSC spheroids encapsulated with 2 layers of material after 3 days. From left to right: spheroids with 2 layers of encapsulation in bright field (outline traced in yellow); spheroids with 2 layers of encapsulation under fluorescence (outline traced in blue); overlay of traced outlines from bright field and fluorescent micrograph; and enlarged overlay of selected outlines (indicated by red arrow). Scale bar = 100 μm.

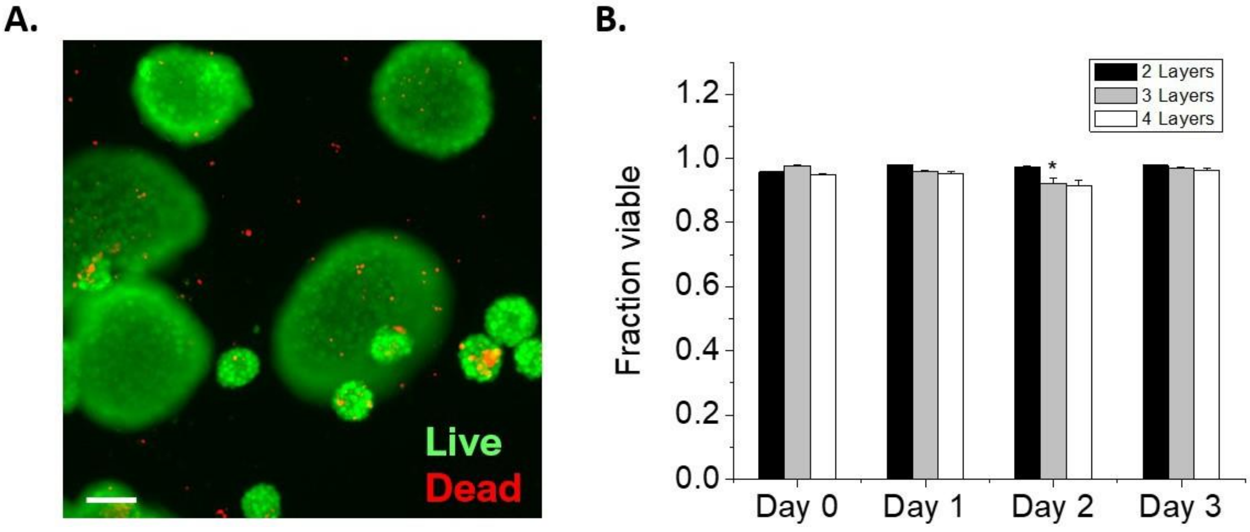

Figure 3. A) Representative image of a live/dead stain for D0 NSC spheroids with 2 layers of encapsulation. **B)** The fraction of NSCs that remained viable over 3 days was >90% in all groups. * denotes significant differences within the same group when compared to D0. There are at least 3 replicates for each group, and for each replicate, n > 3000 cells were counted. A total of 228,605 cells were used to assess viability. Scale bar = 100 μm.

Conformal Encapsulation of Mesenchymal Stromal Cells

NSCs are not contractile and have a reduced cytoskeletal structure compared to contractile cells, and thus are susceptible to damage from processing steps, particularly in single-cell suspension where they lack cell-cell contact that occurs in robust neurosphere cultures or in vivo[59]. MSCs, on the other hand, readily spread on tissue culture plates and do not require significant cell-cell contact to survive[60]. Furthermore, while both NSCs and MSCs have potential in therapeutic transplantation, MSCs are more widely studied as a candidate for cell therapy, due to their immunosuppressant abilities and trophic factor secretion[61,62] and are employed in >1000 clinical trials[63]. Therefore, towards assessing the generality of our encapsulation approach, we encapsulated MSCs in up to 4 layers of HA and assessed the effect of the conformal hydrogel on MSCs, as above for NSCs.

MSCs were encapsulated using the same protocol as for NSCs. Up to 4 layers of encapsulations were established, where lipHASH was used as the first layer, RhoB-tagged MaHA as the second, HASH as the third, and MaHA as the fourth layer. Again, we observed fluorescence around MSCs after forming a 2 layered conformal hydrogel on their surfaces (Fig. 4A). When we looked at the fraction of cells encapsulated over time

(Fig. 4B), we observed a faster rate of MSC egress from 3 layers and 4 layers of conformal encapsulations compared to NSCs. Interestingly, for 2 layer encapsulations, though MSCs started spreading as early as day 1, fluorescent coating remained on the surfaces of adherent cells. This indicates that MSCs were able to spread in the presence of the 2-

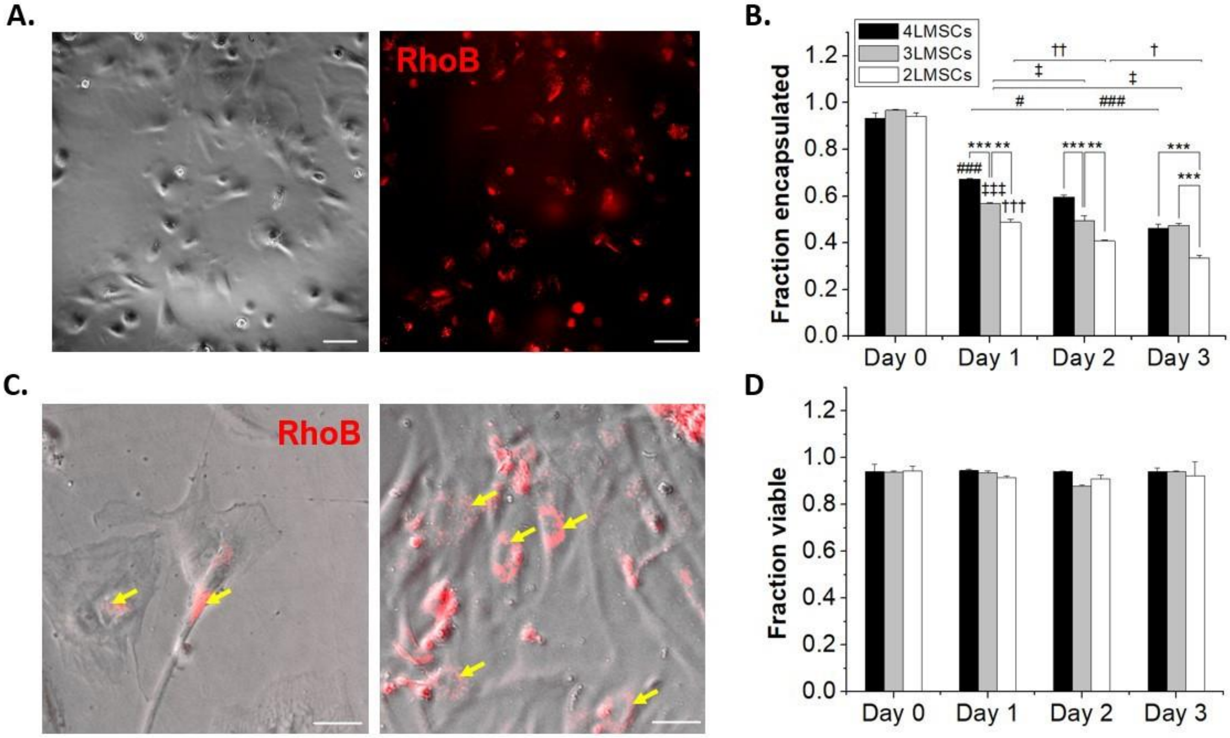

Fig. 4 A) MSCs encapsulated in lipHASH and then RhoB-tagged MaHA. **B)** The fraction of MSCs that remained encapsulated over 3-day culture periods**. C)** MSCs spread with MaHA still coating portions of the cell membrane. Yellow arrow denotes where MaHA localizes on the MSCs. **D)** The fraction of MSCs that remained viable over 3-day encapsulation periods, no statistical significance were detected. * denotes significant differences within groups, #, ‡, and † denotes significant differences of 2-layer, 3-layerand 4-layer-encapsulated MSCs compared to Day 0, respectively. There are at least 3 replicates for each group, and for each replicate, at least 472 cells were counted. A total of 14,103 cells and 12,198 cells were used to assess encapsulation fraction and viability fraction, respectively. Two-way ANOVA and Tukey's Post hoc tests were run for statistical testing. All scale bars = 50 µm.

layer conformal coating, perhaps spreading within the coating, through the coating, or in the presence of a coating which is partial disrupted (Fig. 4C).

To further investigate the dynamic of cell egress, we tracked the movement of MSCs encapsulated with 2 layers of material (Supplementary Movie S1). We saw that encapsulated MSCs (visualized by rhoB-conjugated MaHA) were able to spread as soon as 30 minutes after plating. However, we also saw that for some cells, the encapsulation prevented immediate adhesion to the plate. These cells underwent increased blebbing before adhering to the plate (indicated by yellow arrows in the movie). The encapsulating material, however, did not detach from the cell surface. Rather, the materials were rearranged and conformed to MSC movements. This observation is in line with previous work on MSC encapsulations 28. We also observed that while 4 layers of encapsulation prevented NSCs from egressing, it did not have the same effect on MSCs. The MSCs were able to spread and egress even from a 4-layer conformal encapsulation. Notably, we saw that the MSCs maintained high viability across groups and that viability did not significantly drop over multiple days in culture (Fig. 4D).

Assembly and Photopatterning of Encapsulated NSCs

To demonstrate the potential to leverage conformal encapsulation for multicellular assemblies, we utilize the same hydrogel materials used in the conformal encapsulation to generate multicellular clusters and to pattern cells onto a substrate with a resolution of 100 µm using photolithograpy. To direct the assembly of multicellular clusters, we used the complementary thiol-maleimide chemistry to organize multiple cells around a single cell. In one population of NSCs, we created a conformal coating in which the outer layer was lipHASH (thiol-NSCs), containing unreacted thiols. In a second population of NSCs, we assembled a coating whose outer layer was MaHA (mal-NSCs) that contained free maleimides. By mixing these populations in suspension with thiol-NSCs in excess, then centrifuging to bring them together, we were able to create assemblies of thiol-NSCs surrounding mal-NSCs in which the cells were in close proximity and held together by covalent bonds between conformal coatings in directed assembly (Fig. 5A). To assess the specificity of the interaction, we quantified the fraction of mal-NSCs and thiol-NSCs that formed clusters >2 cells. In the mixture of mal-NSCs with excess thiol-NSCs, almost all mal-NSCs formed clusters with thiol-NSCs. Thiol-NSCs, on the other hand, rarely aggregated to each other (Fig. 5B), confirming that maleimide-thiol reaction directed the assembly of NSCs. The assembled construct was stable and withstood vigorous mixing using a handheld pipette.

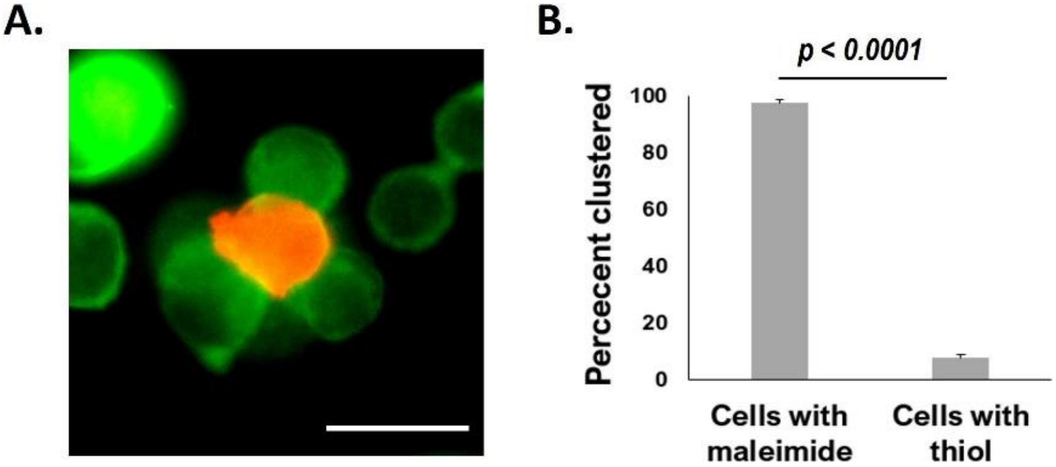

Fig. 5 A) NSCs encapsulated with MaHA (red cells in the center) were assembled together with excess lipHASH-encapsulated NSCs (green cells on the outside). Scale bar = 20 µm. **B)** Significantly more maleimide-presenting cells clustered with thiol-presenting cells (97.5 ± 3.5%) than thiol-presenting cells with other thiol-presenting cells (7.67 ± 2.6%). A total of n = 1,520 cells were used to perform statistical testing with student's t-test.

Photolithography is often used to exert spatiotemporal control over properties of hydrogels that contain photoactive chemical functionalities. Photolithographic modification of a hydrogel offers high-resolution spatial control over crosslinking (e.g. photo-triggered crosslinking), degradation (e.g. using photolabile bonds), and presentation of bioactive molecules[64]. Capabilities that enable cells to be assembled at resolutions that can be attained in light-based photopatterning, which include the length scales of single cells, may be useful in studying basic biology and in fabricating tissue structures[65,66]. Because we can prepare conformal encapsulations that present reactive thiols to the surrounding environment, we investigated the photopatterning of thiolpresenting cells onto norHA hydrogels fabricated with remaining unreacted norbornene pendant groups[67]. To demonstrate the ability to control the positions of conformally encapsulated cells, we encapsulated NSCs in a conformal hydrogel with an outermost layer of HASH or lipHASH. The process for photopatterning encapsulated NSCs is schematically illustrated in Fig. 6A. Briefly, we prepared the norHA substrate as a thin gel conjugated to a thiolated glass slide, with the upper surface of the hydrogel presenting unreacted norbornene groups[58]. We incubated the cells in a dense suspension containing photoinitiator on top of the gel, then used a photomask placed on top of the cells to spatially control light exposure in 100 μm wide stripes. The photoinitiated thio-ene reaction thus crosslinked the conformally encapsulated cells to the norHA substrate in 100 μm wide stripes with equal spacing, demonstrating the specificity and resolution of the interaction (Fig. 6B), the intensity profile across the striped pattern showed that the distance between patterns is ~100 μm in size.

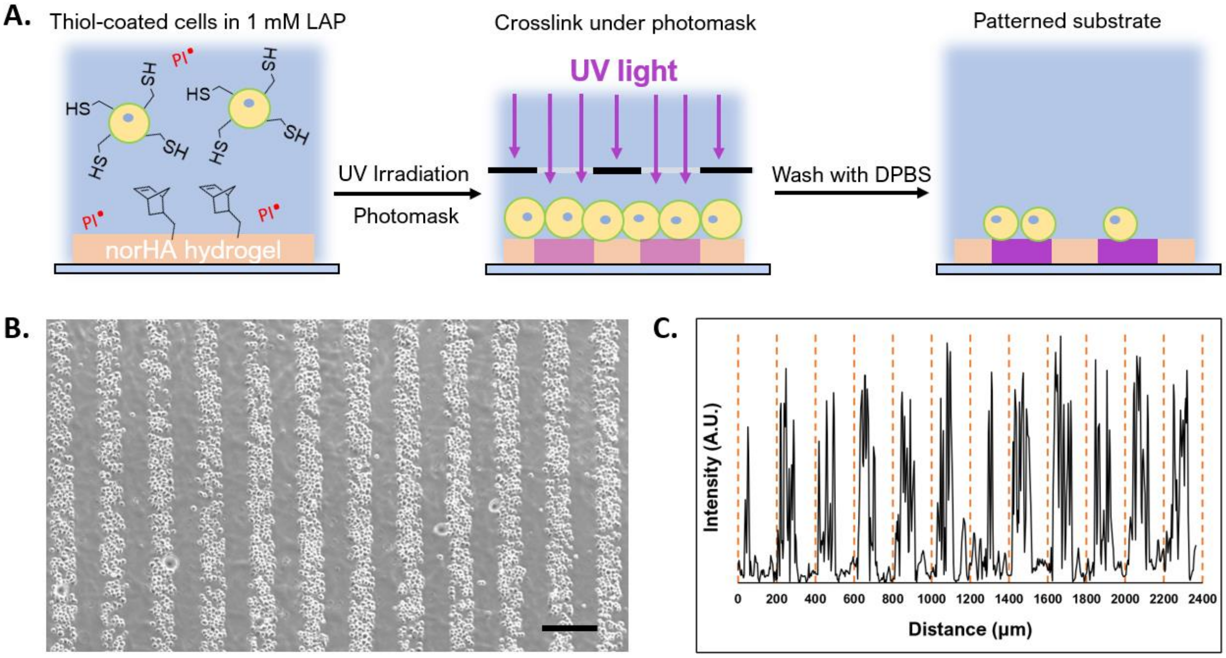

Fig. 6 A) Schematic of the photopatterning procedure, thiolated cells are allowed to settle on the norHA gel (orange in schematic) with a photoinitiator (LAP) present, a photomask (black slit in schematic) was then fitted to the surface of the solution. NSCs are then UV crosslinked to the substrate for 1 min, the striped pattern (purple in schematic) remained after washing with PBS. **B)** NSCs encapsulated in lipHASH then photopatterned onto norHA substrate. Scale bar = 200 μm. **C)** The intensity profile of the photopatterned substrate was quantified using imageJ, the distance between the yellow dashes is 200 μm.

Discussion:

The conformal encapsulation system we studied here was based on HA, which can be used to design hydrogels for many applications[53]. We used a lipid modification to localize an initial layer of the HA material to the cell surface. This approach, based on the interaction between the pendant phospholipid and the cell membrane, has been used with synthetic glycopolymers[68], DNA[43], and PEG[46,69] and appears generalizable for localizing material onto cell membranes. For our lipid material, our synthesis method allows us to control the degree of substitution for both lipid and thiol pendant groups, making it tunable: we observed that the degree of substitution (DoS) for lipid could be increased up to 5% before lipid-HA became almost insoluble, and we were able to achieve a DoS for thiol functionality of up to 40%. Concurrently, the use of a glycosaminoglycan (HA) reduced concerns about cytotoxicity present in some conformal encapsulation systems, as it is sometimes seen in synthetic polyelectrolyte-based encapsulations that are formed layering processes similar to the one used here.

Using this new material system, we chose to encapsulate progenitor cells – NSCs and MSCs – towards the development of materials platforms that might ultimately enhance cell delivery or support cell survival and phenotype in therapies, as delivery of naïve cells through a needle often associates with low viability[5]. With respect to NSCs, interactions with HA through the CD44 receptor play important roles in maintaining NSC stemness and differentiation[70,71]. HA has also been shown to influence MSC phenotype in cell therapy for cartilage regeneration[72,73]. Further material design to include instructive cues is possible using the same conjugation methods as those used to introduce fluorophores. We showed NSCs could be encapsulated in minimal coatings with high viability, although we observed significant decreases of viability in 4-layer conformal encapsulations in later time points: at 1 day and beyond. However, encapsulating NSCs as spheroids negated decreases in viability, suggesting that lack of cell-cell interaction when NSCs are encapsulated as single cells contributed to the loss of viability.

MSCs exhibited higher viability and tendency to escape encapsulation with time compared to NSCs. We did not optimize our system for long-term encapsulation. Cytoprotective and short-term surface modification may be exploited in certain applications, such as cell printing, where cells must be shielded from acute stress imposed by the extrusion process; and cellular assembly or patterning, where surface modification is needed for the initial positioning of cells. Additionally, expedient cell egress from encapsulation, as well as the ability for encapsulated cells to interact with their microenvironment and other cells, may prove beneficial in cell delivery applications, where therapeutic benefits rely on the activity of the delivered cells.

Studies of conformal encapsulations have demonstrated they convey cytoprotection from mechanical stresses, including shear during delivery by injection or extrusion in bioprinting applications[27,47,74]. Towards biofabrication, while the work presented here did not directly evaluate mechanical protection, we showed the reactive moieties on the outer layer of encapsulation can be utilized to spatially assemble cells. Microtissues assembled through complementary oligonucleotides coatings have been demonstrated[43,75]; here, our system offers similar capabilities, albeit limited to one complementary interaction: thiol-maleimide. The conformal hydrogel offers the potential for further cues to be engineered into the extracellular environments of assembled cells through HA modification and hydrogel design. Rapid elimination of engineered material may be desirable as cells begin to deposit their own ECM[67] and as cells or microtissues establish interactions with their surroundings. Additionally, external cues engineered into coatings might be used to direct delivery of cells to, or influence responses by, the surrounding tissue into which cells and microtissues are implanted.

The reactive moieties, such as the thiol functionality used in this study, also allow encapsulated cells to be patterned onto substrates with complementary chemistry. In comparison to other approaches, such as cell adherence to patterned RGD islands, in this paper we utilized photochemistry to achieve cell attachment over a short period of time: 10 minutes for cells to settle to the substrate surface then 1 minute of crosslinking. With the use of a photomask, this method potentially allows for the patterning of multiple cell types onto overlapping shapes. This method can be carried out in culture medium at 37 °C, so that the cells remain in controlled and supportive culture conditions at all times. Going forward, the patterned cells might serve as another substrate for subsequent reactions; for example, thiol-coated cells patterned onto the norHA substrate can serve as reaction sites for the addition of maleimide-coated cells, allowing complex, cell dense structures to be assembled.

Conclusions:

Conformal hydrogels enable minimal volumes of engineered material to be used to protect encapsulated cells and influence phenotype and fate. These systems have potential applications in cell delivery, biofabrication, and systems designed to control interactions of the cells with their immediate surroundings or influence the interactions of the surroundings with the cell via the encapsulation material. The encapsulation system presented here featured an HA-based system that utilized a dual-modified HA, lipHASH, to encapsulate NSCs, for which few encapsulation systems have been demonstrated, and MSCs. We showed that the interactions of cells with the conformal hydrogel encapsulation was dependent both on cell type and material design, with the duration of cell encapsulation and cell viability being modulated by hydrogel properties. We also showed that conformal encapsulations could be used to direct cellular aggregation into multicellular assemblies and organization into designed, high-resolution patterns using photolithography. Given the extent of functionality which can be engineered into soft biomaterials, such as HA-based hydrogels, these systems offer opportunities for using biomaterials approaches to influence cell fate within minimal material environments, at the resolution of individual cells. This hydrogel represents a new, versatile material system that might be used in conformal encapsulations in the delivery of cells in cell-based therapies, in the assembly of cells 3D systems for expansion or culture in vitro, in directing interactions with tissue environments in vivo, and in assembling complex, cell-dense tissue constructs.

References:

1. Duff, R. G. (1985). Microencapsulation technology: A novel method for monoclonal antibody production. In Trends in Biotechnology.
2. G. D. Nicodemus and S. J. Bryant, https://home.liebertpub.com/teb, 2008, 14, 149–165.
3. J. L. Wilson and T. C. Mcdevitt, Biotechnology and Bioengineering, 2013, 110, 667–682.
4. O. Hasturk and D. L. Kaplan, Acta Biomaterialia, 2019, 95, 3–31.
5. H. Lee, N. Kim, H. B. Rheem, B. J. Kim, J. H. Park and I. S. Choi, Advanced Healthcare Materials, 2021, 10, 2100347.
6. B. A. Aguado, W. Mulyasasmita, J. Su, K. J. Lampe and S. C. Heilshorn, Tissue Engineering Part A, 2012, 18, 806–815.
7. J. Lam, W. E. Lowry, S. T. Carmichael and T. Segura, Advanced Functional Materials, 2014, 24, 7053–7062.
8. C. M. Madl, B. L. Lesavage, R. E. Dewi, C. B. Dinh, R. S. Stowers, M. Khariton, K. J. Lampe, D. Nguyen, O. Chaudhuri, A. Enejder and S. C. Heilshorn, Nature Materials, 2017, 16, 1233–1242.
9. C. M. Madl, B. L. LeSavage, R. E. Dewi, K. J. Lampe and S. C. Heilshorn, Advanced Science, 2019, 6, year.
10. R. G. Duff, Microencapsulation technology: A novel method for monoclonal antibody production, 1985.
11. G. M. O’Shea and A. M. Sun, Diabetes, 1986, 35, 943–946.

12. M. Y. Fan, Z. P. Lum, X. W. Fu, L. Levesque, I. T. Tai and A. M. Sun, Diabetes, 1990, 39, 519–522.
13. A. J. Hwa and G. C. Weir, Transplantation of Macroencapsulated Insulin-Producing Cells, 2018, https://doi.org/10. 1007/s11892-018-1028-y.
14. G. Romero, J. J. Lilly, N. S. Abraham, H. Y. Shin, V. Balasubramaniam, T. Izumi and B. J. Berron, ACS Applied Materials and Interfaces, 2015, 7, 17598–17602.
15. P. J. Wu, H. Peng, C. Li, A. Abdel-Latif and B. J. Berron, ACS Applied Bio Materials, 2020, 3, 2930–2939.
16. H. F. Ding, R. Liu, B. G. Li, J. R. Lou, K. R. Dai and T. T. Tang, Biochemical and Biophysical Research Communications, 2007, 362, 923–927.
17. A. J. Ryan, H. S. O'Neill, G. P. Duffy and F. J. O'Brien, Current opinion in pharmacology, 2017, 36, 66–71.
18. G. Basta and R. Calafiore, Current diabetes reports, 2011, 11, 384–391.
19. A. A. Tomei, V. Manzoli, C. A. Fraker, J. Giraldo, D. Velluto, M. Najjar, A. Pileggi, R. D. Molano, C. Ricordi, C. L. Stabler and J. A. Hubbell, Proceedings of the National Academy of Sciences of the United States of America, 2014, 111, 10514– 10519.
20. J. L. Lilly, G. Romero, W. Xu, H. Y. Shin and B. J. Berron, Biomacromolecules, 2015, 16, 541–549.
21. M. Germain, P. Balaguer, J. C. Nicolas, F. Lopez, J. P. Esteve, G. B. Sukhorukov, M. Winterhalter, H. Richard-Foy and D. Fournier, Biosensors and Bioelectronics, 2006, 21, 1566–1573.

22. S. Zhao, L. Zhang, J. Han, J. Chu, H. Wang, X. Chen, Y. Wang, N. Tun, L. Lu, X. F. Bai, M. Yearsley, S. Devine, X. He and J. Yu, ACS Nano, 2016, 10, 6189–6200.
23. S. Krol, S. Del Guerra, M. Grupillo, A. Diaspro, A. Gliozzi and P. Marchetti, Nano Letters, 2006, 6, 1933–1939.
24. M. Borkowska, E. Godlewska, M. Antosiak-Iwan´ska, J. Kinasiewicz, M. Borkowska, E. Godlewska, M. AntosiakIwa´nskaiwa´nska, J. Kinasiewicz, M. Strawski, M. Szklarczyk and L. H. Granicka, Article in Journal of Biomedical Nanotechnology, 2012, 8, 1–6.
25. S. Mansouri, Y. Merhi, F. M. Winnik and M. Tabrizian, Biomacromolecules, 2011, 12, 585–592.
26. W. Li, T. Guan, X. Zhang, Z. Wang, M. Wang, W. Zhong, H. Feng, M. Xing and J. Kong, ACS Applied Materials and Interfaces, 2015, 7, 3018–3029.
27. J. Hwang, D. Choi, M. Choi, Y. Seo, J. Son, J. Hong and J. Choi, ACS Applied Materials and Interfaces, 2018, 10, 17685–17692.
28. J. Yang, J. Li, X. Li, X. Wang, Y. Yang, N. Kawazoe and G. Chen, Biomaterials, 2017, 133, 253–262.
29. D. Choi, H. Lee, H.-B. Kim, M. Yang, J. Heo, Y. Won, S. Soon Jang, J. Kuk Park, Y. Son, T. In Oh, E. Lee and J. Hong, 2017.
30. Y. Fukuda, T. Akagi, T. Asaoka, H. Eguchi, K. Sasaki, Y. Iwagami, D. Yamada, T. Noda, K. Kawamoto, K. Gotoh, S. Kobayashi, M. Mori, Y. Doki and M. Akashi, Biomaterials, 2018, 160, 82–91.

31. Y. Sasano, K. Fukumoto, Y. Tsukamoto, T. Akagi and M. Akashi, Journal of Bioscience and Bioengineering, 2020, 129, 749–755.
32. I. Koh, I. Yong, B. Kim, D. Choi, J. Hong, Y. M. Han and P. Kim, ACS Biomaterials Science and Engineering, 2020, 6, 813–821.
33. S. Sakai and M. Taya, ACS Macro Letters, 2014, 3, 972–975.
34. M. R. Dzamukova, E. A. Naumenko, E. V. Rozhina, A. A. Trifonov and R. F. Fakhrullin, Nano Research, 2015, 8, 2515– 2532.
35. J. H. Park, K. Kim, J. Lee, J. Y. Choi, D. Hong, S. H. Yang, F. Caruso, Y. Lee and I. S. Choi, Angewandte Chemie International Edition, 2014, 53, 12420–12425.
36. J. Lee, J. Choi, J. H. Park, M.-H. Kim, D. Hong, H. Cho, S. H. Yang and I. S. Choi, Angewandte Chemie International Edition, 2014, 53, 8056–8059.
37. B. J. Kim, T. Park, H. C. Moon, S. Y. Park, D. Hong, E. H. Ko, J. Y. Kim, J. W. Hong, S. W. Han, Y. G. Kim and I. S. Choi, Angewandte Chemie International Edition, 2014, 53, 14443–14446.
38. J. Yang, Y. Yang, N. Kawazoe and G. Chen, Biomaterials, 2019, 197, 317–326.
39. Y. Teramura, O. P. Oommen, J. Olerud, J. Hilborn and B. Nilsson, Biomaterials, 2013, 34, 2683–2693.
40. M. Matsusaki, K. Kadowaki, Y. Nakahara and M. Akashi, Angewandte Chemie International Edition, 2007, 46, 4689–4692.
41. K. Kadowaki, M. Matsusaki and M. Akashi, Langmuir, 2010, 26, 5670–5678.
42. S. Toda, A. Fattah, K. Asawa, N. Nakamura, K. N. Ekdahl, B. Nilsson and Y. Teramura, Micromachines, 2019, 10, 755.

43. A. A. Stock, V. Manzoli, T. De Toni, M. M. Abreu, Y. C. Poh, L. Ye, A. Roose, F. W. Pagliuca, C. Thanos, C. Ricordi and A. A. Tomei, Stem Cell Reports, 2020, 14, 91–104.
44. Z. J. Gartner and C. R. Bertozzi, Proceedings of the National Academy of Sciences, 2009, 106, 4606–4610.
45. J. S. Liu and Z. J. Gartner, Trends in Cell Biology, 2012, 22, 683–691.
46. N. G. Veerabadran, P. L. Goli, S. S. Stewart-Clark, Y. M. Lvov and D. K. Mills, Macromolecular Bioscience, 2007, 7, 877–882.
47. S. Miura, Y. Teramura and H. Iwata, Biomaterials, 2006, 27, 5828–5835.
48. A. S. Mao, J. W. Shin, S. Utech, H. Wang, O. Uzun, W. Li, M. Cooper, Y. Hu, L. Zhang, D. A. Weitz and D. J. Mooney, Nature Materials, 2017, 16, 236–243.
49. A. S. Mao, B. Özkale, N. J. Shah, K. H. Vining, T. Descombes, L. Zhang, C. M. Tringides, S. W. Wong, J. W. Shin, D. T. Scadden, D. A. Weitz and D. J. Mooney, Proceedings of the National Academy of Sciences of the United States of America, 2019, 116, 15392–15397.
50. Z. L. Zhi, B. Liu, P. M. Jones and J. C. Pickup, Biomacromolecules, 2010, 11, 610–616.
51. D. Hachim, J. Melendez and R. Ebensperger, Journal of Encapsulation and Adsorption Sciences, 2013, 03, 1–12.
52. G. Marchioli, L. Zellner, C. Oliveira, M. Engelse, E. d. Koning, J. Mano, Karperien, A. v. Apeldoorn and L. Moroni, Journal of Materials Science: Materials in Medicine, 2017, 28, year.

53. C. B. Highley, G. D. Prestwich and J. A. Burdick, Current Opinion in Biotechnology, 2016, 40, 35–40.

54. J. A. Burdick and G. D. Prestwich, Advanced Materials, 2011, 23, H41–H56.

55. S. Sahoo, C. Chung, S. Khetan and J. A. Burdick, Biomacromolecules, 2008, 9, 1088–1092.

56. J. L. Holloway, H. Ma, R. Rai and J. A. Burdick, Journal of Controlled Release, 2014, 191, 63–70.

57. C. B. Rodell, J. W. MacArthur, S. M. Dorsey, R. J. Wade, L. L. Wang, Y. J. Woo and J. A. Burdick, Advanced Functional Materials, 2015, 25, 636–644.

58. W. M. Gramlich, I. L. Kim and J. A. Burdick, Biomaterials, 2013, 34, 9803–9811.

59. M. G. Grewal, V. P. Gray, R. A. Letteri and C. B. Highley, Biomaterials Science, 2021, 9, 4374–4387.

60. L. S. Campos, Journal of Neuroscience Research, 2004, 78, 761–769.

61. D. Mushahary, A. Spittler, C. Kasper, V. Weber and V. Charwat, Cytometry Part A, 2018, 93, 19–31.

62. X. Wei, X. Yang, Z. P. Han, F. F. Qu, L. Shao and Y. F. Shi, Acta Pharmacologica Sinica 2013 34:6, 2013, 34, 747–754.

63. B. J. Jones and S. J. McTaggart, Experimental Hematology, 2008, 36, 733–741.

64. J. Galipeau and L. Sensébé, Cell Stem Cell, 2018, 22, 824–833.

65. A. M. Kloxin, A. M. Kasko, C. N. Salinas and K. S. Anseth, Science, 2009, 324, 59–63.

66. M. E. Todhunter, N. Y. Jee, A. J. Hughes, M. C. Coyle, A. Cerchiari, J. Farlow, J. C. Garbe, M. A. LaBarge, T. A. Desai and Z. J. Gartner, Nature Methods 2015 12:10, 2015, 12, 975–981.

67. X. Zhou, H. Wu, H. Wen and B. Zheng, Micromachines 2022, Vol. 13, Page 80, 2022, 13, 80.

68. C. Loebel, R. L. Mauck and J. A. Burdick, Nature Materials, 2019, 1.

69. D. Rabuka, M. B. Forstner, J. T. Groves and C. R. Bertozzi, Journal of the American Chemical Society, 2008, 130, 5947–5953.

70. K. Tatsumi, K. Ohashi, Y. Teramura, R. Utoh, K. Kanegae, N. Watanabe, S. Mukobata, M. Nakayama, H. Iwata and T. Okano, Biomaterials, 2012, 33, 821–828.

71. W. Su, S. C. Foster, R. Xing, K. Feistel, R. H. Olsen, S. F. Acevedo, J. Raber and L. S. Sherman, Journal of Biological Chemistry, 2017, 292, 4434–4445.

72. Z. Z. Khaing and S. K. Seidlits, Journal of Materials Chemistry B, 2015, 3, 7850–7866.

73. L. Bian, M. Guvendiren, R. L. Mauck and J. A. Burdick, Proceedings of the National Academy of Sciences, 2013, 110, 10117–10122.

74. M. Y. Kwon, C. Wang, J. H. Galarraga, E. Puré, L. Han and J. A. Burdick, Biomaterials, 2019, 222, 119451.

75. A. Matsuzawa, M. Matsusaki and M. Akashi, Langmuir, 2013, 29, 7362–7368.

76. M. E. Todhunter, N. Y. Jee, A. J. Hughes, M. C. Coyle, A. Cerchiari, J. Farlow, J. C. Garbe, M. A. Labarge, T. A. Desai, Z. J. Gartner, M. E. T. Conceived and J. C. G. Performed, Nat Methods, 2015, 12, 975–981.

Chapter 3. Identifying opportunities for cell fate control through unique features in granular hydrogels

Our cellular encapsulation approach demonstrated possibilities for using biomaterials to control cellular environment and generate multicellular structures. As described below, this served as the basis for further collaborative studies on the material's role in guiding cellular assembly in a vasculature model. Concurrently, I began working with granular hydrogels and identified opportunities that would serve as the basis for the development of a unique, porous granular system, which I will describe in the later part of this chapter.

PART I: Discussion of cell encapsulation potentials and further work

Our encapsulation technology, being based on biocompatible, natural hydrogels to which thiolated biofunctionalities could easily be conjugated, could offered potential beyond protective encapsulation and cell assembly. However, there are significant bottlenecks that need to be overcome, which led to my focus on the latter part of my thesis using a different system, granular hydrogels, to achieve cell-instructive biomaterials.

A primary challenge exists in the synthesis of the materials. The material we used for insertion into the cellular membrane, lipHASH, requires prolonged synthesis process and time from commercially obtainable sodium hyaluronate. Additionally, lipHASH, as well as HASH and MaHA used in encapsulation present some challenges in long-term storage due to their high reactivity.

Secondly, while our material chemistry can, in theory, support unlimited layering, a small percentage of cells were lost to each washing process that can accrued as the number of layers increases. Combined with the process time, this also presents limitations to the system. Additionally, as shown in the previous chapter, both NSCs and MSCs stop interacting with their environment at higher numbers of layers; however, as the number of layers increased, cell viability tended to become lower. Further optimization may be required if the material system were to be applied to provide protection against immune responses, where cell surface antigens need to be masked. Further, while we did not conduct any studies on the coatings protective effect from needle extrusion, we speculate that higher numbers of layers are also needed to achieve a significant effect. Again, loss in cell number and viability from adding layers of encapsulation to achieve protection may outweigh the benefit brought about by increased protection during injection. Especially when cell death from injection could also be rescued by increasing the needle size, at the expense of having somewhat more robust inflammatory responses[1].

Therefore, to achieve cytoprotective effects using this system, extensive modifications and optimizations are needed to materials that are already complex. On the other hand, the assembly-mediating capability was quite exciting for us: lipHASH provides us with a molecule that can be inserted into any cell surface without compromising cell viability. Without forming a crosslinked encapsulation, lipHASH would disappear from the cell surface over a period of 24 hours, presumably due to a combination of endocytosis and spontaneous detachment and thermal diffusion into the surrounding solution. This transient interaction, however, may prove useful in establishing cellular assemblies. The material could serve as the initial guide that places cells near each other or onto a substrate. As cell-cell or cell-substrate interactions occur over a period of hours, the material slowly leaves the cell surface, leaving only cellular interactions in place.

In fact, when I presented these findings in an Society for Biomaterials 2022 Annual Meeting in Baltimore, Dr. Nan Zhao, who was presenting a poster across from mine, saw the opportunity to use this material for exactly this purpose in the project he was working on.

Dr. Zhao was, at that time, a postdoc in Dr. Peter Searson's group at Johns Hopkins, working on an *in vitro* model of the arteriole. Briefly, an arteriole consists of an endothelium wrapped within smooth muscle cells (SMCs). To recapitulate this key characteristic, the Searson group utilized a microfluidic device with a center channel amenable to cell seeding (Figure 1). As illustrated in Figure 1, SMCs were first seeded to the walls of the

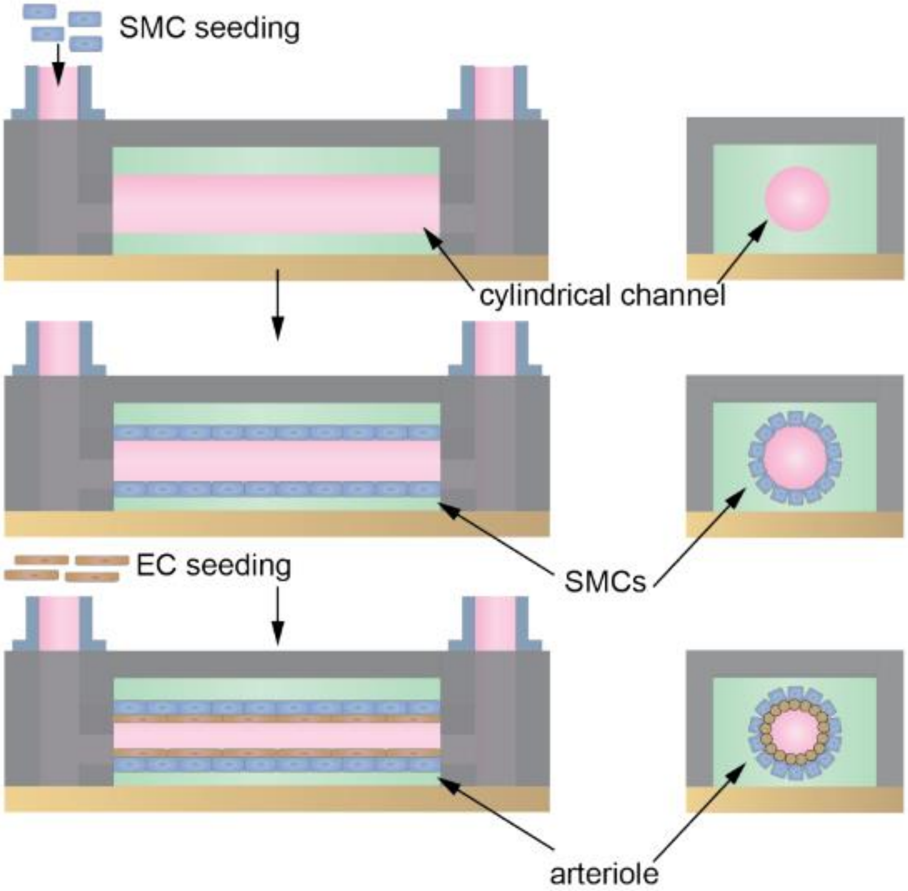

Figure 1. Schematic for creating an in vitro arteriole model. Credits to Dr. Nan Zhao in the Searson group.

channel to create a confluent layer. Subsequently, endothelial cells (ECs) would be seeded, in an attempt to create another confluent EC layer over the SMC layer.

EC layering, however, proved to be problematic. In physiological systems, vasculogenesis does not start with the formation of the SMC layer, but rather the endothelial layer, which in turn recruits SMCs and stromal cells[2]. Doing it in reverse resulted in low adhesions of ECs – ligands present on SMCs are not adept at supporting ECs that have not formed a stable endothelial layer. As shown in Figure 2B, direct seeding of ECs resulted in ECs competing for channel adhesion with SMCs and heterogenous distributions, rather than ECs adhering to SMCs.

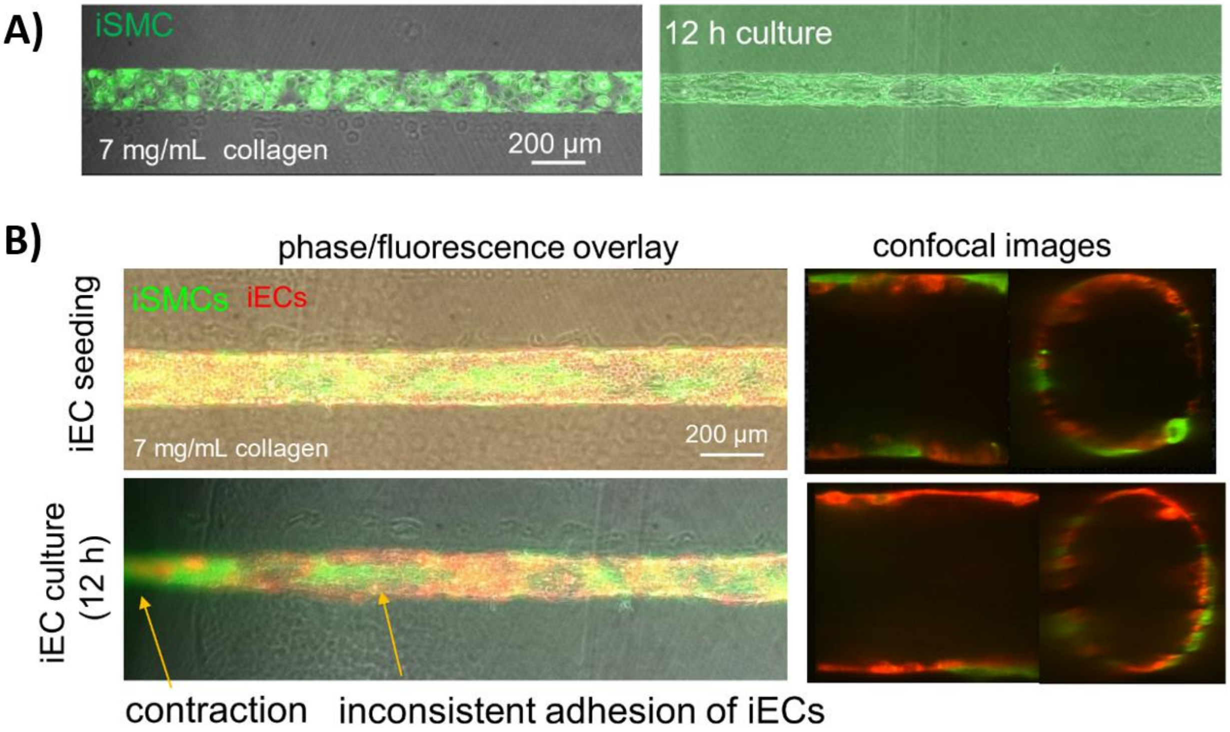

Figure 2. A) SMC seeded channel forms a confluent layer after 12 hours of culture. **B)** Seeding ECs onto SMC lined channels resulted in uneven adhesion and little adhesion of ECs to SMCs. Image credits to Dr. Nan Zhao in the Searson group.

When I chatted with Dr. Zhao at the conference, he was exploring ways to attach adhesive ligands (ECM molecules such as collagen and laminin). Interestingly, he was also using lipid-modified small molecules, in addition to small molecules that can be covalently attached to the surfaces. However, cellular viability was low, presumably due to the high number of molecules on the cell surface, disrupting the membrane and/or other cellular signaling activities occurring on the membrane. In our material system, the lipHASH molecule was synthesized to have an average of 1 lipid present on each chain of the HA polysaccharide. However, for each chain of the polysaccharide, many SH (thiol) groups are present. As the thiol groups are the reactive sites that facilitate further conjugation, this means that for each lipid insertion, our system creates a great number of reactive sites. While the small molecules modified with lipid has a 1:1 reactive group to lipid ratio, for our system, a common molecular weight of 60kDA with a thiol degree of substitution (DoS) of 0.3 provides ~50:1 reactive group to lipid ratio. We hypothesize that the reduction in lipid insertion will reduce the cell death they were seeing. And the present of thiol groups provide convenient conjugation sites for the ECM molecules that the Searson group was already using.

To test if our material system would facilitate conjugation of adhesion molecules and the subsequent attachment of ECs, we synthesized lipHASH at 0.35 DoS. The Searson group conjugated gelatin, a cell attachment molecule derived from collagen, with maleimide. Incubation of lipHASH on confluent layers of SMCs showed that lipHASH attached consistently and evenly to the SMC surfaces at a concentration of 0.5mg/mL (Figure 3A, see the materials and methods section of this chapter for experimental details).

Subsequent incubation of lipHASH-coated cells in gelatin maleimide (G-M) tagged with FITC (G-M-F) showed splotchy, but strong signals indicating gelatin attachment to the cell surfaces (Figure 3B). After gelatin attachment, ECs were cultured on top of the SMCs for a day before imaging. Here, we qualitatively observed that while having the conjugated gelatin increased the initial seeding density of ECs by a small amount, EC spreading and morphology was not changed (Figure 4).

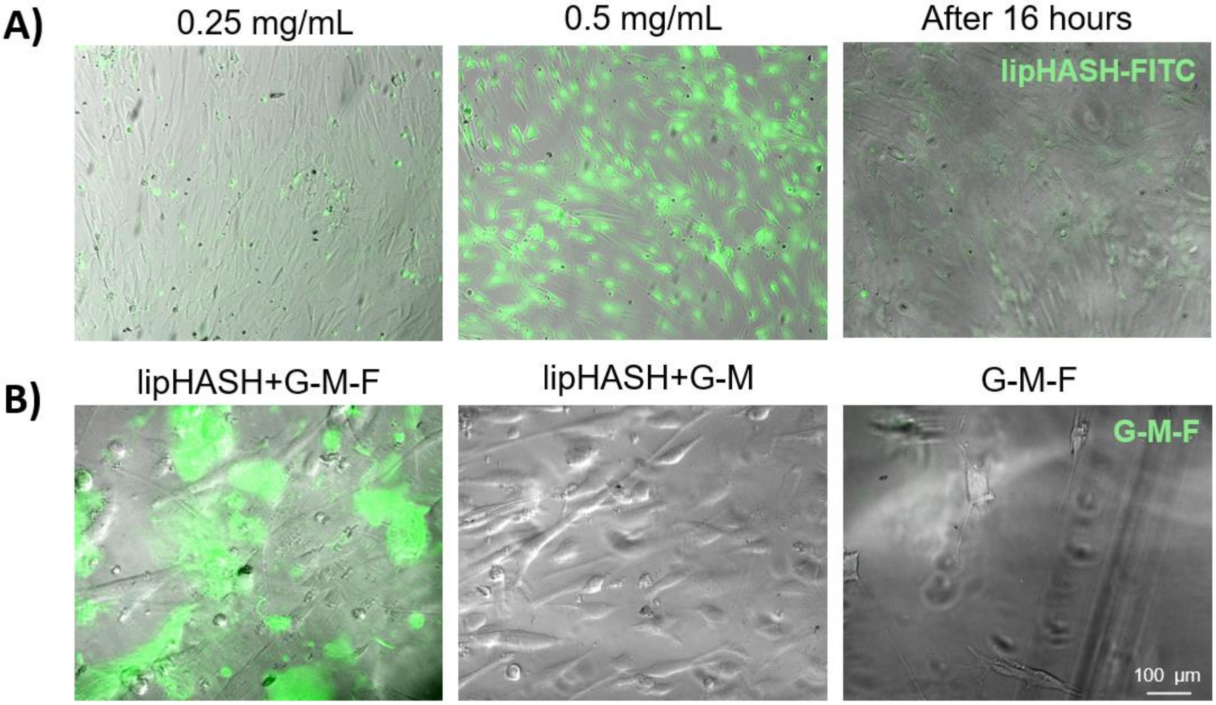

Figure 3. A) SMC monolayers cultured with lipHASH-FITC solution with varying concentrations then washed; and 16 hours after incubation in 0.5mg/mL lipHASH-FITC solution. **B)** Gelatin maleimide incubation after incubation with and without 0.5mg/mL lipHASH. Image credits to Dr. Nan Zhao in the Searson group.

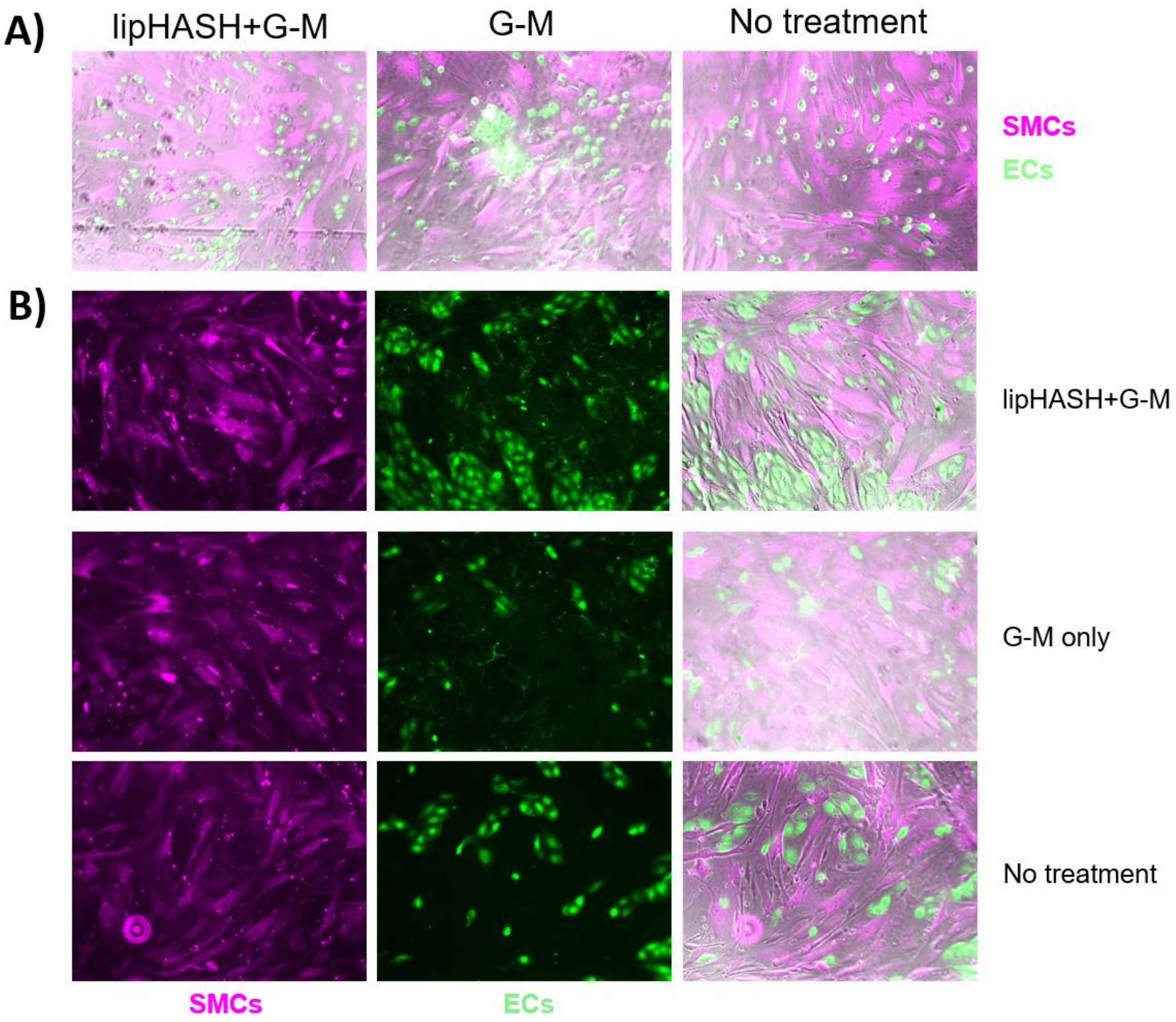

Figure 4. A) 30 minutes after seeding ECs (green) on confluent layers of SMCs (deep red) treated with indicated groups. **B)** 1 day after EC seeding on SMCs treated with indicated groups. Image credits to Dr. Nan Zhao in the Searson group.

The experiments were not carried out further due to other priorities in the Searson group. ECs were not able to spread on SMCs with lipHASH-G-M, likely due to the relatively weak interactions provided by lipid insertion. While the G-M attachment helped retain cells initially, cellular contractile forces following adhesion ligand (gelatin) attachment could have removed the lipHASH-G-M from the surface. This is supported by ECs not being able to spread, which is a result of integrin binding that requires formations of focal adhesions[4]. However, this experiment further demonstrated the reproducibility and capability of the lipHASH system: lipHASH was able to consistently cover cell surfaces and supported secondary attachment of gelatin. Crosslinking of lipHASH to form a more stable layer prior to attaching gelatin could provide ECs with a better substrate upon which to spread.

In conclusion, while further optimization is required toward providing cellular protection, our material system provides a versatile and cytocompatible platform for cellular assembly. This system could be used to provide temporary, but precise patterning of cells onto substrates, as well as with each other. Upon further optimization, this system holds promises for engineering cell-dense tissues with precise control over cell type and positioning.

PART II: Exploring potentialities in granular hydrogel scaffolds

In continuing to engineer biomaterials to influence cell fates beyond cellular encapsulation, I also began to pursue possibilities using jammed hydrogel microparticles (HMPs), a class of materials with seemingly improbable, but very convenient properties. In short, hydrogels, when made into particles typically 10-100s of μm in diameter, can be packed together. As the packing of particles becomes tighter, the packed particles stop being able to flow and roll past one another. Instead, they form a solid structure without needing any adhesive forces among particles. This change in bulk flow behavior is termed the "jamming transition"[4-5]. A great example of jammed particles is toothpaste, which, though not a hydrogel, is composed of tightly packed particles. The packed toothpaste particles give toothpaste the special property of 1) being able to be squeezed out of the tube, and 2) staying as a solid and not rolling down our toothbrushes after having been placed.

The solid structures formed by jammed HMPs are typically called “granular hydrogels”: a multitude of granules that are, in themselves, hydrogels, jammed together to form a bulk solid. In recent years, many groups have been experimenting with the granular hydrogel system; mainly due to two unique properties that makes the system highly convenient and attractive for tissue engineering and regenerative applications.

The first is the ability of the HMPs to flow past each other when an external force is applied. While granular hydrogels remain solid-like at rest, HMPs are held together only by the compressive forces they exert on each other[6]. Overcoming the compressive forces holding the HMPs together is relatively easy due to the lack of other adhesive or attractive interactions among HMPs. On the macroscopic level, this means that most granular hydrogels can be injected through a needle, as shown by various groups that have utilized the granular system as injectable therapies[7], as well as in 3D printing applications[8]. Compared to injectable bulk hydrogels made up of polymer networks, granular hydrogel systems have a decided advantage. In order for bulk hydrogels to be injectable without breaking, reversible bonds are needed so that the polymer network can break to allow for injection, then reform after injection is complete. This typically requires non-covalent interactions[9,10] or dynamic covalent bonds[11] that introduce many limitations and complexities to material choice and design. In contrast, the injectability of granular hydrogels comes not from the characteristics of bonds between polymers, but the physical interactions between HMPs, which break and reform without needing additional attractive forces. As most hydrogels can be processed to form microparticles, HMP-based approaches can decouple the design of hydrogel molecular structure from injectability. This allows for a huge range of hydrogels to become injectable, as long as they can be fabricated into the form of HMPs, or even other irregular shapes that can be packed together[12-14]. Beyond injectability, the ability for granular hydrogels to flow easily yet remain a solid when unperturbed is very desirable for laboratory transfer and processing. Bulk hydrogels typically remain in liquid form prior to crosslinking, necessitating the need for molds and containers that hold liquid in place. Additionally, incorporating of cells into bulk hydrogels, done very commonly to achieve 3D culture of cells, typically require constant agitation of the cell-liquid mixture as the precursor crosslinks, so that cells do not sink to the bottom of the hydrogel and create heterogenous distributions. Granular hydrogels exhibit liquid behaviors but forms a free-standing solid structure at rest, thus eliminating the requirement of a mold and enabling formation of more complex structures. Additionally, cells can be mixed into granular hydrogels and reside in the interstitial spaces between the HMPs with minimal movement, again reducing experimental complexities and in turn, broadening the use and applications of 3D culture systems.

The other property unique to the granular hydrogel system is its inherent porosity. Packing of spherical particles is inefficient and leaves void spaces between the particles. For HMPs with 10s – 100s μm in diameter, even when packed, void spaces between HMPs are on the scale of 10s of μm in size, spacious enough for cells to reside and migrate into[7]. Further, the total void space, or porosity, as well as the pore sizes, can be tuned by changing the packing density and HMP sizes, respectively. Bulk hydrogels, on the other hand, typically possess only nanoscale porosity within the crosslinked polymer meshes that comprise their molecular structures. The nanoscale porosity limits diffusion and cell movement. Though porosity and permissiveness of the hydrogel polymer mesh can be engineered by using strategies such as using sacrificial materials[15,16], 3D printing[17], and material chemistry that allow for degradation[18] and malleability[3,19]; granular hydrogels are positioned to support cells without requiring extensive engineering.

One of the most cited examples showcasing the benefits of granular hydrogel porosity is the microporous annealed particle (MAP) scaffolds developed by Dr. Tatiana Segura, Dr. Donald Griffin, and Dr. Dino Di Carlo[7]. In their seminal paper, PEG-based HMPs were packed together to form granular hydrogels. The granular hydrogel was then secondarily crosslinked using excess reactive groups on the HMP surfaces to form MAP scaffolds. The secondary crosslinking is important in stabilizing the granular hydrogel. Without this, while granular hydrogels consisting of uncrosslinked HMPs remains a solid at rest, submersion of granular hydrogels in solution will quickly result in their dissociation. Griffin et al. found that incorporation of stromal cells in MAP scaffolds resulted in much better proliferation and spreading compared to stromal cells incorporated in non-porous bulk scaffolds. More strikingly, when used in a murine skin wound closure model, MAP-treated mice resulted in ~40% wound closure, double that of the no treatment group (~20%). Non-porous bulk hydrogel-treated mice, on the other hand, only had ~7% wound closure. Additionally, significant infiltration of vascular cells and other cell types enabled large-scale tissue structure formation within the MAP scaffolds.

Since then, efforts from many groups have shown beneficial effects of granular hydrogels in regeneration of muscle[20] and cartilage[21]. Injectable MAP formulations in which particles can bind with each other through physical interactions have been developed for tissue repair after stroke[22,23]. Further, fabrication of granular hydrogels in shapes other than spheres are being explored to simplify production[13] and alter system characteristics such as flow behavior and void space[24], all of them showing great propensity for cellular support.

Needless to say, I was very excited when I had the chance to work on a project in a collaboration among my own advisor, Dr. Chris Highley; one of the original creators of MAP scaffolds, Dr. Donald Griffin; and an expert in mesenchymal stromal cell (MSC) biology, Dr. Ross Marklein. In working with HMPs comprising MAP, however, I quickly found that our centrifuge was not quite powerful enough to sufficiently jam the HMPs. Specifically, a 15% decrease, with a final relative centrifugal force (rcf) of 21,130 compared to 25,000 rcf used in the Griffin lab, did not support the final crosslinking of the HMPs into a network. Presumably due to insufficient interparticle contacts that are key to stabilizing the final scaffold. This insight led me to rethink the design of granular scaffolds, as in granular hydrogels, the magnitude of granular hydrogel porosity is altered by the degree of packing, with pores and porosity becoming smaller as packing density increases[12,24]. However, if a high degree of packing is needed to crosslink and stabilize the granular hydrogel, porosity, and the magnitude change in porosity become limited as decreased packing quickly renders the granular hydrogel unable to be crosslinked. I became interested in attempting to address this challenge, by finding a way to decouple the packing density requirement and the achievable porosity in granular scaffolds, as well as methods to stabilize granular scaffolds.

Porosity is the hallmark of granular hydrogels and provides great benefits in supporting cell growth, as shown for MAP scaffolds[7]. However, even in microporous granular hydrogels, cells can benefit from higher porosity and pore sizes. Anderson et al. showed that increased particle fraction (decreased porosity), or packing density, resulted in decreased mesenchymal cell growth and slower macromolecular diffusion[25]. Qazi et al. showed that decreasing packing density (increased porosity) enhanced the sprouting of HUVEC/MSC spheroids. Spheroid sprouting was also enhanced when the packing density is kept the same, but the sizes of the particles increased[24] (increased pore sizes). So far, controlling porosity characteristics in granular hydrogels is typically done by changing the sizes of the particles to change the pore sizes; and changing the density of particle packing to change the total porosity. Both approaches present some challenges as 1) pore size is limited by the size of particles. Granular hydrogel formulation such as MAP has pore sizes on the order of 10s of μm with particle diameter of ~100 μm. Much larger particles with millimeter scale diameter might be needed to achieve pore sizes on the scale of 100 μm. However, macroscale particles will become hard to process using pipettes with small inlet diameters, as well as potentially change the jamming behavior undesirably. 2) Changing particle packing alters the flow behavior of the granular hydrogel and is limited by particle contacts. Porosity is increased as particle packing density decreases, or, in other words, the amount of interstitial solution increases, effectively diluting the particles. There are challenges in this process. First, loosely packed granular hydrogels are easier to flow, but harder to hold solid-like structures at rest, bringing potential undesired behavior for certain applications. Second, “loose” vs “dense” packings are not standardized, strategies for changing packing density includes varying centrifugation speed, drying the particles on a filter[12,24], as well as lyophilizing the particles then adding back calculated volumes of solution[25]. While the last method can be done reproducibly and can precisely control the particle fraction, lyophilization of the particles is difficult to achieve and will likely require different strategies for different materials[26]. As for the rest, further characterization of “loosely packed” and “densely packed” granular hydrogels are needed to elucidate the porosity of the system. Lastly, dilution of the particles cannot be increased indefinitely. Particles eventually exit the jammed state as the packing density decreases and lose contact with each other. This, again, takes away from the jammed behavior desirable in many applications, and more importantly, limits the porosity that can be achieved in granular hydrogels.

In the next chapter, I will detail our attempt to address these limitations by engineering a granular hydrogel scaffold that is easy to fabricate, easy to crosslink, and can achieve controlled porosity independent of the packing process. Further, as increasing porosity has shown beneficial effects on cellular infiltration and growth, we also devised a method that can create porosity beyond the current approaches while keeping the highly porous scaffold stable for long-term culture.

Materials and Methods for PART I

Synthesis and preparation of lipHASH and gelatin maleimide:

LipHASH is synthesized as described in the previous chapter. HA:Boc2O:SH ratio is adjusted to achieve 0.4 degree of thiol substitution. Purified lipHASH is stored in solution along with tris(2-carboxyethyl)phosphine (TCEP) at a 2:1 SH:TCEP molar ratio in -80C and shipped to Johns Hopkins on dry ice. Gelatin maleimide is synthesized by Dr. Nan Zhao in the Searson group.

Assessing lipid insertion into SMC membrane

LipHA-FITC was lyophilized and reconstituted in PBS before use. To assess if lipid-HA inserts into and are retained on the cellular membrane, SMCs were first cultured until a confluent monolayer formed. LipHA-FITC dissolved at 0mg/mL, 0.25mg/mL, or 0.5mg/mL in PBS was added to the SMCs and allowed to incubate for 1 hour. The SMCs were subsequently washed with PBS and observed for FITC signal over a period of 16 hours.

Assessing gelatin attachment to lipHASH

LipHASH (non-fluorescent) was lyophilized and reconstituted in PBS at 0.5mg/mL before use. pH of the lipHASH solution was tested and adjusted to 7 using 0.1mM NaOH and 0.1mM HCl. SMC monolayer was incubated in either PBS or lipHASH solution for an hour and washed with PBS. Then, gelatin-maleimide-FITC (G-M-F) or gelatin-maleimide (G-M) was incubated for another 2 hours before PBS washing and imaging.

Endothelial cell culture on SMC monolayers

SMCs were incubated with PBS or lipHASH for 1 hour, then G-M for 2 hours, as described. After washing with PBS, endothelial cells (ECs) were seeded onto the SMC monolayer, EC attachment at spreading were assessed at the 30-minute time point, as well as at 1 day after seeding.

References:

1. Skuk, D., Goulet, M., & Tremblay, J. P. (2014). Intramuscular Transplantation of Myogenic Cells in Primates: Importance of Needle Size, Cell Number, and Injection Volume. Cell Transplantation, 23(1), 13–25.
2. Carmeliet, P. (2000). Mechanisms of angiogenesis and arteriogenesis. Nature Medicine 2000 6:4, 6(4), 389–395.
3. Lou, J., Stowers, R., Nam, S., Xia, Y., & Chaudhuri, O. (2018). Stress relaxing hyaluronic acid-collagen hydrogels promote cell spreading, fiber remodeling, and focal adhesion formation in 3D cell culture. Biomaterials, 154, 213–222.
4. Cates, M. E., Wittmer, J. P., Bouchaud, J.-P., & Claudin, P. (1998). Jamming is not just cool any more. Nature 1998 396:6706, 396(6706), 21–22.
5. Van Hecke, M. (2009). Jamming of soft particles: geometry, mechanics, scaling and isostaticity. Journal of Physics: Condensed Matter, 22(3), 033101.
6. O’hern, C. S., Silbert, L. E., Liu, A. J., & Nagel, S. R. (n.d.). *Jamming at zero temperature and zero applied stress: The epitome of disorder*.
7. Griffin, D. R., Weaver, W. M., Scumpia, P. O., di Carlo, D., & Segura, T. (2015). Accelerated wound healing by injectable microporous gel scaffolds assembled from annealed building blocks. Nature Materials 2014 14:7, 14(7), 737–744.
8. Highley, C. B., Hoon Song, K., Daly, A. C., Burdick, J. A., Highley, C. B., Song, K. H., Daly, A. C., & Burdick, J. A. (2019). Jammed Microgel Inks for 3D Printing Applications. Advanced Science, 6(1), 1801076.

9. Le, T. M. D., Jung, B. K., Li, Y., Duong, H. T. T., Nguyen, T. L., Hong, J. W., Yun, C. O., & Lee, D. S. (2019). Physically crosslinked injectable hydrogels for long-term delivery of oncolytic adenoviruses for cancer treatment. Biomaterials Science, 7(10), 4195–4207.

10. Pettinelli, N., Rodríguez-Llamazares, S., Bouza, R., Barral, L., Feijoo-Bandín, S., & Lago, F. (2020). Carrageenan-based physically crosslinked injectable hydrogel for wound healing and tissue repairing applications. International Journal of Pharmaceutics, 589, 119828.

11. Wang, L. L., Highley, C. B., Yeh, Y.-C., Galarraga, J. H., Uman, S., & Burdick, J. A. (2018). Three-dimensional extrusion bioprinting of single- and double-network hydrogels containing dynamic covalent crosslinks. Journal of Biomedical Materials Research Part A, 106(4), 865–875.

12. Qazi, T. H., Wu, J., Muir, V. G., Weintraub, S., Gullbrand, S. E., Lee, D., Issadore, D., & Burdick, J. A. (2022). Anisotropic Rod-Shaped Particles Influence Injectable Granular Hydrogel Properties and Cell Invasion. Advanced Materials, 34(12)

13. Muir, V. G., Qazi, T. H., Weintraub, S., Torres Maldonado, B. O., Arratia, P. E., Burdick, J. A.(2022). Sticking Together: Injectable Granular Hydrogels with Increased Functionality via Dynamic Covalent Inter-Particle Crosslinking. Small, 18(36), 2201115.

14. Tang, R. C., Shang, L., Scumpia, P. O., & di Carlo, D. (2023). Injectable Microporous Annealed Crescent-Shaped (MAC) Particle Hydrogel Scaffold for Enhanced Cell Infiltration. Advanced Healthcare Materials, 2302477.

15. Chiu, Y. C., Cheng, M. H., Engel, H., Kao, S. W., Larson, J. C., Gupta, S., & Brey, E. M. (2011). The role of pore size on vascularization and tissue remodeling in PEG hydrogels. Biomaterials, 32(26), 6045–6051.

16. Hwang, C. M., Sant, S., Masaeli, M., Kachouie, N. N., Zamanian, B., Lee, S. H., & Khademhosseini, A. (2010). Fabrication of three-dimensional porous cell-laden hydrogel for tissue engineering. Biofabrication, 2(3), 035003.

17. Miri, A. K., Khalilpour, A., Cecen, B., Maharjan, S., Shin, S. R., & Khademhosseini, A. (2019). Multiscale bioprinting of vascularized models. Biomaterials, 198, 204–216.

18. Sahoo, S., Chung, C., Khetan, S., & Burdick, J. A. (2008). Hydrolytically degradable hyaluronic acid hydrogels with controlled temporal structures. Biomacromolecules, 9(4), 1088–1092.

19. Whisler, J. A., Chen, M. B., & Kamm, R. D. (2014). Control of perfusable microvascular network morphology using a multiculture microfluidic system. Tissue Engineering - Part C: Methods, 20(7), 543–552.

20. Rodriguez, A., Griffin, D. R., & Christi, G. J. (2023, July). Cell-scale pores in microporous annealed particle (MAP) hydrogel implants promote regeneration in volumetric muscle loss injuries. In *TISSUE ENGINEERING PART A* (Vol. 29, No. 13-14).

21. Schaeffer, C., Pfaff, B. N., Cornell, N. J., Salopek, L. S., Shan, S., Viyar, J., Omesiete, W., Griffin, D. R., Cottler, P. S., & Degeorge, B. R. (2020). Injectable

Microannealed Porous Scaffold for Articular Cartilage Regeneration. Annals of Plastic Surgery, 84(6), S446–S450.

22. Sideris, E., Kioulaphides, S., Wilson, K. L., Yu, A., Chen, J., Carmichael, S. T., & Segura, T. (2022). Particle Hydrogels Decrease Cerebral Atrophy and Attenuate Astrocyte and Microglia/Macrophage Reactivity after Stroke. Advanced Therapeutics, 5(8), 2200048.
23. Wilson, K. L., Joseph, N. I., Onweller, L. A., Anderson, A. R., Darling, N. J., David-Bercholz, J., & Segura, T. (2023). SDF-1 Bound Heparin Nanoparticles Recruit Progenitor Cells for Their Differentiation and Promotion of Angiogenesis after Stroke. Advanced Healthcare Materials, 2302081.
24. Qazi, T. H., Muir, V. G., & Burdick, J. A. (2022). Methods to Characterize Granular Hydrogel Rheological Properties, Porosity, and Cell Invasion. ACS Biomaterials Science and Engineering, 8(4), 1427–1442.
25. Anderson, A. R., Nicklow, E., & Segura, T. (2022). Particle fraction is a bioactive cue in granular scaffolds. Acta Biomaterialia, 150, 111–127.
26. Anderson, A. R., & Segura, T. (2022). Controlling Particle Fraction in Microporous Annealed Particle Scaffolds for 3D Cell Culture. Journal of Visualized Experiments: JoVE, 188.

Chapter 4: Creating highly porous granular hydrogel scaffolds reinforced by electrospun hydrogel fibers for long-term stability

Contributing Authors: Jack Whitewolf, Lindsay Riley, Brooke Brady, Greg Grewal, Tatiana Segura, and Chris Highley

Abstract:

Scaffolds composed of crosslinked hydrogel microparticles (HMPs), or granular hydrogel scaffolds (GHSs), contain pore spaces much greater in size than conventional bulk hydrogels. Packing of HMPs creates interconnected, micron-scaled openings that are preserved upon crosslinking. Scaffolds created by crosslinking packed HMPs, also known as microporous annealed particle (MAP) scaffolds, improve cell migration and proliferation. However, while higher porosity and larger pore sizes have been shown to improve cellular infiltration, creation of high porosity and large pores are usually associated with decreased packing density and number of HMP contacts, resulting in reduced scaffold mechanical integrity. Here, we address this challenge by demonstrating 1) the fabrication of high-porosity granular scaffolds beyond what is possible from particle packing using sacrificial HMPs; and 2) stabilization of the high-porosity scaffolds by incorporating electrospun hydrogel fibers within the scaffolds. We fabricated granular scaffolds using norbornene-modified hyaluronic acid (norHA) HMPs and gelatin HMPs as the sacrificial population. HMPs with varying norHA concentrations and sizes were fabricated to quantify the effect of HMP mechanical property and sizes on granular hydrogel flow behavior. We created HMP scaffolds with up to 50% porosity by incorporating (0-50 vol.%) sacrificial gelatin HMPs. When electrospun norHA fibers were incorporated in scaffolds at 5-10 vol.%, highly porous scaffolds retained their structure

over a period of 28 days. Additionally, HUVECs were mixed with HMPs prior to scaffold formation and exhibited high viability. The HUVEC-HMP mixture could be injected through a needle and then crosslinked to form a scaffold, with post-injection viability >80%. Overall, this study demonstrates the development and characterization of a stable, highly porous granular scaffold system with high processibility and cytocompatibility.

Introduction:

Hydrogels have been widely used as 3D cell culture platforms. Synthetic and natural polymers have been engineered to recapitulate characteristics of the extracellular matrix (ECM), including mechanical properties, degradability, and bioactive ligands that guide cell fate. Among the various strategies of hydrogel engineering, fabricating granular hydrogels from microparticle components has become a popular approach. Hydrogel microparticles (HMPs) can be packed together to create granular hydrogels that can transition from a solid-like state to a liquid-like state[1-3]: when the applied stress is less than the yield stress of granular hydrogel system, the bulk material responds elastically to deformation. However, once applied stress surpasses the yield stress, the HMPs can flow past each other, and the bulk material exhibits shear-thinning behavior. This property is particularly desirable for injection-based applications and 3D printing[4,5]. Moreover, even when fully packed, interconnected, micron-scale porosity exists among the HMPs, priming the system for easy cellular infiltration[6-8]. This porosity is preserved even after interparticle crosslinking between HMPs is established to form a scaffold, as shown extensively with microporous annealed particle scaffolds[6] (or MAP scaffolds). HMPs comprising MAP scaffolds can be injected into wound sites then crosslinked to form a microporous scaffold, which have been shown to support tissue regeneration[6,9-12].

While the micro-scale porosity in packed HMPs is desirable for cellular infiltration, porosity comes at the cost of mechanical integrity[13]. In scaffolds formed by continuous hydrogels, polymer chains crosslink to form nanoscale meshes throughout the hydrogel, creating a highly crosslinked network that holds the scaffold together. In granular hydrogel scaffolds (GHSs), while the HMPs themselves possess the same polymer network, the interactions that hold the scaffold together occur at HMP interfaces, which are comparatively fewer and further apart, as each HMP could be 10s to 100s of µm in size. As a result, HMP stability relies on discrete clusters of interactions occurring at the interfaces of neighboring HMPs. This differs qualitatively from crosslinked polymer chains in continuous hydrogels, where the distribution of crosslinking sites is more homogeneous, and polymer chains can utilize long-range interactions beyond their neighbors to strengthen the network and dissipate applied force. In comparison, the clusters of interactions that uphold GHS structure are fewer in number and more localized, making GHSs more liable to disruption from external forces and hence weaker.

Currently, approaches for increasing the stability of GHSs are limited. Some stabilization approaches include using crosslinked interstitial matrix or interpenetrating networks throughout the GHS[13-16]. However, both methods require a polymer network to be formed within the interstitial space, doing away with the microscale interstitial porosity and focusing on applications that do not require a microporous scaffold. Other potential approaches to increase stability include decreasing HMP sizes and increasing packing density. Both serve to create more HMP interfaces available for interaction. However, as smaller HMPs pack more densely, the interstitial pore sizes also become smaller and less accessible to cells. Increasing packing density faces similar limitations, as both pore sizes and total porosity could be reduced as HMPs become more packed[17-19].

In our work, we explore another approach to increase GHS stability that does not impact HMP packing and scaffold porosity. We demonstrate stabilization of HMP scaffolds by adding small volumes of high-aspect ratio hydrogel fibers as a scaffold-forming component. By adding small volumes of fibers that have widths of single-microns but greater lengths than HMP diameters, HMP associations can be extended beyond its immediate neighbors without significantly affecting total porosity. This allows HMPs to form connections through fibers in a larger surrounding volume, strengthening the network beyond the strength of HMP interfacial bonds. Additionally, fiber stabilization of GHSs allows for the establishment of highly porous scaffold with long-term stability. Using sacrificial HMPs, we can achieve well-controlled porosity by changing the ratio of sacrificial HMPs to scaffold-forming HMPs. We demonstrate that large, interconnected pores desirable for cellular infiltration can be achieved in this manner without requiring low packing density or large HMPs. Finally, we show that packed HMPs can be injected with cells for facile cell culture, as well as potential applications in cell delivery and regenerative medicine.

Results and Discussion:

Fabrication and characterization of norHA HMPs

HMPs were generated from norbornene-modified hyaluronic acid (norHA). Hyaluronic acid (HA) is a naturally derived polysaccharide that is biocompatible, biodegradable, and amenable to chemical modification. The addition of norbornene pendant groups to HA enables reactions of norHA to thiolated molecules: a highly efficient thiol-ene click chemistry that allows for stoichiometric control over the consumption of norbornene groups by limiting the available thiol-containing groups (Figure 1A). This enables the preservation of norbornene pendant groups for secondary conjugations. Here, we synthesized norHA with a 0.3 degree of substitution (DoS), confirmed by ^{1}H NMR (Figure S1). By controlling the thiolated crosslinker to norbornene concentration, 0.3 DoS

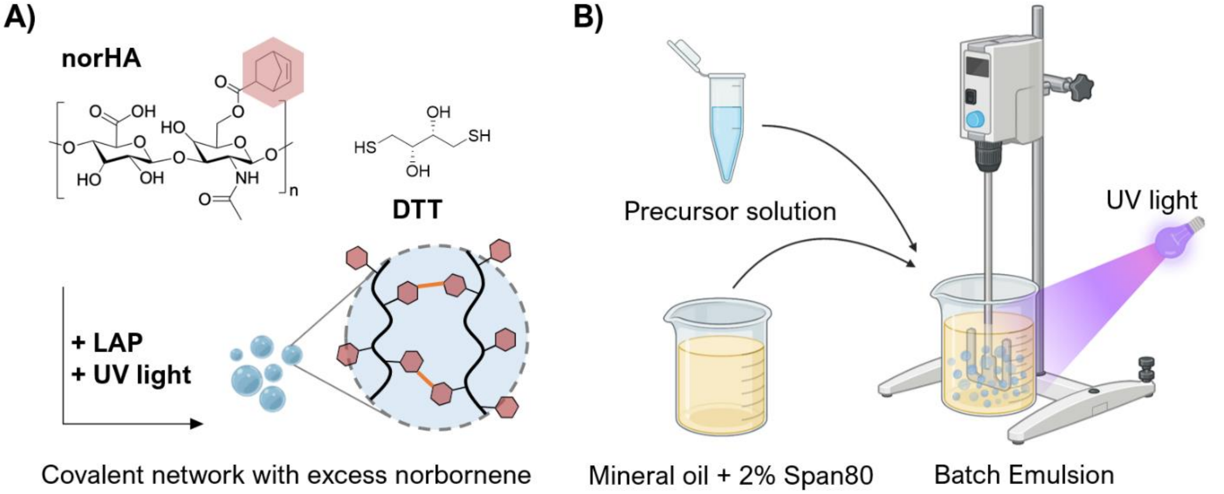

Figure 1. A) Thiol-ene click chemistry using norHA and DTT. Norbornenes conjugated to HA and DTT can be crosslinked under UV light with the presence of a photoinitiator (LAP). Stoichiometric control of DTT ensures there be excess norbornene for later reactions. **B)** HMP fabrication. HMP precursor (norHA, DTT, and LAP; aqueous phase) is mixed together with mineral oil with 2% Span80 (oil phase) and homogenized to form an emulsion. Application of UV light while stirring crosslinks the precursor solution into stable HMPs.

sufficiently supports both crosslinking required to form the HMPs and subsequent interparticle crosslinking to form GHSs (Table S1).

Using batch emulsification, we generated norHA HMPs (Figure 1B) with varying moduli and size by varying the HMP composition and the speed of homogenization, respectively. Soft, medium, and stiff HMPs are made using 2% w/v, 3% w/v, and 4% w/v norHA concentration and 2mM, 3mM, and 4mM DTT concentration, respectively (Table S1). The mechanical properties of the HMPs are characterized by measuring the storage moduli of bulk hydrogels with identical compositions. Soft, medium, and stiff HMPs have average storage moduli of 782 Pa, 1758 Pa, and 3797 Pa, respectively (Figure S2). We can also alter the size of norHA HMPs by changing the spin speed of the homogenizer used for emulsification. Small, medium, and large HMPs were generated at 750 rpm, 1500 rpm, and 3000 rpm. For each modulus, we generated HMPs with mean diameter ranging from

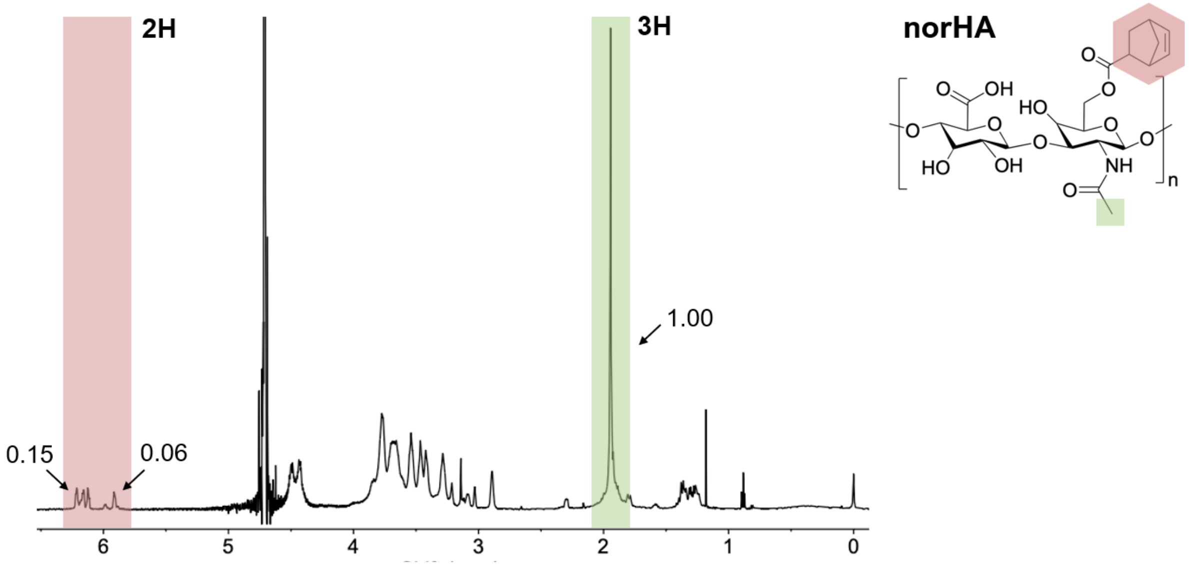

Figure S1. ^{1}H NMR spectrum of norbornene-modified HA with 0.3 degree of substitution.

<10μm to 50μm (Table 1). Due to the nature of the emulsion process, size distributions of HMP populations were polydisperse.

Polydispersity increased as the stir speed decreased (Figure 2A); however, mean sizes were well-separated and statistically significant for groups across stir speeds. Effect sizes were also calculated for each comparison. The smallest effect size calculated for comparing between stir speed was 1.17, accounting for a large effect (>0.8). In comparing the HMP size distribution across HMP composition; however, the largest effect size

Table 1. NorHA HMP mean sizes for all compositions and speeds

	Mean diameter (μm)		
HMP composition	***750 rpm***	***1500 rpm***	***3000 rpm***
2 wt% norHA	46±23.5	23.2±9.53	8.65±5.24
3 wt% norHA	52.7±27	29.5±11.6	9.33±5.24
4 wt% norHA	49.7±30.9	26.6±14	6.49±5.02

Table S1. Varying norHA HMP compositions and available reactive groups

	Soft	Medium	Stiff
norHA (wt%)	2	3	4
DTT (mM)	2	3	4
Total norbornene (mM)	15	22.5	30
Remaining norbornene (mM)	11	16.5	22
% norbornene consumed	26.7	26.7	26.7
		norHA DoS:	0.3

calculated was 0.55, accounting for a medium effect (>0.5), with most groups having a small effect (>0.2) and less (Figure 2B).

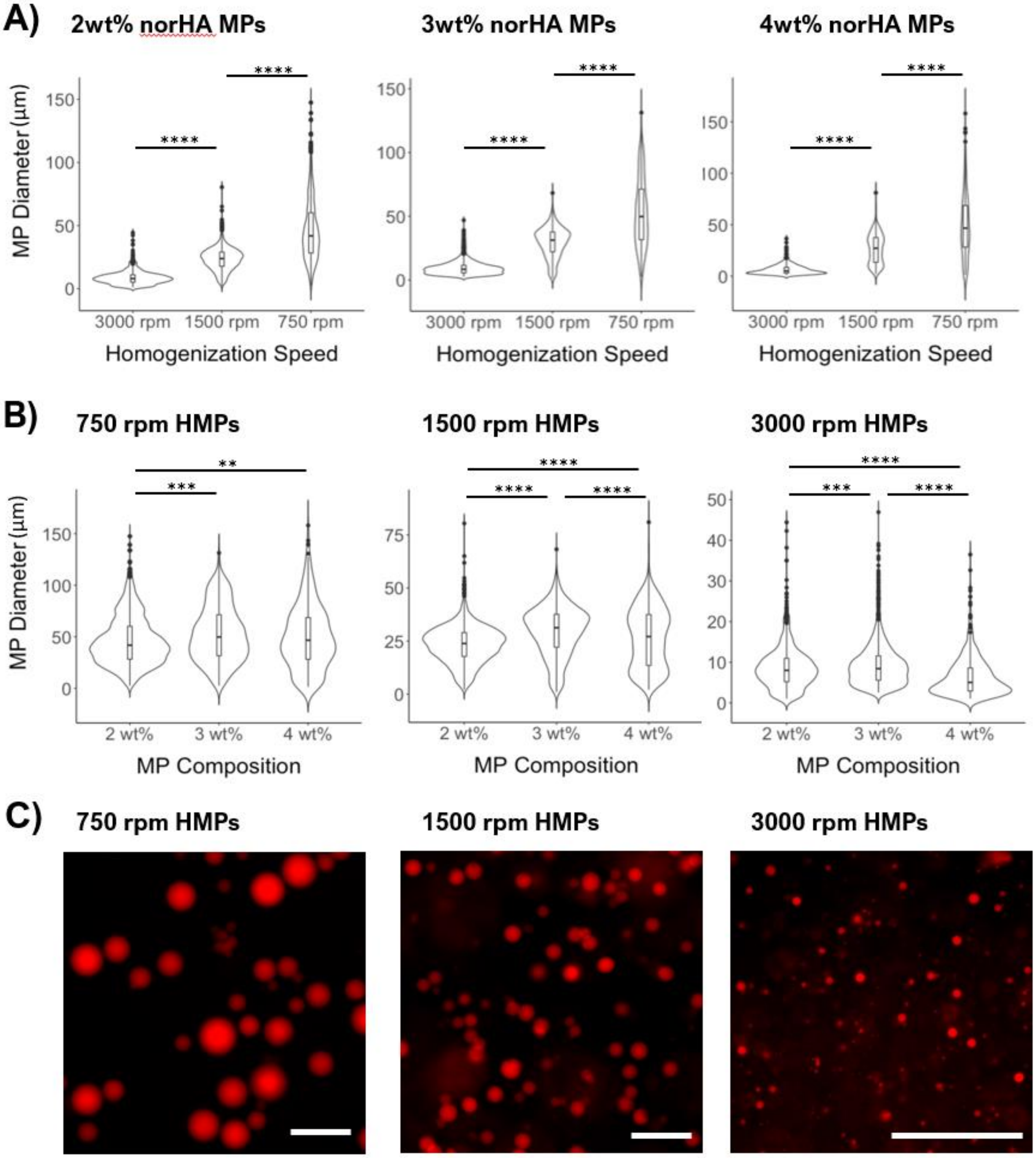

Figure 2. NorHA HMP size characterization. **A)** Size distributions comparing HMPs made from varying homogenization spin speeds. **B)** Size distributions comparing HMPs with varying compositions. C) Fluorescent micrograph of HMPs at varying spin speeds. Scale bars = 100 µm.

Next, we conducted rheological tests to investigate the properties of granular hydrogels formed from packed HMPs in response to applied strains, in the absence of interparticle crosslinking. HMPs, when sufficiently packed, enter a “jammed” state[1-3]. Jammed HMPs have been well documented to be able to flow under external forces and recover when applied force is removed. This property allows granular hydrogel formulations to be extruded from a needle and enabled various applications in injectable therapeutics and 3D printing. We confirmed our HMPs exhibit the same behavior using time sweeps alternating between 0.5% and 500% strain (Figure S2). For all compositions and sizes, packed norHA HMPs exhibited solid-like behavior below the yield strain (here, at 0.5% strain) and liquid-like behavior above the yield strain (here, at 500% strain). Frequency and strain sweeps were also conducted for all HMPs. We observed that changes in granular hydrogel moduli correlated to changes in the moduli of the component HMPs. In considering the sizes of the HMPs, when size was held constant, increases in HMP modulus resulted in increases in the modulus of the granular hydrogel as a bulk (Figure 3A, S2). However, changes in HMP sizes largely did not affect the bulk modulus, with one exception observed in the 4% norHA group (Figure 3A).

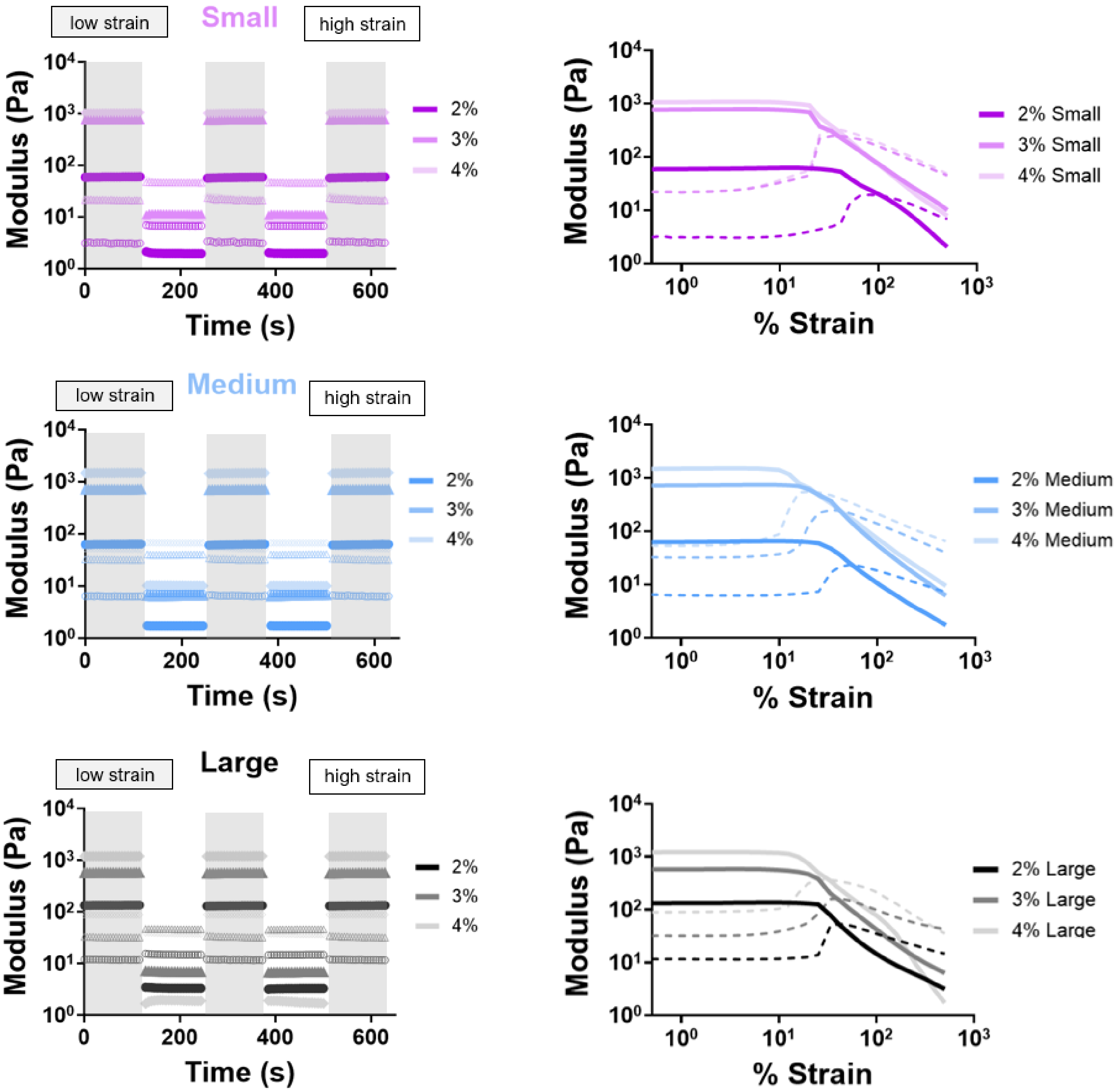

Figure S2. Representative rheology results for all norHA HMP compositions and sizes. *Left column:* time sweeps with strains alternating from high (500%) strain to low (1%) strain. *Right column:* strain sweeps from 0.1% strain to 500% strain. From top to bottom: rheology results of small, medium, and large norHA HMPs, respectively.

Another important feature of granular hydrogels is their resistance to flow, often described by the yield stress of the system. Here, we measured yield stress using stress sweeps supplemented by shear rate sweeps focused on lower shear rates (Figure S3, Figure 3B). Yield stress of each formulation was quantified using results obtained from stress sweeps; shear rate sweeps at low shear rates provided an indirect measure of shear stresses that can used to confirm measurements from stress sweeps by showing values obtained in each test do not significantly deviate from each other. Similar to results obtained for bulk moduli, for HMPs of the same size, yield stresses of packed HMPs increased as the moduli for component HMPs increased (Figure 3B). We also observed that for 3% norHA and 4% norHA HMPs, yield stress increased as HMPs became smaller (Figure 3B). This finding largely corroborates literature findings of yield strain changes with respect to HMP sizes[7]. Yield stress is difficult to define and measure for many material systems[20]. Our shear rate sweep profiles on packed HMPs were reminiscent of shear-banding behavior in other packed systems, suggesting that shear-banding within packed HMPs could be a driving force in the initiation of HMP flow[20-22]. A possible reason for the yield stress changes we saw could be due to larger HMPs possessing less contact density per unit volume compared to smaller HMPs. The lessened contacts may be less suited for dissipating the externally applied force to other HMPs, causing localized disruptions as external forces exceed local HMP interactions, thus facilitating the onset of shear bands or flow.

Further, this trend was corroborated by qualitative experimental observations. 2wt% norHA HMPs, even when fully packed, flow very easily and could not hold their shape at rest, reflecting the low yield stress as well as storage modulus. On the other hand, small

3wt% norHA HMPs and all 4wt% HMPs presented challenges in processing: during pipette transfer, these HMP formulations frequently became stuck to the side of the pipette tip, and the bulk granular material fragmented or separated into discrete pieces during aspiration or extrusion.

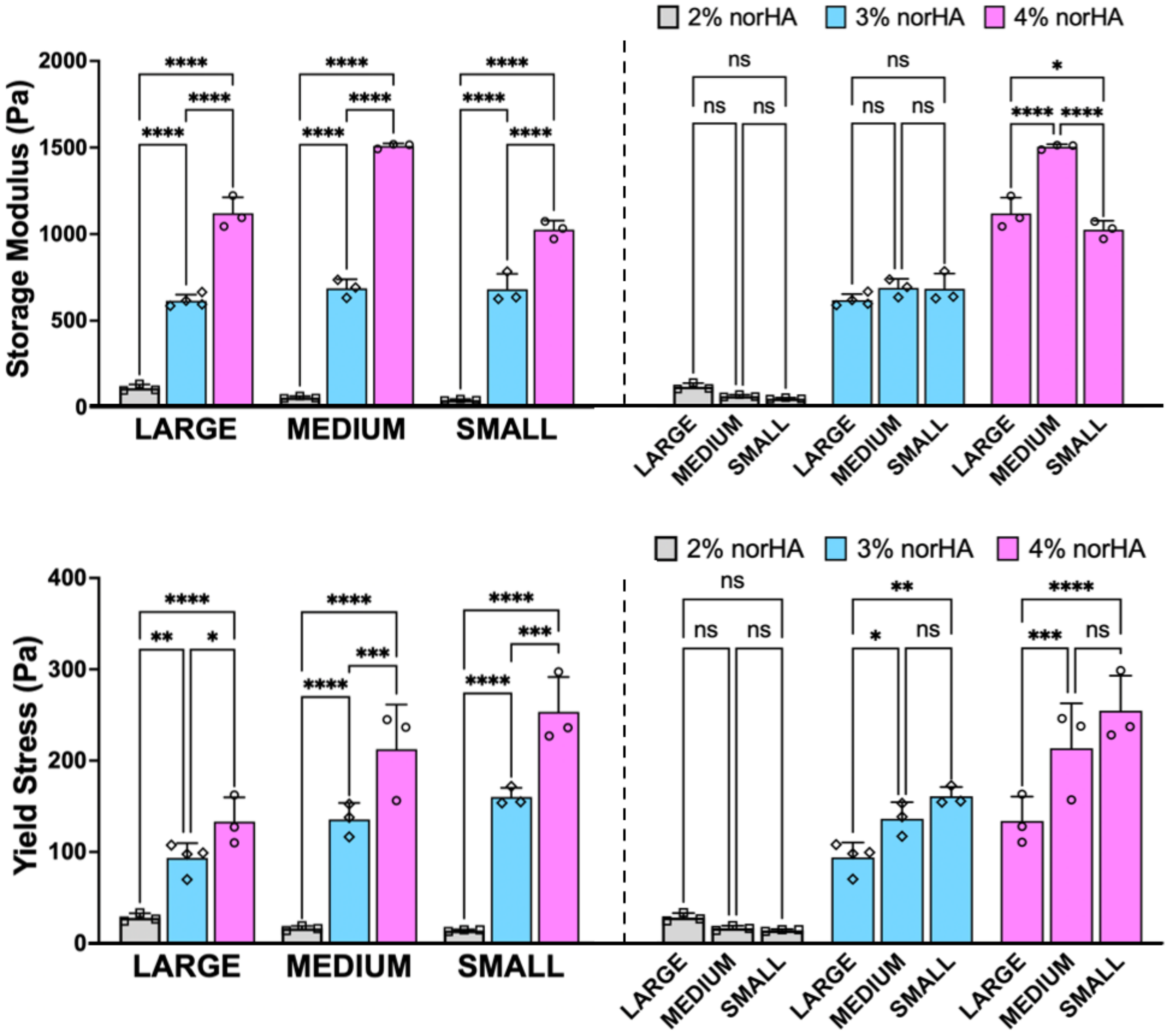

Figure 3. **A)** Quantified storage modulus of norHA HMPs for all compositions and sizes, compared based on composition (left) or size (right). **B)** Quantified yield of norHA HMPs for all compositions and sizes, compared based on composition (left) or size (right).

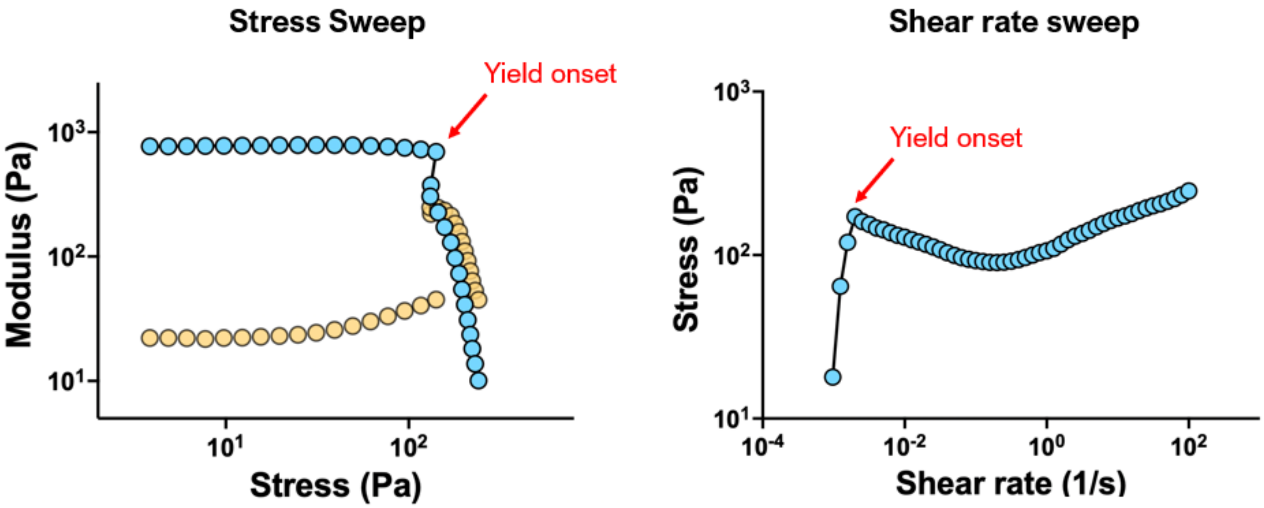

Figure S3. Representative rheology curves for packed norHA HMP stress sweep (left) and shear rate sweep (right). Red arrow points to representative data points used for quantifying and confirming yield stress.

Creating tunable porosity in HMP scaffolds using sacrificial gelatin MPs

Porosity as well as pore sizes in hydrogel scaffolds influence important processes such as cellular infiltration, immune cell responses, and vasculature growth. In HMP scaffolds, spaces among packed spherical particles inherently create interconnected micropores that are challenging to engineer in bulk hydrogels, facilitating cellular infiltration and tissue regeneration when implanted *in vivo*. Currently, porosity in HMP scaffolds is largely controlled by changing HMP sizes and packing density; however, limitations exist for both. Pore sizes can be increased by increasing HMP diameters without affecting porosity. However, increasing HMP sizes can impact packing behavior and affect bulk modulus undesirably[7,23,24]. The uniform increase in pore size can also cause cells to fall through the open spaces, presenting challenges for in vitro culture[24,25]. On the other hand, decreasing packing density can increase porosity[18]. However, as the interstitial fluid volume increases, the tendency of HMPs to stay solid-like at rest may be attenuated. More importantly, cross-linking becomes impossible as interstitial space becomes greater and the HMPs lose physical contact with each other, limiting the porosity.

The use of sacrificial HMPs is an alternative method for creating porosity that does not rely on changing particle sizes or packing density. Here, we mixed known volumes of norHA HMPs (scaffold-forming) and gelatin HMPs (sacrificial) at defined ratios to control porosity in HMP scaffolds. Gelatin HMPs were fabricated similarly to norHA HMPs through emulsification (Figure S4) and mixed with norHA HMPs to form solid scaffolds. The component gelatin HMPs can be liquefied (or sacrificed) at 37°C, making them easy to remove and create pore spaces under standard culture conditions. The process is as shown in Figure 4A. First, to observe porosity characteristics, we fabricated gelatin HMPs with varying sizes and generated scaffolds where norHA HMP diameters are less than, equal to, or greater than gelatin HMP diameters (Figure S5). Scaffolds with norHA HMPs and gelatin HMPs mixed at 100:0, 75:25, and 50:50 volume ratios were generated for porosity measurement.

We observed large pockets of void space when gelatin HMP diameters are greater than norHA HMP diameters, while equal-sized or smaller gelatin HMPs created more continuous void spaces in scaffolds (Figure S5). Gelatin HMP sizes had negligible effects on the total porosity created. For subsequent studies, all scaffold porosities are created using gelatin HMPs with diameters smaller than norHA HMP diameters.

For each volume ratio group, we generated separate scaffolds using small, medium, and large populations of norHA HMPs to elucidate the effect of size on porosity. We found that for all norHA HMP sizes, we consistently generated scaffolds with ~10% porosity for 100% norHA scaffolds; ~30% porosity for 75% norHA scaffolds; and ~50% porosity for 50% norHA scaffolds (Figure 4B). However, for each volume ratio group, no statistically significant differences were found for porosity among norHA HMPs with different sizes (Figure 4B).

We did, however, see a trend of Increasing porosity as HMP sizes increased for 100% norHA scaffolds, which corroborates reported findings in existing approaches that do not use sacrificial HMP components[7]. Interestingly among the small norHA HMPs (3000 rpm)

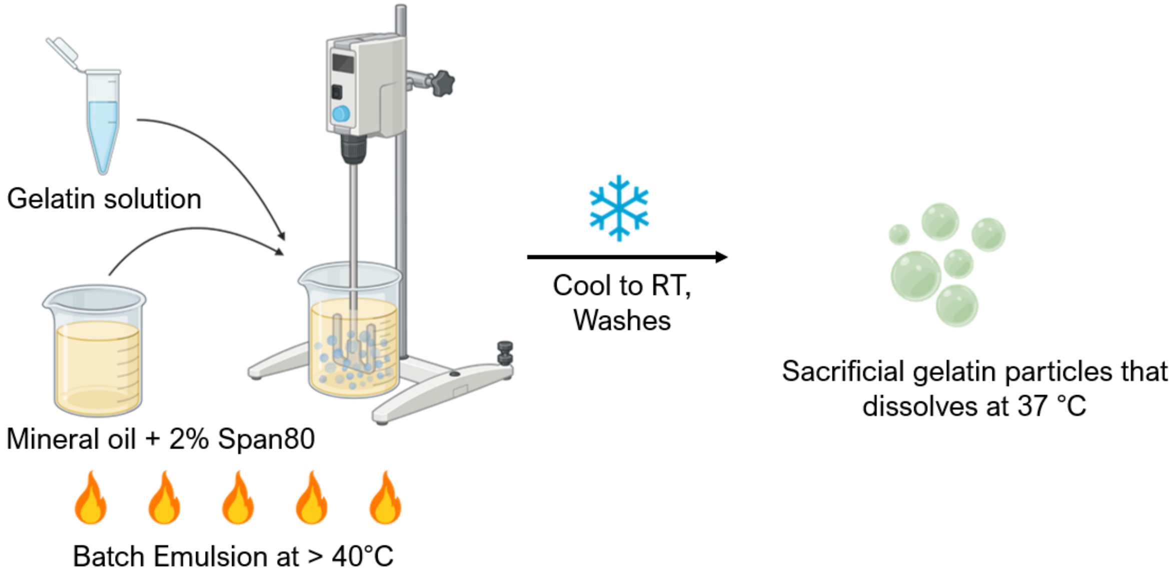

Figure S4. Gelatin HMP fabrication scheme. Gelatin solution was homogenized at varying speeds in oil and surfactant at 40 degrees Celsius. The mixture is then cooled to room temperature and washed in the same method as norHA HMPs to obtain gelatin HMPs.

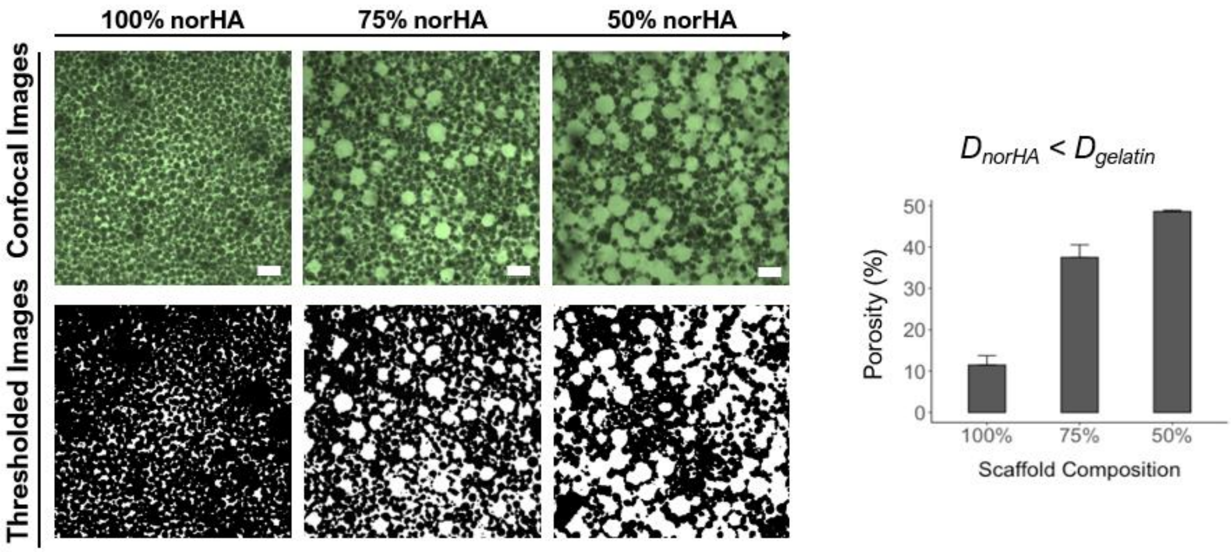
100% norHA
75% norHA
50% norHA
Confocal Images
Thresholded Images
$D_{norHA} < D_{gelatin}$
Porosity (%)
50
40
30
20
10
0
100%
75%
50%
Scaffold Composition

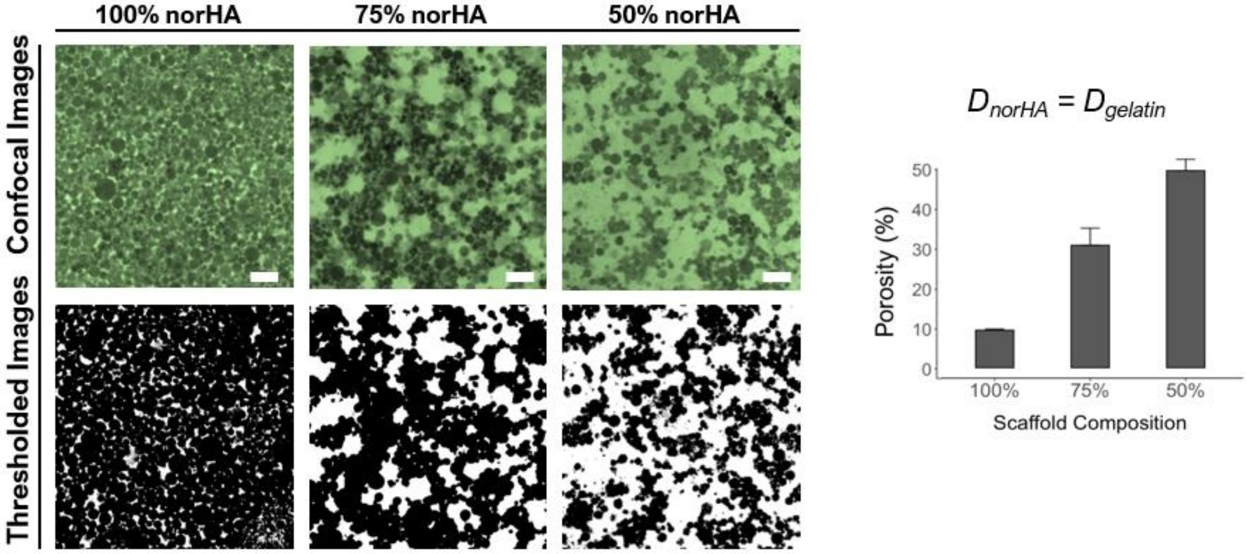
100% norHA
75% norHA
50% norHA
Confocal Images
Thresholded Images
$D_{norHA} = D_{gelatin}$
Porosity (%)
50
40
30
20
10
0
100%
75%
50%
Scaffold Composition

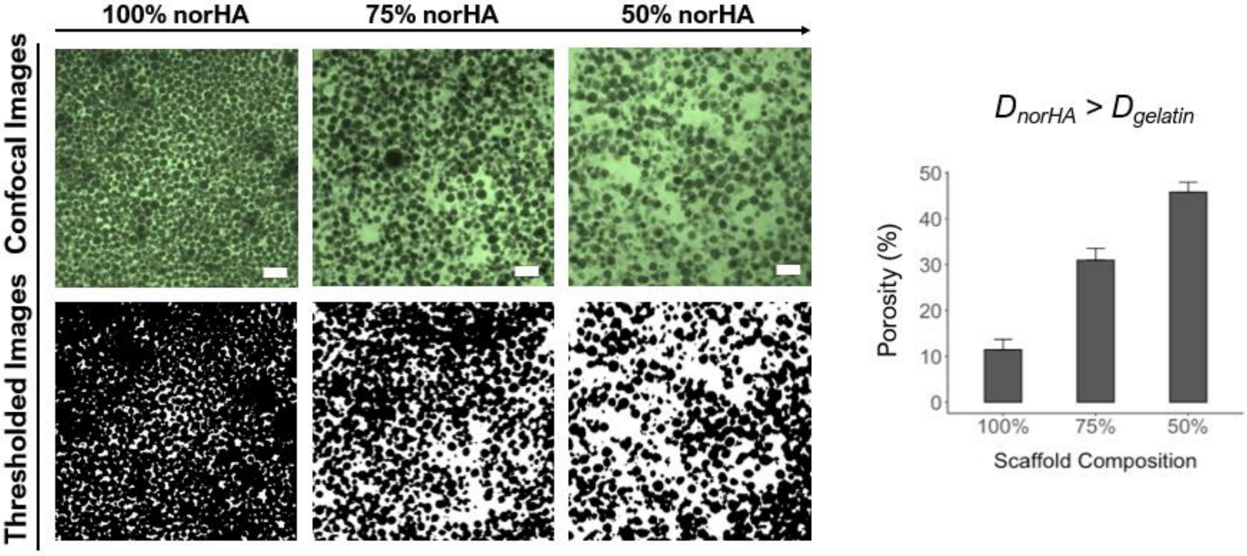
100% norHA
75% norHA
50% norHA
Confocal Images
Thresholded Images
$D_{norHA} > D_{gelatin}$
Porosity (%)
50
40
30
20
10
0
100%
75%
50%
Scaffold Composition

Figure S5. From to top to bottom: 100% norHA, 75% norHA, and 50% norHA scaffolds created with gelatin HMPs with diameters greater than (top), equal to (middle), or less than (bottom) the diameters of norHA HMPs. Porosity of each scaffold is quantified and shown on the right.

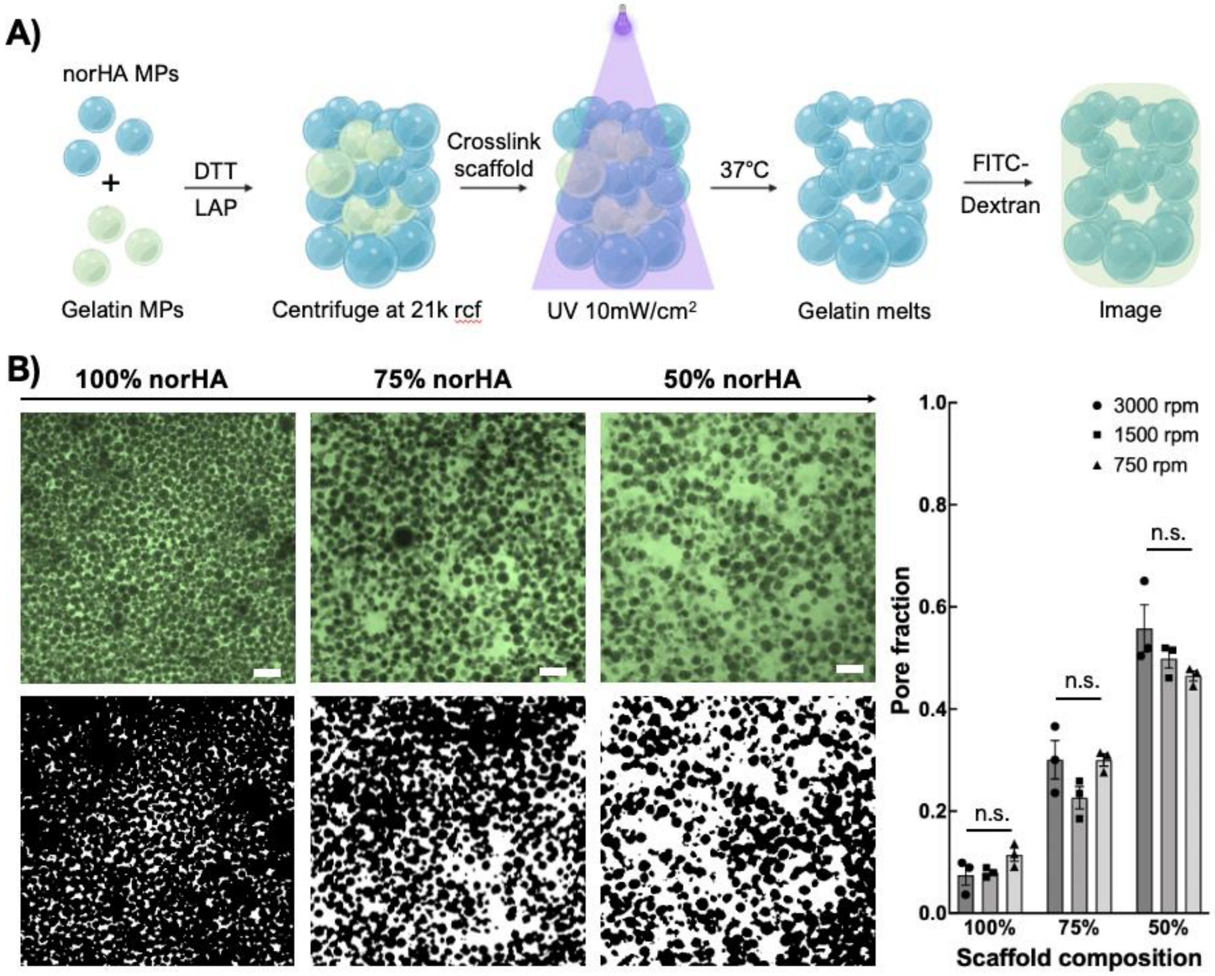

Figure 4. A) HMP scaffold fabrication. Desired ratios of norHA and gelatin HMPs, along with DTT and LAP, are combined and packed by centrifugation. The packed HMPs were then crosslinked and cultured at 37°C to liquefy gelatin HMPs. The scaffolds were then submerged in FITC-dextran solution and imaged. **B)** *Left:* Representative confocal images (top) and corresponding thresholded images (bottom) of scaffolds with varying ratios of norHA HMP (750 rpm) to gelatin HMP (2000 rpm). *Right:* Quantified void volume fraction for each scaffold composition. Scale bars = 100μm.

in 100% norHA scaffolds, we often saw pockets of pore spaces much larger than the HMPs (Figure S6), whereas pore spaces only existed between packed particles for larger norHA HMPs. This suggests that the centrifugal force was not enough to overcome the microstructures created by small HMPs and may be remedied by more aggressive filtration methods to eliminate interstitial fluid. The inherent structure may be desirable for certain applications and has implications on the flow properties of packed HMPs, as they could create local heterogeneity in shear-driven flow that disrupts bulk flow behavior. However, this is outside the scope of the current work.

We then quantified the 2-D pore sizes using a custom Matlab program. Images were segmented and processed to quantify the area of interconnected pores for all our scaffolds compositions. Plotting pore area distribution based on the number frequency revealed that small pores formed by HMP packing made up the majority number-wise (Figure S7). However, large pores that were fewer in number but account for high fractions of total pore area with several magnitudes higher pore area were seen in 75% and 50% scaffolds (Figure S7). Toward better capturing and elucidating the effect of these large

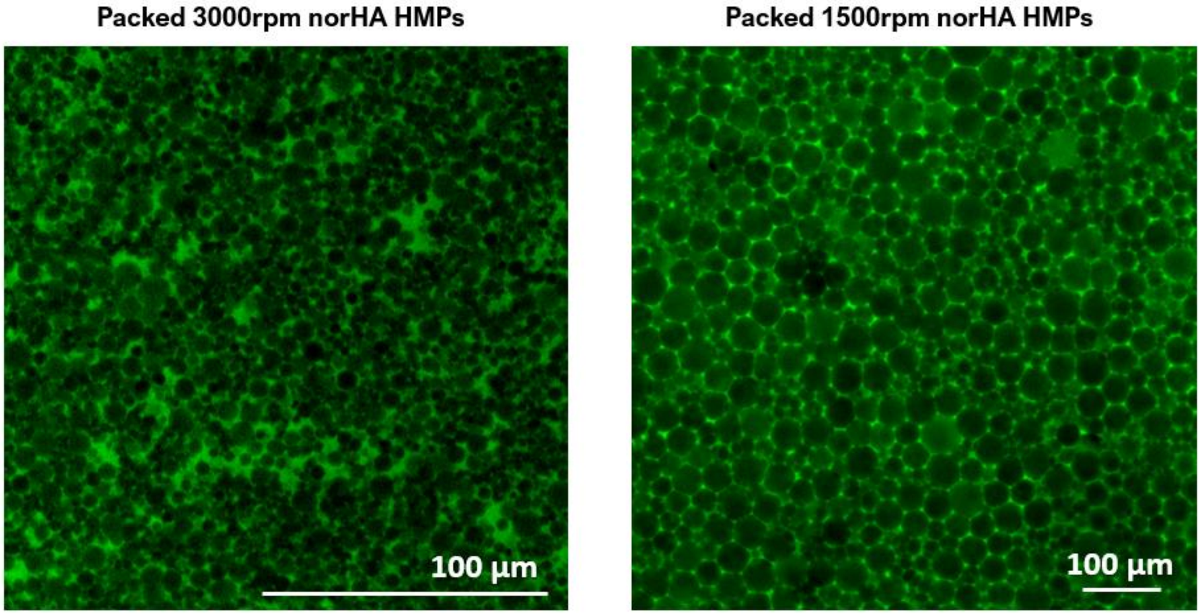

Figure S6. *Left:* small norHA HMPs packed at 21,000 rcf and imaged in FITC-dextran. *Right:* medium norHA HMPs packed at 21,000 rcf and imaged in FITC-dextran (green).

pores, we calculated the pore area fractions (pore areas divided by total pore area) and plotted the pore size distribution based on the area fraction with which the pore sizes were associated. A visual representation of pore distribution is shown in Figure 5A, where large, connected pores form the majority of the total pore area but are few in number; and smaller pores, though numerous, only comprise a small amount of pore area. This is corroborated by area fraction-based distribution (Figure 5B). We saw that regardless of HMP sizes in the scaffold, higher total porosity created by sacrificial materials resulted in having larger pores that contribute to most of the porosity. This effect is most pronounced in our large norHA HMPs, where one or a few pores contributed to ~90% of the total porosity in the 50% scaffolds and ~60% of total porosity in the 75% scaffolds, indicating very high degrees of interconnectivity.

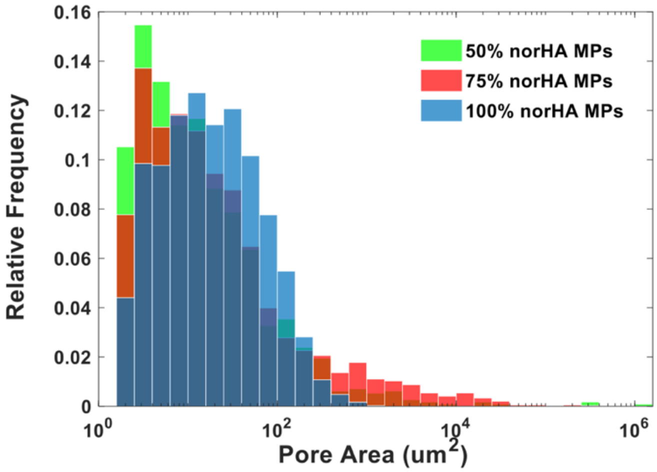

Figure S7. Number-based pore area distribution for each scaffold composition.

Further, we observed that in HMP scaffolds with varying porosities, pore size distributions among the small pores were similar. We hypothesized that these pores existed among packed norHA HMPs and are preserved when sacrificial HMPs are incorporated. In other words, in 100% norHA scaffolds, these pore features would exist throughout scaffolds;

however, in 75% and 50% norHA scaffolds, these features exist where packed norHA HMPs were not disrupted by gelatin HMP incorporation. To investigate this, we looked at the distribution of only the smaller pores spaces in each group. More specifically, for each norHA HMP size, we used the largest pore found in the 100% norHA group as the cut-off pore size. Pore spaces in 75% norHA and 50% norHA with area larger than the cut-off were eliminated, and the pore size distribution was compared among the groups (Figure S8). The pore size distribution based on number fraction as well as area fraction showed great consistency among groups with different porosity, suggesting that while higher porosity groups possess much larger pore spaces, the smaller pore spaces that resulted from HMP packing are still present.

The heterogeneity in pore sizes is unique to this system, where interconnected “mega” pores comprise most of the porosity, yet pores areas several magnitudes lower are present. The co-existence of both types of pores allowed for the creation of non-uniform, multiscale void spaces that could encourage cellular infiltration[26-30].

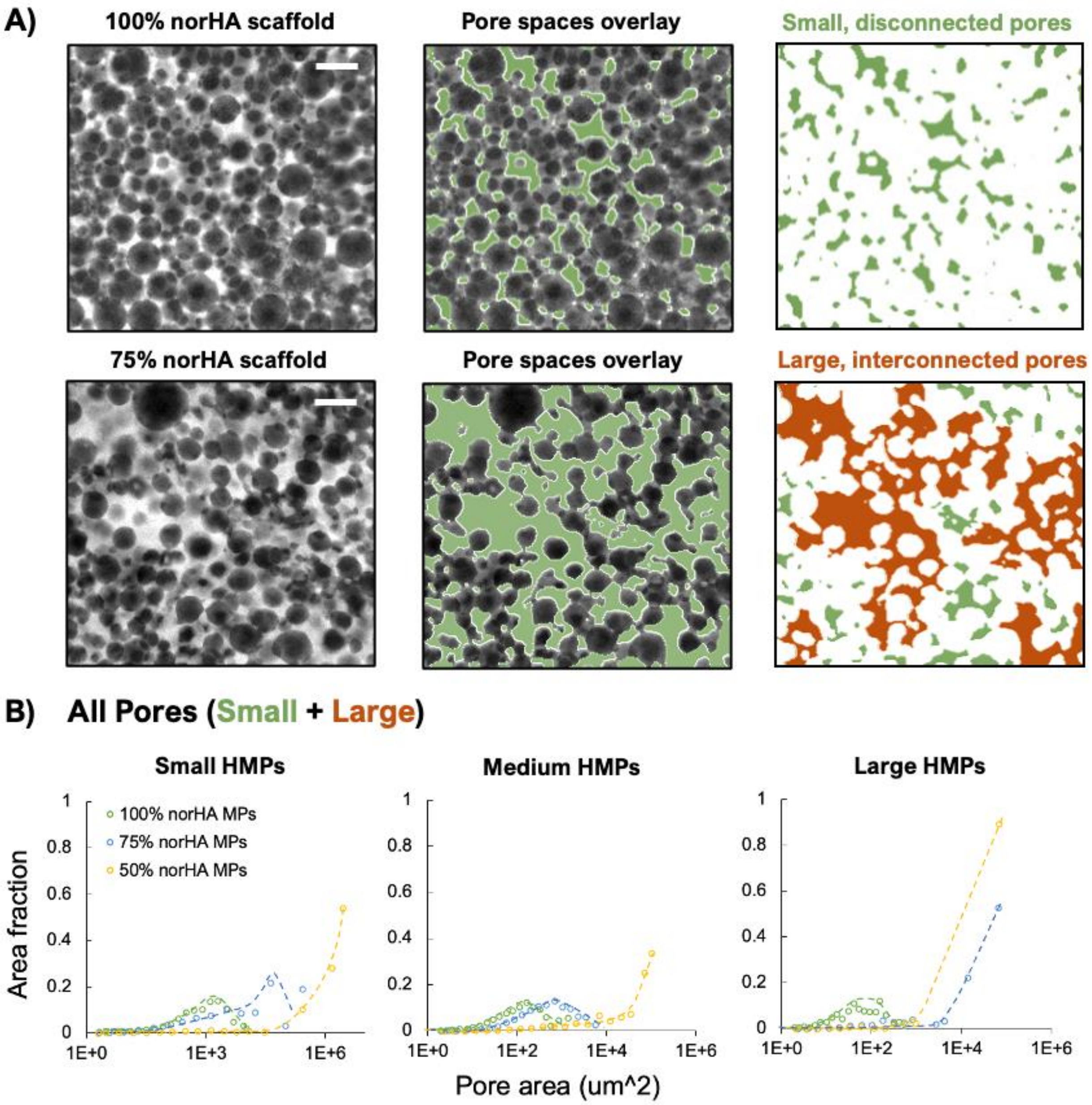

Figure 5. A) Visualization of 2D pore spaces. From left to right: confocal image of the scaffold with fluorescent interstitial space; all pore spaces highlighted in green; and representation of both small pore areas (green) and large pores areas (maroon). **B)** Pore area distribution based on the area fraction of pores, small, medium, and large HMP were used to make 100%, 75%, and 50% norHA scaffolds, the pore areas of each scaffold was found and plotted.

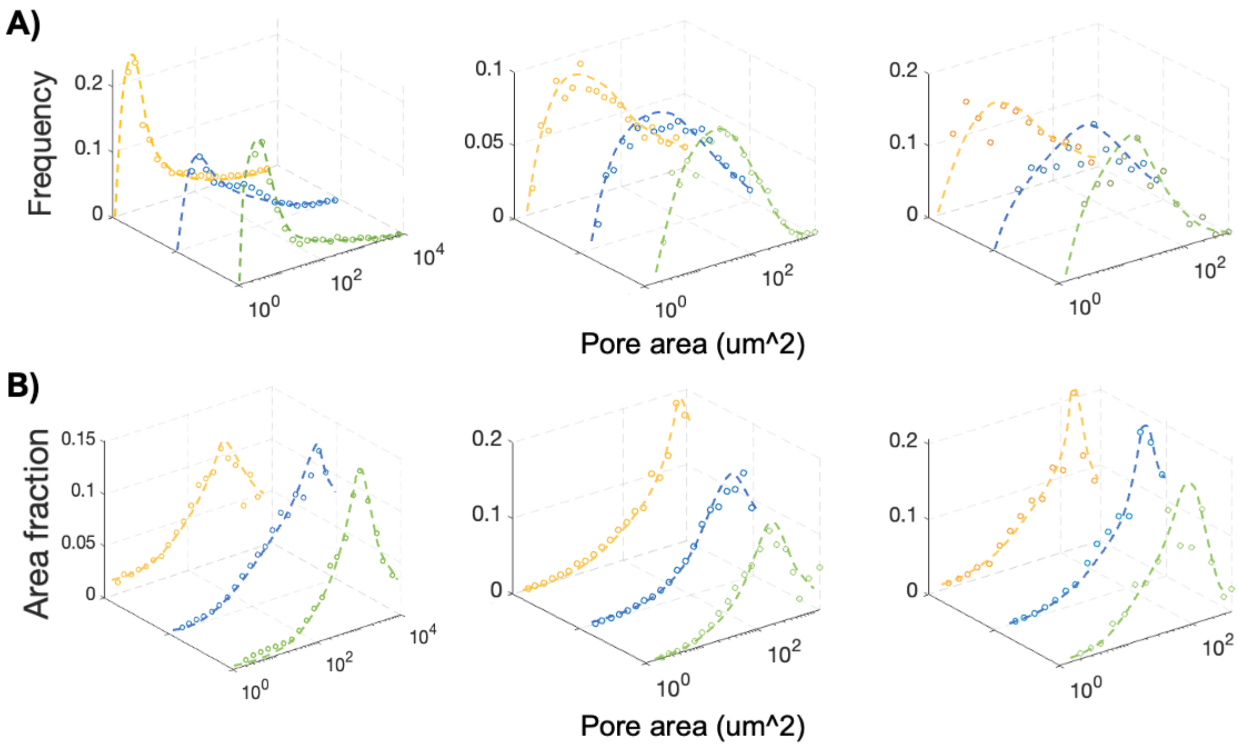

Figure S8. Pore area distributions using the largest pore in 100% norHA scaffolds as the cut-off point. **A)** Pore area distribution based on the number of pores. **B)** Pore area distributions based on the area fraction of pores

Computational assessment of 3D pore spaces in HMP scaffolds

To extend 2D analysis of pore area distribution and general porosity to 3D considerations of pore volumes and interconnectivity, we utilized LOVAMAP[31]. LOVAMAP is a software created specifically for the analysis of 3D pore spaces in GHSs with the ability to accurately discern discrete pore volumes and interconnected pore spaces. Here, our analysis used scaffolds composed of 3% norHA HMPs fabricated at 750 rpm, as this formulation exhibited desirable flow properties and showed the highest connectivity as porosity increased in our 2D analysis.

Using this formulation, we fabricated scaffolds with increasing porosity, as previously described: 100% norHA, 75% norHA, and 50% norHA HMPs with the remainder being sacrificial gelatin HMPs. We fluorescently tagged norHA HMPs for confocal imaging and analyzed confocal z-stacks in LOVAMAP, which computationally reconstructed 3D volumes[25,31] and provided visual representations of computationally identified 3D pore spaces (Figure 6A). For the 100%, 75%, and 50% norHA groups, the total porosities found were 7%, 18.8%, and 59.4%, respectively (Figure 6B). While this deviates somewhat from our 2D analysis, it demonstrates the range of porosity achievable using sacrificial HMPs. If certain porosity is desired, this can be reached by adding or removing sacrificial HMPs and does not affect the trends found in this study. Additionally, 3D analysis allowed us to elucidate the true number of pores in the scaffolds. Analysis of pore number in fixed scaffold volumes showed decreasing number of pores as porosity increases (Figure 6B), indicating much larger pores in higher porosity scaffolds. Average pore size calculated based on porosity (total porosity divided by total number of pores) showed that pore volume increases in magnitudes as porosity increased (Figure 6B).

Plotting volume fraction-based pore volume fraction showed the same trend as in 2D (Figure 6C), especially in our 50% scaffold, where a singular large pore accounted for over 90% of the total porosity. Plotting small pores only using the largest 100% norHA scaffold pore as the cut-off again showed similar distributions (Figure S9), as seen in 2D. This confirms the heterogeneity of the true pore volumes in 3D, where large volumes of pore spaces are interconnected yet small pores created by packing still exist.

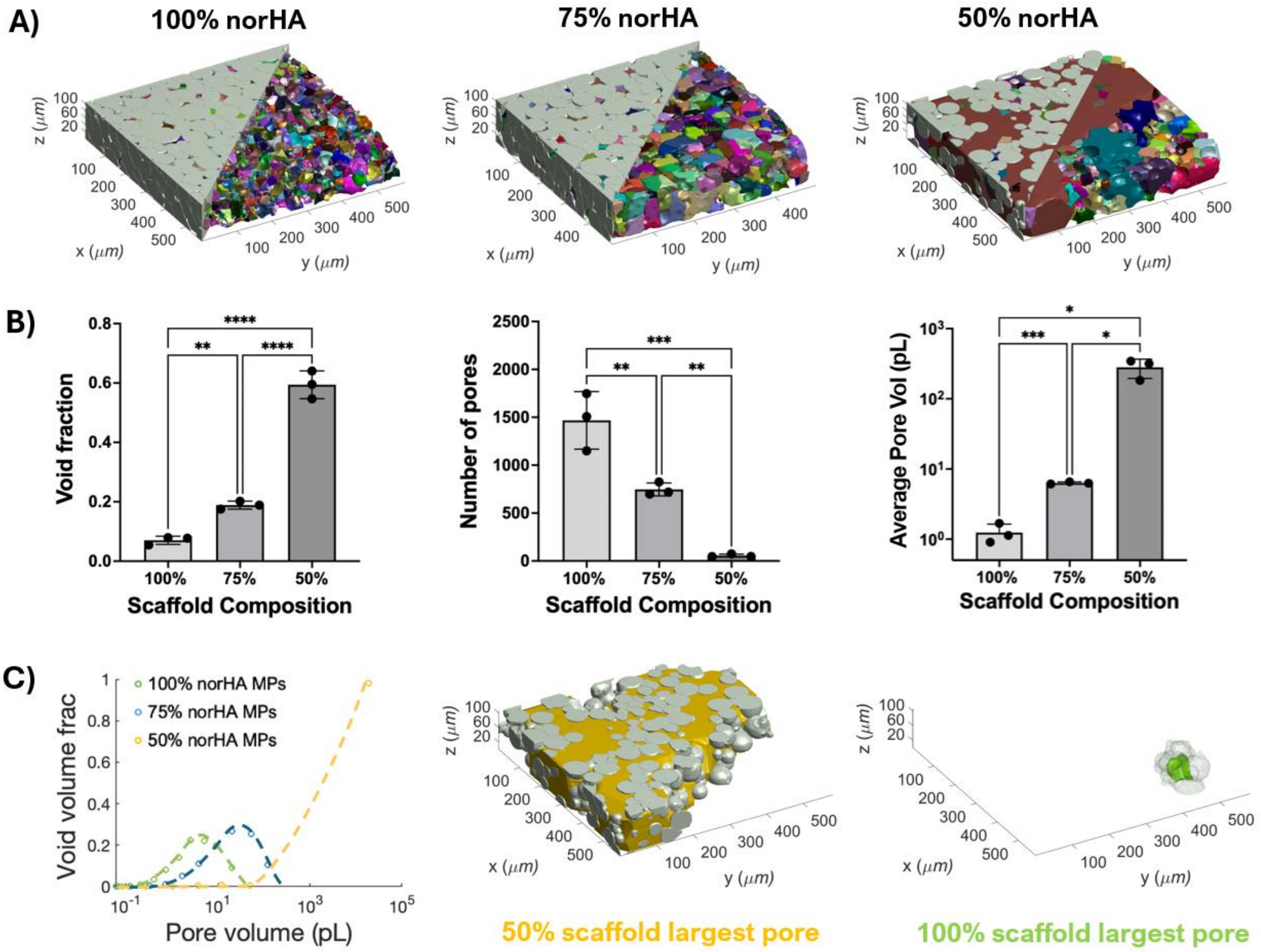

Figure 6. A) Representative LOVAMAP-generated domains of HMP scaffold with varying compositions. **B)** from left to right: void fraction, total number of pores per scaffold, and the average pore volume for each scaffold composition. **C)** *Left:* volume fraction-based pore volume distribution for each scaffold composition. *Middle and right:* representative largest pore for 50% norHA scaffold and 100% norHA scaffold.

Additionally, in reconstructions of scaffold volumes, LOVAMAP analysis allowed us to differentiate between pores which interface with the surface of the scaffold ("exterior pores"), and those that do not and are instead enclosed within HMPs ("interior pores") (Figure S9). This is important towards understanding reciprocal access between the scaffold interior and the surrounding environment through scaffold porosity; for example, exterior pores are desirable for supporting tissue infiltration into the scaffold. We observed that as total porosity increased, larger pore spaces accounted for increasingly large percentages of the total porosity, while the number of interior pores decreased (Figure S9). By volume fraction distribution, we saw that interior pores of all groups were similar in size and distribution, but only ~1% of pore volumes were in interior pores for our highest porosity 50% norHA scaffolds compared to ~50% pore volumes being interior pores for our least porous 100% norHA scaffolds (Figure S9).

Both 2D and 3D analysis demonstrate the co-existence of large, interconnected pores and small pores in our system. This structure is permissible to engineering multi-scale tissue structures (e.g., vasculature) and may be desirable for many tissue engineering and regenerative applications. Importantly, porosities in the scaffolds above are achieved predictably, as a direct function of sacrificial HMP fraction. This circumvents the need to dilute packed HMPs or perform other processing steps to reduce packing density. Instead, mixtures can be ratiometrically combined to achieve controlled, high porosity in a single-step process. With this high porosity, however, maintaining GHS stability remains a challenge. To address this, we looked to quantify the impact of including hydrogel nanofibers within HMPs scaffolds on scaffold stability.

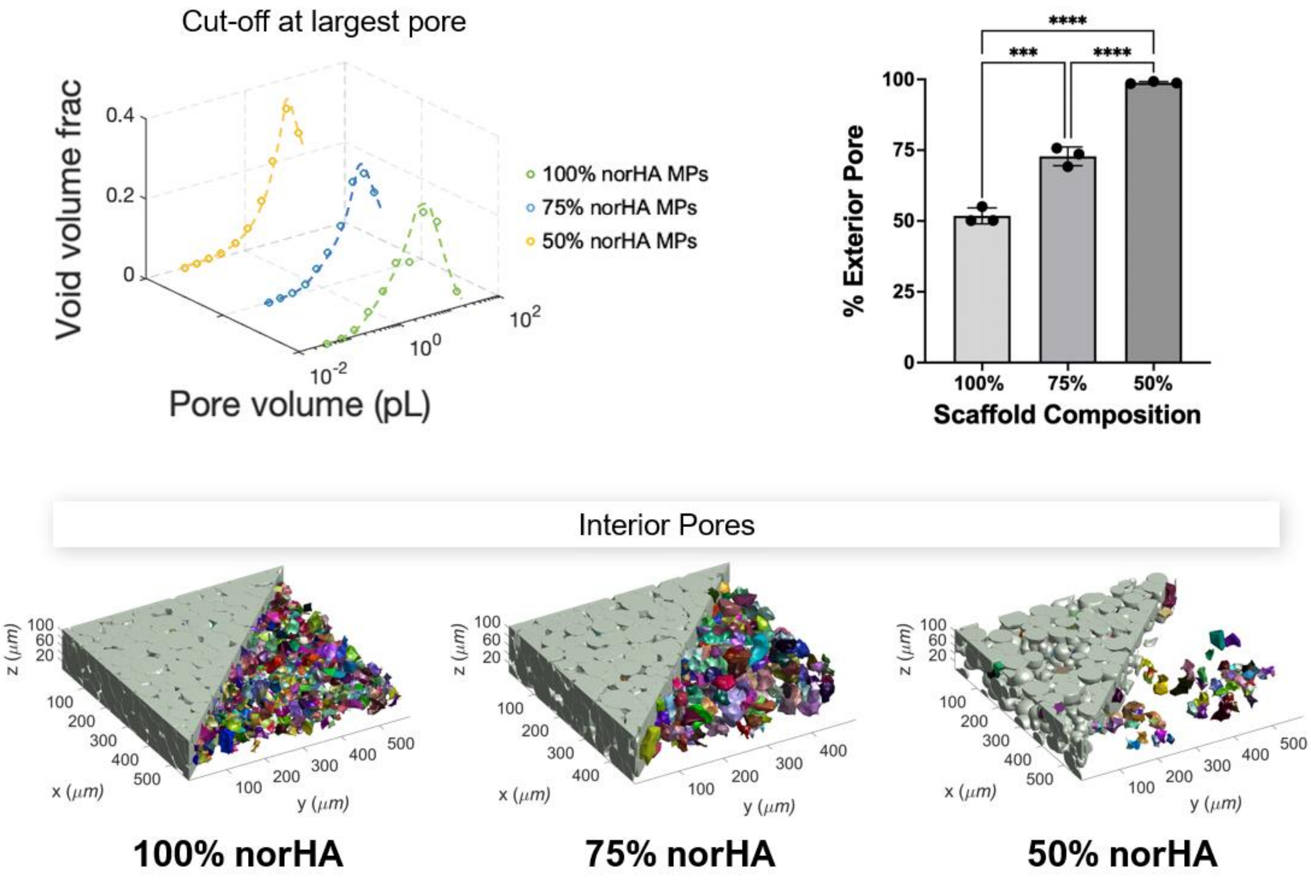

Figure S9. *Top left:* volume fraction-based pore volume distributions using the largest pore in 100% norHA scaffolds as the cut-off point. *Top right:* percent of exterior pores for each scaffold composition. *Bottom:* representative LOVAMAP-generated scaffolds with only interior pores shown.

Incorporation of electrospun fibers alleviates HMP scaffold degradation

To generate hydrogel fibers to reinforce HMP scaffolds, we electrospun norHA fibers crosslinked by norbornene-DTT click chemistry. Crosslinked fibers were hydrated in PBS and segmented (Figure 7A) to yield high-aspect ratio fibers with a mean width of 1.6 ± 0.59 µm and a mean length of 95 ± 48.5 µm. Similar to HMP formation, in crosslinking electrospun norHA fibers, we controlled the norbornene to DTT ratio so that excess norbornene were present after crosslinking. The unreacted norbornenes on fibers enable secondary crosslinking with the norbornenes on HMP surfaces, strengthening fiber-HMP interactions.

We combined defined ratios of norHA fibers, norHA HMPs, and gelatin HMPs, to generate composite scaffolds with controlled compositions (Figure 7B). Confocal imaging of HMP scaffolds with fiber incorporation showed that fluorescently labeled fibers distributed within the interstitial space of the scaffolds (Figure 7C, left and middle), wrapping around volumes occupied by HMPs (spherical-shaped empty spaces), and we observed that fibers did not appear inside spaces occupied by HMPs. Additionally, fibers were well distributed throughout the space and could bridge between HMPs that were otherwise not in direct contact with one another (Figure 7C, right).

Next, we investigated the effects of fiber-based reinforcement on scaffold degradation, as a function of scaffold porosity. In our granular system, we had previously observed degradation by scaffold erosion with increasing porosity and concomitant drops in particle-particle contacts. Here, we added fibers to scaffolds of increasing porosity: 100% norHA HMPs, 75% norHA HMPs, and 50% norHA HMPs, and tracked their weight and appearance over 28 days. For each scaffold composition, we varied the fiber content (0% v/v, 1% v/v, 5% v/v, and 10% v/v) to elucidate the amount of fibers needed to reinforce granular hydrogels in long-term culture. As shown in Figure 8A, 100% norHA scaffolds

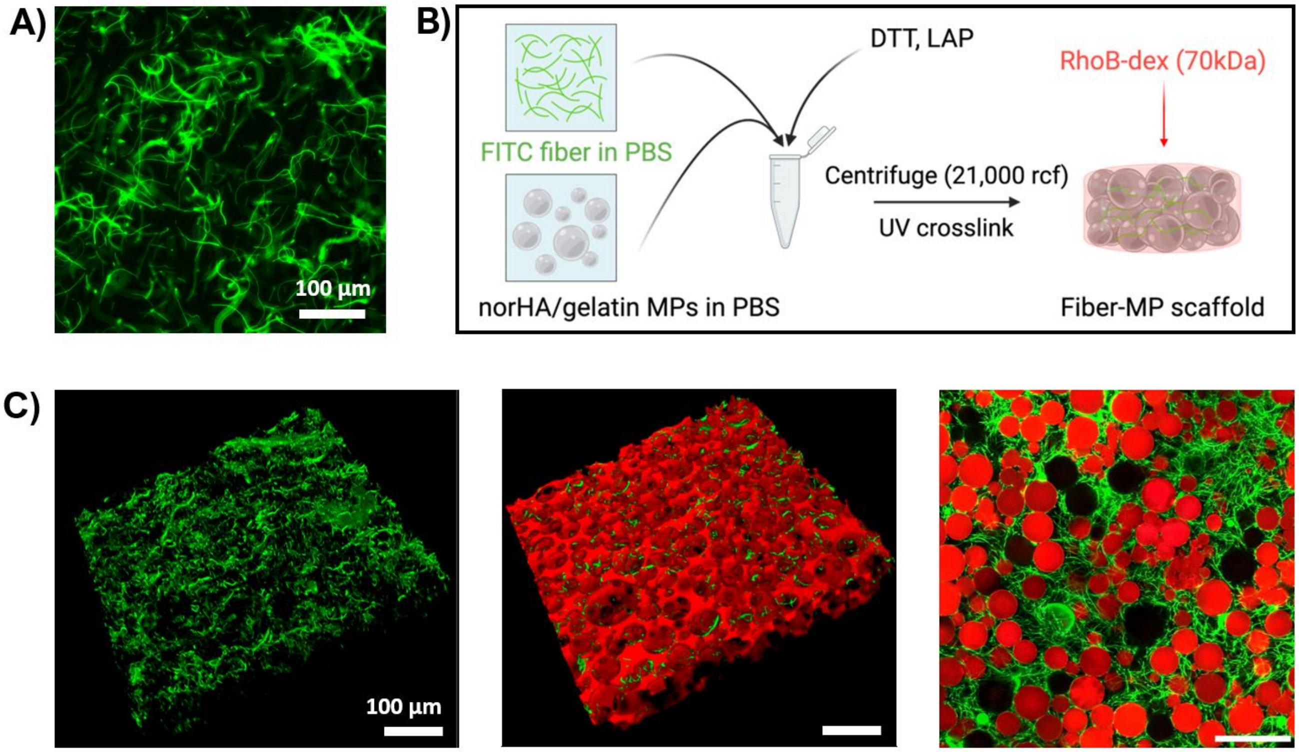

Figure 7. A) Representative fluorescent image of electrospun norHA fibers. A more dilute population of fibers was used for quantification of fiber sizes. **B)** Electrospun fiber incorporation into the scaffold. Fibers and desired ratios of norHA and gelatin HMPs were combined, along with DTT and LAP. The mixture is jammed through centrifugation and UV-crosslinked; then submerged in rhodamine B-dextran for imaging. **C)** *Left and middle:* 3D confocal image of fibers within the scaffold, and fibers combined with interstitial space (in red) within the scaffold. *Right:* Representative 2D confocal image of fibers (green) and norHA HMPs (red) in a 50% scaffold. All scale bars = 100µm.

retained ~70% of their initial mass without fiber reinforcement after 28 days of culture in PBS. Incorporation of 1%, 5%, and 10% fiber into 100% norHA scaffolds retained more mass (up to 80%) by the end of culture; however, there were no statistically significant differences, suggesting that these scaffolds are suitable for long term culture without fiber reinforcement. In 75% norHA scaffolds, the incorporation of fibers markedly enhanced the scaffold stability in long-term culture (Figure 8A). After the initial mass loss between day 0 and day 1 as the result of the removal of sacrificial particles, significant mass loss continued in scaffolds with 0% fiber. By day 7, only ~50% of the scaffold remained for 0% fiber scaffolds. Scaffolds with 1% fiber did not show significant differences compared to 0% fiber scaffolds for the first 6 days. However, from day 7 on, 1% fiber scaffolds degraded significantly less than 0% fiber scaffolds. At day 28, ~7% of 0% fiber scaffold and ~32% of 1% fiber scaffold remained. Neither group retained their shape at 28 days In comparison, both 5% fiber and 10% fiber scaffolds held their shape over the 28 days of our study, and both retained >50% of their initial weight, which included the mass of the gelatin HMPs. Additionally, at no point of the study were the two groups statistically different from each other, indicating that both 5% fiber and 10% fiber scaffolds were suitable for maintaining stable GHSs in long-term culture.

In our most porous scaffold group (50% norHA), the reinforcement effect of fibers was the most pronounced (Figure 8A, B). Without the incorporation of fibers, dissociation of 50% norHA scaffolds started by day 3, with scaffolds breaking apart into smaller pieces and losing most of their weight. Adding 1% fiber delayed the start of dissociation, but no scaffolds remained after 6 days. Incorporation of either 5% and 10% fibers in 50% norHA scaffolds was able to stop the scaffold from dissociating, with 10% fiber incorporation retaining significantly more scaffold mass after 28 days. Further, while both 5% fiber and 10% fiber incorporation were able to keep the scaffolds from dissociating, only 10% fiber scaffolds were able to maintain their shape over the course of the study, a representative image is shown in Figure 8B. Confocal microscopy of 50% norHA scaffold with 10% fiber on day 28 showed that the internal structure of the scaffold was preserved, with porosity comparable to newly made 50% norHA scaffolds (Figure 8C), demonstrating that the fibers both had minimal effects on porosity and the potential to preserve pore spaces within the highest porosity scaffolds over weeks in culture.

We also investigated whether fiber incorporation strengthened the mechanical properties of HMP scaffolds using non-destructive oscillatory rheology. We measured the shear modulus of 100% norHA scaffolds, 75% norHA scaffolds, and 50% norHA scaffolds, with no fibers or with 5% fiber. We chose 5% fiber incorporation only, because it provided significant short-term reinforcement, corresponding to the time scale of this experiment. The storage moduli were measured for all groups prior and after gelatin HMP liquefication.

In all scaffolds with sacrificial gelatin HMPs, liquefication of gelatin HMPs resulted in significant decreases in scaffold moduli (Figure 8D). Prior to gelatin HMP liquefication, however, there were no significant differences in storage moduli in all groups. 5% fiber incorporation was able to rescue some of the reduction in scaffold modulus from gelatin liquefication (Figure 8D). For 50% norHA scaffolds, the differences in the storage modulus of scaffolds prior and after gelatin liquefication were compared; statistical significance was shown between non-fiber reinforced scaffolds and 5% fiber scaffolds. For 75% norHA scaffolds, while 5% fiber incorporation reduced the decrease in storage modulus after liquefication, no statistical significance was shown. Combined, these data showed that up to 5% fiber incorporation did not reinforce the scaffolds by increasing the storage modulus of system. Rather, fiber incorporation reinforced the scaffolds by alleviating the loss in modulus resulted from liquefication of gelatin HMPs. These results suggest that low amount of fibers (5%) work to passively tether the HMPs together rather than changing the bulk properties of the scaffold. This allows for the decoupling of scaffold bulk mechanical properties and scaffold integrity, offering more control in HMP scaffold design.

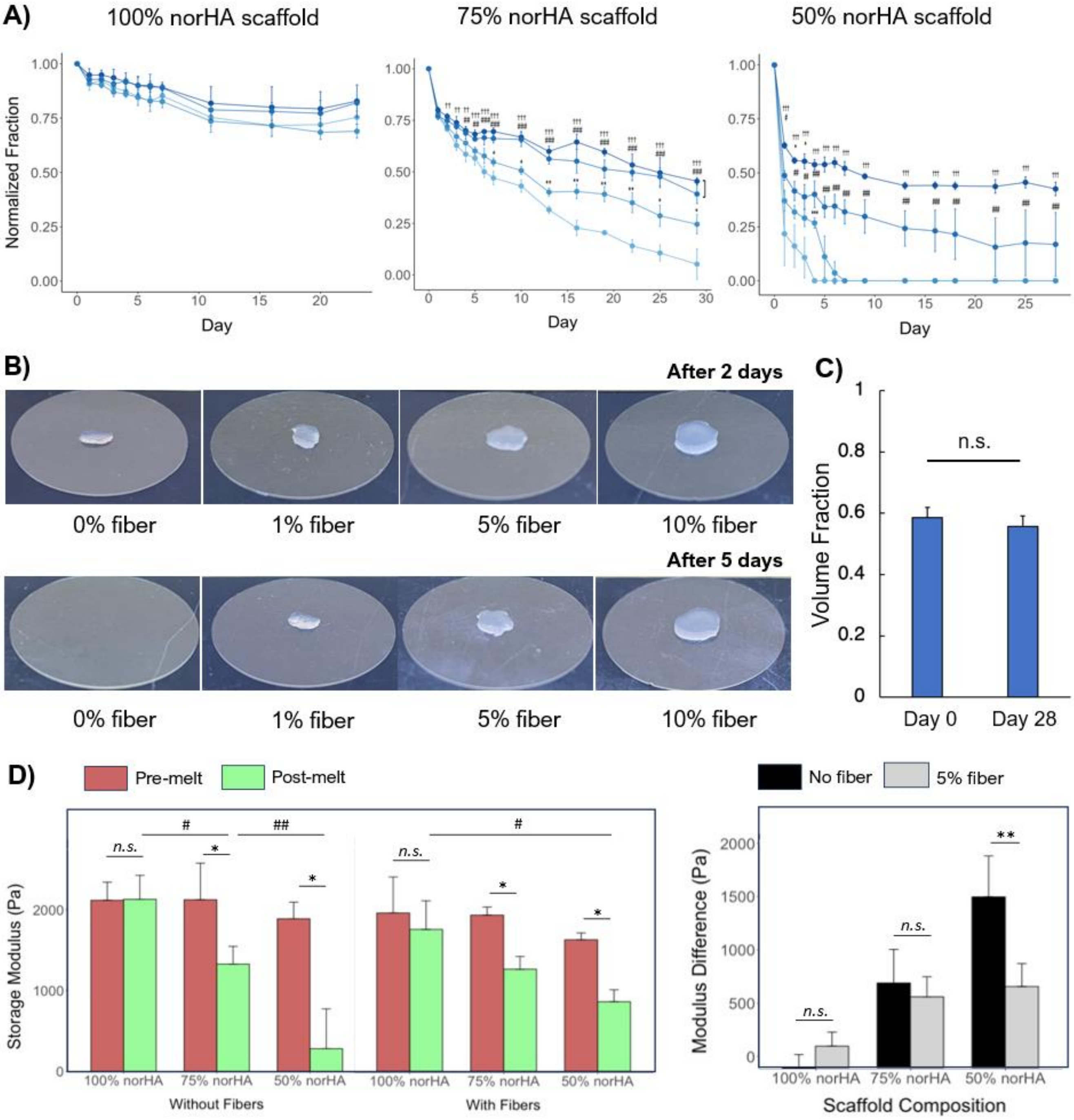

Figure 8. A) Remaining weight fraction of scaffolds tracked over 28 days normalized to scaffold weight at day 0. **B)** Visual presentation of effect of fiber amounts on 50% scaffold degradation over a period of 5 days. **C)** Porosity for 50% scaffold with 10% fiber at day 28 compared to day 0. D) *Left:* Rheological quantification of storage moduli of all scaffolds prior to and after gelatin HMPs liquefy. *Right:* Quantification of the moduli differences for each scaffold before and after gelatin liquefication.

Injection of cell-HMP mixture and subsequent crosslinking retained high cell viability

Injectable biomaterials in regenerative applications allow for minimally invasive administrations of therapeutics. The self-assembling, shear-thinning, and self-healing properties of granular hydrogels make these microporous materials particularly promising for both injection and for cell culture, promoting cellular infiltration and tissue remodeling. To assess our system as an injectable, cytocompatible material, we extruded packed, 100% norHA HMPs with cells included among the HMPs (Figure 9A). Subsequently, we crosslinked the HMPs into a scaffold and assessed cell viability. Human umbilical vein endothelial cells (HUVECs) were used in this study to show that our granular scaffold system could support cells critical for vasculature formation.

To discern the effects of processing the cells within the material from the effects of the material itself on cell viability, viability was assessed at distinct steps during material preparation and extrusion. Specifically, a live/dead assay was performed (1) prior to the extrusion process to assess if the processing of cells within the materials was adverse to cell survival, (2) immediately after extrusion and UV cross-linking to discern the effect of injection and crosslinking on cell viability, and (3) after three days of culture to assess cell survival and proliferation in the scaffold.

We showed that cell viability was maintained at all steps in the process. On day 3 of culture, HUVECs visibly adhered and spread on the HMPs (Figure 9B). After the initial process of mixing cells within the packed HMPs, HUVEC viability was observed to be between 80%-90%, preserving a high degree of cell viability for continued culturing. This viability was maintained through extrusion, with measurement immediately after extrusion, suggesting minimal cell deaths occur from the injection and crosslinking process. After 3 days of culture, a slight reduction in cell viability was observed. This might be attributed to delayed effects of the extrusion process as well as the lower porosity in 100% norHA scaffolds.

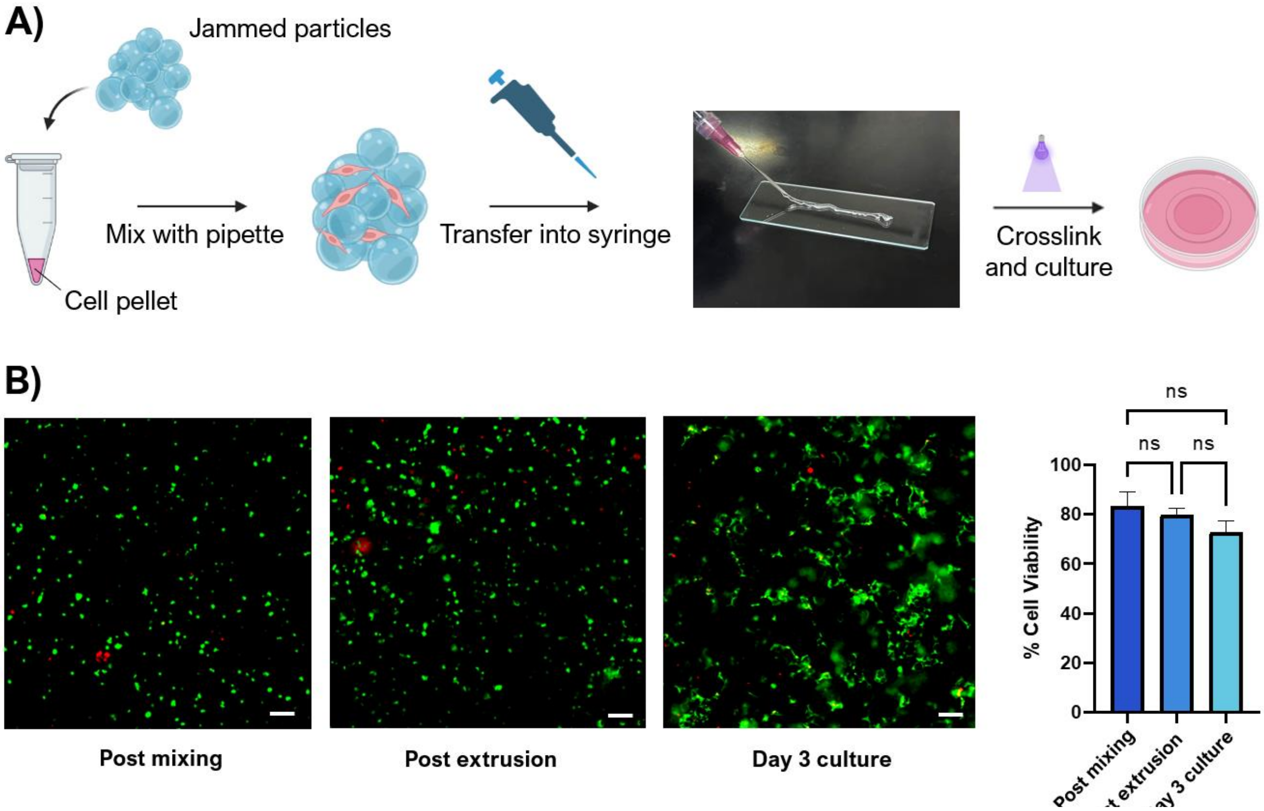

Figure 9. A) The process for HUVEC incorporation, extrusion, and scaffold formation. **B)** Representative images of live/dead stain carried out independently after HUVECs are mixed with HMPs (left), after the cells-HMPs mixture are extruded through the syringe (mid), and after 3 days of culture (right). **C)** Quantified cell viability for each timepoint in panel B.

Together, our current results indicated that the granular hydrogel systems are biocompatible, support cell viability through extrusion, and might serve as platforms for delivering cells within biomaterials that can be designed to be highly porous. These extrudable materials might be leveraged in 3D bioprinting and regenerative engineering applications.

Conclusion:

We were able to fabricate norHA HMPs with varying sizes and moduli rapidly using this batch emulsification.. Through efficient norbornene-thiol click chemistry, norHA HMPs was secondarily crosslinked to each other, as well as conjugated with thiolated RGD to facilitate cell growth. We showed that by introducing a population of sacrificial particles, we were able to tune the porosity and create mulit-scale, interconnected pores. Porous scaffold with as much as 50% porosity can be made viable for long term culture through the introduction of electrospun fibers. 10% v/v fiber incorporation was able to stabilize scaffolds with 50% porosity over a period of 30 days, retaining both the scaffold porosity and structure. Finally, we showed that the HMPs we generate are suitable for cell culture; and that HUVECs were able to survive mixing, injection, as well as subsequent UV crosslinking in the HMPs with high viability. The presented approach allows for easy fabrication of highly porous GHSs with well-characterized pore spaces. Additionally, reinforcement of crosslinked HMPs enabled by small amounts of electrospun fibers has not been previously explored; and is shown here to be a viable method to reinforcing even highly porous HMP systems. Combined, the methods presented in this paper may enable an additional degree of freedom in designing granular materials for various tissue engineering and regenerative medicine applications.

Experimental methods:

NorHA synthesis and characterization:

norHA was synthesized through a previously described method[32]. Briefly, HATBA was made by first dissolving sodium hyaluronate (lifecore biomedical) in water and adding Dowex® 50WX8 hydrogen form (Sigma). After filtering the resin at the end of the ion exchange, tetrabutylammonium hydroxide (Fisher) was used to titrate the filtered solution until pH reaches 7. Finally, the HATBA was frozen and lyophilized. To synthesize norHA, HATBA and 4-Dimethylaminopyridine (Sigma) were dissolved in DMSO under anhydrous conditions. 5-norbornene-2-carboxylic acid (Sigma) was then added to the solution. After the reagents became well mixed, di-tert-butyl dicarbonate (Sigma) was added and the temperature raised to 40°C. The reaction was allowed to proceed overnight and terminated by quenching with cold water. The mixture was purified through dialysis and precipitation, then lyophilized. ^{1}H NMR was done to characterize the synthesized norHA by dissolving lyophilized norHA at 10mg/mL in D_2O. NMR was conducted using a 600MHz NMR machine (Varian, Inova).

NorHA HMP fabrication:

norHA was dissolved at the desired weight percentages in PBS (2 wt%, 3 wt%, and 4 wt%). Then, 60mM LAP (Sigma) in PBS was added to adjust the final LAP concentration to 6mM. DTT (Sigma) was also added to reach final concentrations of 1mM of DTT per 1 wt% of HA in solution. After fully mixing, the solution was added to light mineral oil (Fisher) with

2% Span 80 (Sigma) at a ratio of 1:9 (solution : oil). The oil-solution mixture was then emulsified for 3 minutes at desired speed, then UV crosslinked for 15 minutes under stirring.

To retrieve the HMPs from oil and eliminate surfactant, the HMP-oil emulsion were first centrifuged at 3,000 rcf for 2 minutes. After discarding the oil, the HMPs were resuspended in hexane and centrifuged at 3,000 rcf again for 2 minutes. This was repeated twice. After the hexane wash, the HMPs were then resuspended in isopropanol and centrifuged at 1200 rcf for 5 minutes. The isopropanol wash was repeated twice to wash off the remaining hexane and sterilize the HMPs at the same time. aAter discarding the excess IPA, the norHA HMPs were resuspended and rehydrated in PBS. This process can be done sterilely to generate culture-ready particles. Finally, the HMPs were filtered through a cell strainer (Pluristrainer, Fisher) with mesh sizes ~1.5x the largest diameter HMP in the distribution to eliminate particle clusters formed through aggregation or faulty crosslinking.

Gelatin HMP fabrication:

Gelatin from bovine skin, type B (Sigma) was dissolved in PBS at 10wt% at ~40°C. The solution was then added to light mineral oil with 2% Span 80 (also heated to ~40°C) and emulsified at desired speed for 3 minutes. The emulsion was then allowed to cool to room temperature to form HMPs. Once cooled, the gelatin HMPs were washed and processed in the same way as norHA HMPs.

Size characterization of norHA HMPs:

norHA HMPs suspended in PBS at 1:1 volume ratio were centrifuged at 21,000 rcf for 5 minutes. After discarding the excess PBS, 2mM of thiolated peptide-rhodamine B (sequence GCGKKKG-RhoB) suspended in PBS was added at equal volume to the HMPs to achieve a final concentration of 1mM rhodamine B. 10mM LAP was also added to the solution to reach a final concentration of 1mM LAP. The HMPs were then vortexed with the solution so that particles are sufficiently suspended. The suspension was then placed under UV light for 5 minutes at 10mW/cm^2. After conjugation, the HMP suspension was centrifuged at 21,000 rcf for 5 minutes again. The excess solution discarded and the HMPs were resuspended in fresh PBS. This washing step is repeated until no color was seen in the PBS after centrifugation.

The now fluorescent HMPs were imaged using a Leica DMi8 widefield microscope. HMPs were first diluted 1:100 volume ratio in PBS. Then 200μL of the suspension was added to a glass-bottom confocal dish and imaged on the microscope. Further dilution was carried out as needed so that HMPs do not overlap each other in the final micrograph. The image was then processed in FIJI, which delineated and analyzed the size of each particle. Plotting and statistical analysis was done using Rstudio. Welch's ANOVA and Games and Howell post-hoc test was done for all hypothesis testing.

Rheological tests for HMP flow properties:

A DHR-3 rheometer (TA instruments) was used for all rheology testing. For all flow property assessments, the HMP samples were conditioned by pre-shearing at 100 s^{-1} for 10 seconds. Samples were then allowed to equilibrate for another 2 minutes before conducting measurements. All gap sizes are set to be 10 times greater than the larges HMP size in the population. Rheology tests are conducted on a Peltier plate, with a 20mm sandblasted solvent trap parallel plate geometry and temperature control at 20°C. For frequency sweeps, after conditioning, 1% strain was applied at frequency ranging from 0.01 Hz to 10 Hz in logarithmic increments. For strain sweeps, frequency was kept at 1 Hz, with strain varying from 0.01% to 500%, also in logarithmic increments.

Fabricating porous norHA scaffolds:

To create norHA scaffolds with varying porosity, both norHA HMPs and gelatin HMPs were first suspended in PBS at 1:1 volume ratio. From here, desired amount and ratio of both populations were calculated, and the appropriate amounts were mixed together. 10mM LAP and 25mg/mL DTT were added to the mixture to achieve a final concentration of 1mM for both. This mixture was then centrifuged at 21,000 rcf for 5 minutes; excess solution was discarded.

To crosslink the HMPs, desired amount HMPs from the last step was transferred with a wide-bore pipette tip. The HMPs were then UV crosslinked for 1 minute at 10mW/cm^2. For HMP scaffolds with gelatin HMPs incorporated, PBS were added to cover the scaffold and the scaffolds were cultured in a 37°C, humidified incubator for 20 minutes to liquefy the gelatin HMPs.

Porosity characterization of norHA scaffolds:

All norHA scaffolds were fabricated as described above. After scaffold formation, all scaffolds are submerged in 1mg/mL FITC-dextran in PBS and cultured at 37°C for >20 minutes. These scaffolds were then imaged under a Leica confocal microscope (Stellaris 5).

To assess the porosity of each scaffold, at least one and up to four randomly sampled region was chosen for each scaffold. For each region, Z-stack images were taken to penetrate 100μm into the scaffold, with step size no larger than 5μm. The images were thresholded with FIJI and the pore fraction for each slice calculated. The final porosity was estimated by the average of each Z-stack image. If multiple regions were selected, the porosity from all Z-stack images were averaged to be the final porosity of the scaffold. Replicates of at least 3 were done by fabricating a new scaffold for each replicate and repeating the above process.

Pore space 2-D analysis:

To analyze the pore spaces in porous scaffolds, the same microscopy images were used as those for characterizing porosity. After thresholding in FIJI, the pixel values (0 or 256) and their corresponding XY coordinates were exported as a .csv file. An in-house Matlab program was built to utilize the pixel value and position data to find interconnected pixels that form the pore spaces. The area of each pore space was then calculated in Matlab.

Area fraction was found by first defining number of bins desired for graphic representation. Then, area fraction was calculated by dividing the sum of the pore areas in the same bin by the total pore area. The average pore area of each bin was used as the x-axis value in the distribution graph.

LOVAMAP analysis of 3-D pore space:

norHA HMPs used for imaging was made fluorescent using AF 430 tetrazine(Lumiporbe). Briefly, norHA HMPs suspended in PBS were centrifuged at 21,000 rcf for 5 minutes. The excess PBS was discarded and 1mM AF tetrazine was added at equal volumes to the HMPs (final concentration 0.5mM AF tetrazine). The mixture was then vortexed to resuspend the HMPs. The reaction was allowed to proceed for 20 minutes, after which the HMP suspension was centrifuged again at 21,000 rcf for 5 minutes. The excess solution was discarded and replaced with fresh PBS. This process was repeated until the solution became clear after centrifuging the HMPs. All scaffolds were fabricated without fiber as described above. The scaffolds were imaged in PBS using a Leica confocal microscope (Stellaris). A 20x objective was used and Z-stacks of 100 μm was taken for each scaffold.

Electrospinning norHA fibers:

electrospinning solution containing 3.5% w/v norHA, 2.5% w/v 900 kDa polyethylene oxide (PEO, Sigma), 0.05% I2959 (Sigma), and 6.5 mM DTT in deionized water was dissolved overnight. The solution was extruded using a syringe pump at a flow rate of 0.4 mL/hr through a 16G needle. The fibers were collected on an aluminum foil substrate attached to a mandrel spinning at ~1,000 rpm. 13-16 kV positive voltage was applied to the needle and 4kV negative voltage was applied to the collection substrate.

After collection, fibers were crosslinked under UV light for 15 minutes at 10mW/cm^2 under nitrogen. Once crosslinked, the fibers were wetted with PBS to detach from the collection substrate, then suspended in PBS. The suspension was homogenized at 9,000 rpm for 2 minutes and then filtered through a 40 μm cell strainer (Fisher) to eliminate large aggregations of fibers.

norHA fiber characterization:

fluorescent fibers were made by incorporating 4mg/mL FITC-dextran (1 MDa, Sigma) in the initial electrospinning solution. All other steps were the same to produce fluorescent fibers. After filtering, fibers were diluted 1:1000 in PBS, and placed between two glass cover slips. Images were taken using a Leica DMi8 widefield microscope and further dilution of the fibers was carried out until fibers no longer overlap each other in the micrograph. The images were then analyzed in FIJI to find the length and width of each fiber.

Characterizing degradation of norHA scaffolds:

non-fiber scaffolds were fabricated as described above. For fiber-reinforced scaffolds, fibers were first centrifuged at 3,000 rcf to form a pellet. The pellet volume was estimated, and the pellet was resuspended 1:10 fiber to PBS volume ratio. To fabricate the scaffolds, desired volume of fiber was calculated (1%, 5%, or 10%), and corresponding volume of fiber was added to the norHA-gelatin HMP mixture (amount measured as described before for 100%, 75%, and 50%). 10mM LAP and 25mg/mL DTT was then added to the mixture to reach a final concentration of 1mM for each reagent. The rest of the fabrication was carried out in the same way as described for fabricating non-fiber scaffolds.

All scaffolds for this study were fabricated on a glass coverslip substrate. Each coverslip was weighed by itself, and then weighed again with the scaffold on top to find the weight of the scaffold. Each scaffold was then submerged in PBS and cultured in a humidified incubator at 37°C. For each degradation time point, the PBS was removed by pipetting and gently wicking off the remaining PBS with a KimWipe. The weight of coverslip and scaffold was then measured again. Plotting and statistical analysis were done in Rstudio. Statistical comparison was done using ANOVA and Tukey's post-hoc test.

Rheological tests for HMP scaffolds:

Time sweeps were done for HMP scaffolds to assess their mechanical properties. Scaffolds were fabricated into disks with 1mm height and 8mm diameter. This is done by first biopsy punching a 1mm thick PTFE sheet (McMasters) to create an 8mm diameter opening. The HMPs were loaded into the opening, then a glass slide is placed on top to flatten the HMPs so that they conform to the opening. Excess HMPs that overflowed between the glass slide and the PTFE sheet were simply wiped away after the glass slide is removed. The HMPs were then photo-crosslinked for 1 minute under 10mW/cm^2 UV light.

Rheology was conducted on a Peltier plate temperature controlled at 20°C. The fabricated 8mm scaffolds were loaded onto the Peltier plate and positioned under an 8mm sandblasted parallel plate geometry. Each scaffold is conditioned by applying a small axial force (0.3-0.8 N) prior to oscillatory testing. This accounts for the potential uneven topography produced during scaffold fabrication and ensures that all scaffold is sufficiently contacting the geometry. Time sweeps were done at 1% strain and 1 Hz frequency for 60 seconds.

To assess mechanical properties of scaffolds post gelatin HMP sacrifice, after time sweep was done for the pre-sacrifice scaffolds, the scaffolds were submerged in PBS and cultured for 20 minutes at 37°C. After culturing, the scaffolds were gently washed with excess PBS, also at 37°C, to remove liquefied gelatin. The same time sweep with conditioning was conducted again on the scaffolds. Statistical analysis was done using paired t-tests for these samples.

Injection of HUVEC and HMPs:

HUVECs (Lonza) was cultured in EGM-2 medium (Lonza) at 5% CO2 and 37°C in a humidified environment. HUVECs Passage 6-8 was used for this experiment. HUVECs were detached from plate using 0.05% trypsin, centrifuged at 300 rcf for 3 minutes, and resuspended in EGM-2 at 30 million cells per mL.

RGD-modified norHA HMPs were made by mixing the norHA HMPs with RGD and LAP to reach a final concentration of 1mM RGD and 1mM LAP (norHA HMPs comprises half the volume of the solution). This mixture was placed under UV light at 10mW/cm^2 for 5 minutes, then washed twice with PBS to eliminate excess RGD and LAP.

The RGD-norHA HMPs were centrifuged at 21,000 rcf for 5 minutes. The dense HUVEC suspension was then mixed with the HMPs to reach a final density of 2 million cells/mL. The mixture was then loaded into a 1 mL syringe and subsequently extruded onto a 6-well cell culture plate through a bevel, 18G needle. The material was subsequently UV crosslinked at 15 mW/cm^2 for 1 minute.

For live/dead staining, HUVECs-HMPs mixture were collected prior to loading the material into the syringe, while post-printing mixtures were collected either immediately after extrusion or after 3 days of culture. The cells were stained using a Live/Dead viability kit

(L3224, Invitrogen) and imaged in a plastic-bottom culture plate by a Leica DMi8 widefield microscope. Statistical analysis was performed using GraphPad Prism 9. Statistical comparison was made using one-way analysis or variance (ANOVA) with Tukey post hoc test.

References:

1. Cates, M. E., Wittmer, J. P., Bouchaud, J.-P., & Claudin, P. (1998). Jamming is not just cool any more. *Nature 1998 396:6706*, *396*(6706), 21–22.
2. O’hern, C. S., Silbert, L. E., Liu, A. J., & Nagel, S. R. (n.d.). *Jamming at zero temperature and zero applied stress: The epitome of disorder*.
3. Van Hecke, M. (2009). Jamming of soft particles: geometry, mechanics, scaling and isostaticity. *Journal of Physics: Condensed Matter*, *22*(3), 033101.
4. Highley, C. B., Hoon Song, K., Daly, A. C., Burdick, J. A., Highley, C. B., Song, K. H., Daly, A. C., & Burdick, J. A. (2019). Jammed Microgel Inks for 3D Printing Applications. *Advanced Science*, *6*(1), 1801076.
5. Daly, A. C. (2023). Granular Hydrogels in Biofabrication: Recent Advances and Future Perspectives. *Advanced Healthcare Materials*, 2301388.
6. Griffin, D. R., Weaver, W. M., Scumpia, P. O., di Carlo, D., & Segura, T. (2015). Accelerated wound healing by injectable microporous gel scaffolds assembled from annealed building blocks. Nature Materials 2014 14:7, 14(7), 737–744.
7. Qazi, T. H., Muir, V. G., & Burdick, J. A. (2022). Methods to Characterize Granular Hydrogel Rheological Properties, Porosity, and Cell Invasion. ACS Biomaterials Science and Engineering, 8(4), 1427–1442.
8. Riley, L., Schirmer, L., & Segura, T. (2019). Granular hydrogels: emergent properties of jammed hydrogel microparticles and their applications in tissue repair and regeneration. Current Opinion in Biotechnology, 60, 1–8.

9. Lam, J., Lowry, W. E., Carmichael, S. T., & Segura, T. (2014). Delivery of iPS-NPCs to the Stroke Cavity within a Hyaluronic Acid Matrix Promotes the Differentiation of Transplanted Cells. *Advanced Functional Materials*, *24*(44), 7053–7062.
10. Pruett, L. J., Jenkins, C. H., Singh, N. S., Catallo, K. J., Griffin, D. R., Pruett, L. J., Jenkins, C. H., Singh, N. S., Catallo, K. J., & Griffin, D. R. (2021). Heparin Microislands in Microporous Annealed Particle Scaffolds for Accelerated Diabetic Wound Healing. *Advanced Functional Materials*, *31*(35), 2104337.
11. Pruett, L. J., Kenny, H. L., Swift, W. M., Catallo, K. J., Apsel, Z. R., Salopek, L. S., Scumpia, P. O., Cottler, P. S., Griffin, D. R., & Daniero, J. J. (2023). De novo tissue formation using custom microporous annealed particle hydrogel provides long-term vocal fold augmentation. *Npj Regenerative Medicine 2023 8:1*, *8*(1), 1–10.
12. Wilson, K. L., Onweller, L. A., Joseph, N. I., David-Bercholz, J., Darling, N. J., Segura, T., & Segura, T. (2023). SDF-1 Bound Heparin Nanoparticles Recruit Progenitor Cells for Their Differentiation and Promotion of Angiogenesis After Stroke. *BioRxiv*,
13. Charlet, A., Bono, F., & Amstad, E. (2022). Mechanical reinforcement of granular hydrogels. Chemical Science, 13(11), 3082–3093.
14. Hirsch, M., Charlet, A., Amstad, E., Hirsch, M., Charlet, A., & Amstad, E. (2021). 3D Printing of Strong and Tough Double Network Granular Hydrogels. Advanced Functional Materials, 31(5), 2005929.

15. Muir, V. G., Weintraub, S., Dhand, A. P., Fallahi, H., Han, L., & Burdick, J. A. (2023). Influence of Microgel and Interstitial Matrix Compositions on Granular Hydrogel Composite Properties. Advanced Science, 2206117.
16. Wang, W., Chen, X., Meng, T., & Liu, L. (2022). Multi-network granular hydrogel with enhanced strength for 3D bioprinting. Journal of Biomaterials Applications, 36(10), 1852–1862.
17. Anderson, A. R., Nicklow, E., & Segura, T. (2022). Particle fraction is a bioactive cue in granular scaffolds. Acta Biomaterialia, 150, 111–127.
18. Qazi, T. H., Wu, J., Muir, V. G., Weintraub, S., Gullbrand, S. E., Lee, D., Issadore, D., & Burdick, J. A. (2022). Anisotropic Rod-Shaped Particles Influence Injectable Granular Hydrogel Properties and Cell Invasion. Advanced Materials, 34(12)
19. Truong, N. F., Kurt, E., Tahmizyan, N., Lesher-Pérez, S. C., Chen, M., Darling, N. J., Xi, W., & Segura, T. (2019). Microporous annealed particle hydrogel stiffness, void space size, and adhesion properties impact cell proliferation, cell spreading, and gene transfer. Acta Biomaterialia, 94, 160–172.
20. Møller, P. C. F., Rodts, S., Michels, M. A. J., & Bonn, D. (n.d.). Shear banding and yield stress in soft glassy materials.
21. Coussot, P., & Ovarlez, G. (2010). Physical origin of shear-banding in jammed systems. European Physical Journal E, 33(3), 183–188.
22. Divoux, T., Fardin, M. A., Manneville, S., & Lerouge, S. (2016). Shear Banding of Complex Fluids. Annu. Rev. Fluid Mech, 48, 81–103.

23. Ataie, Z., Horchler, S., Jaberi, A., Koduru, S. v., El-Mallah, J. C., Sun, M., Kheirabadi, S., Kedzierski, A., Risbud, A., Silva, A. R. A. E., Ravnic, D. J., & Sheikhi, A. (2024). Accelerating Patterned Vascularization Using Granular Hydrogel Scaffolds and Surgical Micropuncture. Small, 20(8), 2307928.

24. Menut, P., Seiffert, S., Sprakel, J., & Weitz, D. A. (2011). Does size matter? Elasticity of compressed suspensions of colloidal- and granular-scale microgels. Soft Matter, 8(1), 156–164.

25. Liu, Y., Suarez-Arnedo, A., Riley, L., Miley, T., Xia, J., & Segura, T. (2023). Spatial Confinement Modulates Macrophage Response in Microporous Annealed Particle (MAP) Scaffolds. Advanced Healthcare Materials, 12(26), 2300823.

26. Chan, N. R., Hwang, B., Ratner, B. D., & Bryers, J. D. (2022). Monocytes contribute to a pro-healing response in 40 µm diameter uniform-pore, precision-templated scaffolds. Journal of Tissue Engineering and Regenerative Medicine, 16(3), 297–310.

27. Choi, S.-W., Zhang, Y., MacEwan, M. R., Xia, Y., Choi, S., Zhang, Y., MacEwan, M. R., & Xia, Y. (2013). Neovascularization in Biodegradable Inverse Opal Scaffolds with Uniform and Precisely Controlled Pore Sizes. Advanced Healthcare Materials, 2(1), 145–154.

28. Sicchieri, L. G., Crippa, G. E., de Oliveira, P. T., Beloti, M. M., & Rosa, A. L. (2012). Pore size regulates cell and tissue interactions with PLGA–CaP scaffolds used for bone engineering. Journal of Tissue Engineering and Regenerative Medicine, 6(2),

29. Somo, S. I., Akar, B., Bayrak, E. S., Larson, J. C., Appel, A. A., Mehdizadeh, H., Cinar, A., & Brey, E. M. (2015). Pore Interconnectivity Influences Growth Factor-Mediated Vascularization in Sphere-Templated Hydrogels. Tissue Engineering - Part C: Methods, 21(8), 773–785.

30. Yin, Y., He, X. T., Wang, J., Wu, R. X., Xu, X. Y., Hong, Y. L., Tian, B. M., & Chen, F. M. (2020). Pore size-mediated macrophage M1-to-M2 transition influences new vessel formation within the compartment of a scaffold. Applied Materials Today, 18, 100466.

31. Riley, L., Cheng, P., & Segura, T. (2023). Identification and analysis of 3D pores in packed particulate materials. Nature Computational Science 2023 3:11, 3(11), 975–992.

32. Gramlich, W. M., Kim, I. L., & Burdick, J. A. (2013). Synthesis and orthogonal photopatterning of hyaluronic acid hydrogels with thiol-norbornene chemistry. Biomaterials, 34(38), 9803–9811.

Chapter 5: Discussion on porosity and its implications, the future of fiber-reinforced microparticle scaffolds

Discussion on porosity:

We have demonstrated a unique system with high porosity and stable formulation able to withstand long-term culture. While porosity on the same scale has been shown in HMPs made with crosslinked gelatin methacrylate (gelMa), cell culture in gelMa HMPs was only carried out to 7 days[1]. Our system provides a unique approach to reinforce less stable formulations, such as our norHA HMP scaffolds, which completely dissociate by day 5 at ~50% porosity. More importantly, the amount of fiber needed for scaffold reinforcement did not substantially change the total porosity and mechanical properties of the scaffold. Further study is needed to elucidate cell-fiber interactions in our fiber-based scaffold, but based on our current data, we can comfortably present fiber as a component with, at least, no adverse effects to porosity and cellular growth within HMP scaffolds.

Being able to generate robust, soft HMPs with high porosity could have impactful implications in the field of regenerative engineering. Many studies have been conducted on the effect of hydrogel porosity on vasculature ingrowth and tissue infiltration[2-5]. Notably, hydrogels with porosity >60% are often investigated in various regenerative applications, especially bone regeneration[5-9]. These highly porous hydrogels are typically generated using uniformly sized spherical porogens, and usually require harsh or prolonged sacrificial procedures[4,6-9]. Additionally, polymer with high mechanical modulus are typically used to withstand the sacrifice process and uphold the hydrogel structure[3,7,8]. Granular hydrogels beginning with MAP, while giving up some porosity, presented a facile method for an injectable and moldable hydrogel scaffold. This, combined with the ability to use soft and stiff hydrogels alike[10-11], enable a large range of translatable regenerative applications. Going further, our system enables high porosity in addition to the advantages presented by granular hydrogel scaffolds.

So, how much porosity is sufficient porosity? And what, then, is the optimal porosity? These are important questions that the field has yet to fully answer. One of the challenges in answering these questions is that responses provoked by porosity are highly cell-type and context dependent. Bone regeneration, for example, has shown recorded success when pore size is greater than 200 microns[4,8,9,12]. Pores less than 200 μm in size did not support deep infiltration, due to limited nutrient diffusion and insufficient vascularization[9,12]. In one study, uniform pore sizes have been shown to promote bone formation up to 600 μm[9,13], with a reduction in bone formation as pores became larger. However, pores on the order of 1mm showed the highest osteoblast gene expression, suggesting a combination or gradient of pore sizes may be needed to achieve optimal pore characteristics for bone regeneration[9]. Chondrocytes, on the other hand, seemed to prefer microcavities on the order of 80-120 μm based on evidence from in vitro studies[14,15]. To complicate things further, vascularization studies using porous materials have shown no consensus in the optimal pore sizes, with evidence showing optimal vascular formation in either ~100-μm or ~40-μm pores[16-18].

An additional confounding factor is that pore size is not sufficient to describe pore characteristics. For instance, the total porosity of the material is an important metric with implications for accessible volume within the material and interconnection between pores.

Porosity, while connected to the pore sizes, is not defined solely by this parameter. Large pores can be formed, for example, using large spherical porogens in a bulk hydrogel; however, the porosity of the final hydrogel will depend on the number of porogen used: discrete, large pores can exist in a low-porosity hydrogel. In practice, therefore, studies that rely on spherical porogen-templated hydrogels typically use packed spheres to ensure that all pores are interconnected and thereby accessible[13-15,17,19-21]. The final porosity is not always reported in these studies; however, we can infer that the porosity will be quite high if the spheres were truly packed, as the body-centered cubic packing fraction for non-deformable, uniformly sized spheres is 0.68. Other factors typically encountered in studies including heterogeneity in particle sizes, dense packing, and deformable particles will only increase the packing fraction, and thus porosity greater than 68%. Granular hydrogels, on the other hand, require less concern pertaining the interconnectedness of pores. Packed particles have inherently interconnected pores – this allows the fabrication of the porous hydrogel mentioned above, the process of which involves liquid precursors infiltrating the space among packed particles. As a result, fully packed hydrogels possess interconnected pores on the order of 10s of μm in size as well as low porosity[22-26] (10-20%), whereas porogen-templated hydrogels with pore sizes on the same magnitude are high in porosity[17,18,27-30]. Therefore, both pore size and porosity must be considered in characterizing a system, as they have large implications on the accessibility and connectivity of the porous space.

If we take it a step further to discern the characteristics of pore shapes and interconnections between pores, even more complications arise. In granular hydrogels where pores are the void spaces created from packing, the pores are irregular. Studies in granular hydrogels have shown that pore shape – especially shapes with high aspect ratios – can affect cellular infiltration and behavior significantly[31,32]. These irregular pores, typically 10s of μm in size form narrow, corridor-like interconnections, where, going from one pore to the other, the connecting available volumes become increasingly smaller and finally becoming larger again as we move closer to the next pore[33]. Porogen-templated hydrogels, on the other hand, have round pores and typically form interconnections through contact between porogens prior to sacrifice[20]. The area of contact determines the size of interconnections after porogen leeching and can be controlled by altering the packing intensity. Compared to granular hydrogels, where cells must travel the corridor-like interconnections to migrate between pores, interconnections in porogen-templated hydrogels draw more similarity to doors, requiring less traversal from cell to cross. Studies that increased the "door" sizes of the interconnections has been shown to have beneficial effects to cellular ingrowth[13,20], and the interconnectedness of the pores have been shown to have important roles in facilitating tissue ingrowth[12]. For granular hydrogels, this effect has not been elucidated, as the interconnecting volumes are linked to total porosity and are difficult to alter independently. However, the beneficial effects from having higher porosity in granular hydrogel scaffolds are likely a result of increased size of interconnecting volumes.

Finally, the mechanical properties of the hydrogels can differentially affect cells[34-37]. Higher stiffness hydrogels, which typically promotes cell spreading and osteogenesis[37], are prime candidates for bone regeneration and used extensively in porogen templating due to their excellent mechanical integrity. Softer hydrogels, on the other hand, are typically used as granular systems and have shown success in many studies for soft tissue[10] as well as cartilage regeneration[11]. This introduces another confounding factor, especially for in vivo studies, as the stiffness of the hydrogel significantly alters the immune cell[38,39] and stromal cell[40-44] behavior that are integral to the local microenvironment and the wound healing process. As a result, porosity studies using hydrogels that differ in mechanical property cannot be easily compared to each other, especially when regenerative studies are carried out in different tissues.

In summary, porosity and pore characteristics are complex 3D spaces that have not been adequately characterized. Pore shapes, interconnections, and pore sizes vary vastly between systems, and there are not yet unifying descriptors in the field to quantify these characteristics. Additionally, these characteristics often cannot be changed independently, making it challenging to isolate and fully understand the effect of singular parameters. There are, however, general trends to be discerned from individual studies that can serve as guidelines to designing porosity. In the following, I will discuss some of these trends and how our unique scaffold system fits in as a scaffold with promising pore characteristics.

First, hydrogels with microscale porosity perform better than bulk hydrogel controls, which are typically nanoporous[22]. However, further increases in porosity and pore size do not linearly correlate with enhanced tissue regeneration or altered cell behaviors beneficial to regeneration. This effect has been shown for different systems on different size scales. For pores with sizes 100 μm and above, multiple studies have shown increases in tissue formation as pore size increased. However, as pore sizes approach 400 μm and above, either no increased tissue formation was observed[13], or decreased formation was found[9], suggesting an optimum pore size range for tissue formation under regenerative contexts. This could be due to the difficulty for cells to bridge the large void spaces created with large, spherical porogens. Perhaps more interestingly, for pores on the order of 10s of μm, multiple studies have shown that pores with size of ~40 μm encouraged better vessel formation[17,18] compared to pores with larger sizes. In on of the studies, populations of macrophages skewed toward the M1 phenotypes inside the pores but more M2-skewed populations were present outside the pores[18]. Other studies have also shown that M2-like macrophage increase as pore sizes become bigger[45,46]. This suggests the important role pore sizes could play on immune-mediated wound healing in porous scaffolds. Additionally, studies using 40-μm pores for ophthalmologic regeneration[17] and cardiac regeneration[27] have shown beneficial effects, further validating 40 μm-sized pores as a promising candidate for tissue regeneration.

Hydrogels incorporating heterogenous pores have been suggested to promote better tissue formation[9]. Studies focused on heterogeneous pores are mostly concerned with biomimetic multiscale porosity, often using a combination of 3D printing and porous hydrogels. The effect of heterogeneity on a smaller scale (100s of μm to 10s of μm), however, have not been systematically studied. While little experimental studies have been done, Mehdizadeh et al. computationally modeled angiogenesis using computer-generated porous scaffolds with spherical pores and an agent-based angiogenesis model[47]. In this work, they showed that angiogenesis correlates positively to pore size as pore size increased from 100 to 400 μm. Better angiogenesis was also found when porosity and interconnectivity increased. Furthermore, they altered the distribution of pore sizes by changing the standard deviation of pore distributions, which allowed changes in the degree of heterogeneity. Interestingly, they found that a wider distribution in pore sizes (higher heterogeneity) positively correlated to blood vessel growth for all pore sizes and porosities. This model does not consider immune cross-talks that influence vessel formation in smaller pores; however, it shines light on the profound effect of pore spaces on blood vessel growth and formation. Combined, evidence from current studies suggest that a heterogeneous system may be desirable for regeneration: what if both pores >100 μm (infiltration-promoting) and ~40 μm (angiogenesis-promoting) co-exist in the system? Would we get the best of both worlds? Or, would we see one effect dominate over the other?

Our system as heterogeneously porous scaffolds:

Our system – granular scaffolds with sacrificial particles – may be able to provide a start to answering this question. With the help of LOVAMAP, we were able to understand our pore spaces to great depths. As shown in the last chapter, pore with volumes on the order of 10s of picoliters (created from packing) to 10,000 of picoliters (single interconnected pore comprising most of the porosity). While this showcases the interconnectivity of our scaffolds, it is difficult to draw comparison to porogen-templated hydrogels, the pore sizes of which are typically quantified in length scales, to reflect the diameter of the porogen from which the pores arose. One descriptor not mentioned in the last chapter, however, could help paint a better picture in relation to porogen-templated hydrogels. As shown in Figure 1. LOVAMAP can calculate the largest enclosed sphere in each pore. Data from

50% norHA scaffold show that pores containing largest spheres with diameters from ~1 µm to ~90 µm exist. This, however, does not mean that our largest pore is 90 µm in size. Rather, our largest pore is an expansive 3D volume with a size much greater than a 90-µm diameter sphere, within which a 90-µm sphere could fit. This could be advantageous to cell growth within the pore, as cells do not have to bridge distances further than 90 µm. More work is still needed to quantify the shape of our large pores in meaningful ways, but we can comfortably claim that our pore spaces contain a large range of pore sizes relevant to tissue infiltration and angiogenesis, with higher interconnectivity than typical granular hydrogel scaffolds.

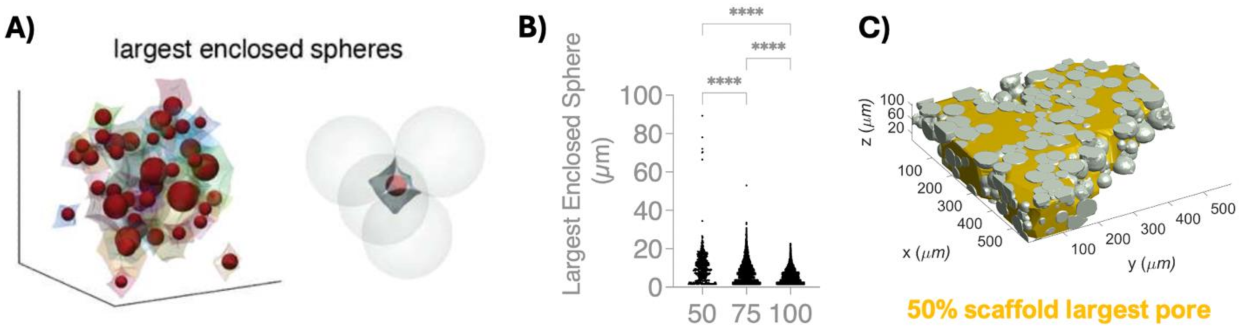

Figure 1. A) LOVAMAP visualization of largest enclosed sphere. **B)** LOVAMAP output of largest enclosed sphere in scaffolds of varying compositions. **C)** Representative largest pore in 50% norHA scaffold.

To see if our scaffold system with heterogeneous pore spaces can enhance cell growth and infiltration, we first cultured HUVECs using our scaffolds with varying porosity. We selected HUVECs again as our model cell type because supporting vasculature cells are of critical importance in tissue engineering as well as regeneration. We fabricated 100%, 75%, and 50% norHA scaffold with HUVECs incorporated at a density of 10 million cells per milliliter scaffold volume. As shown in Figure 2, after 4 days of in vitro culture, actin and nuclear stain showed a significant increase in cell numbers as porosity increased from

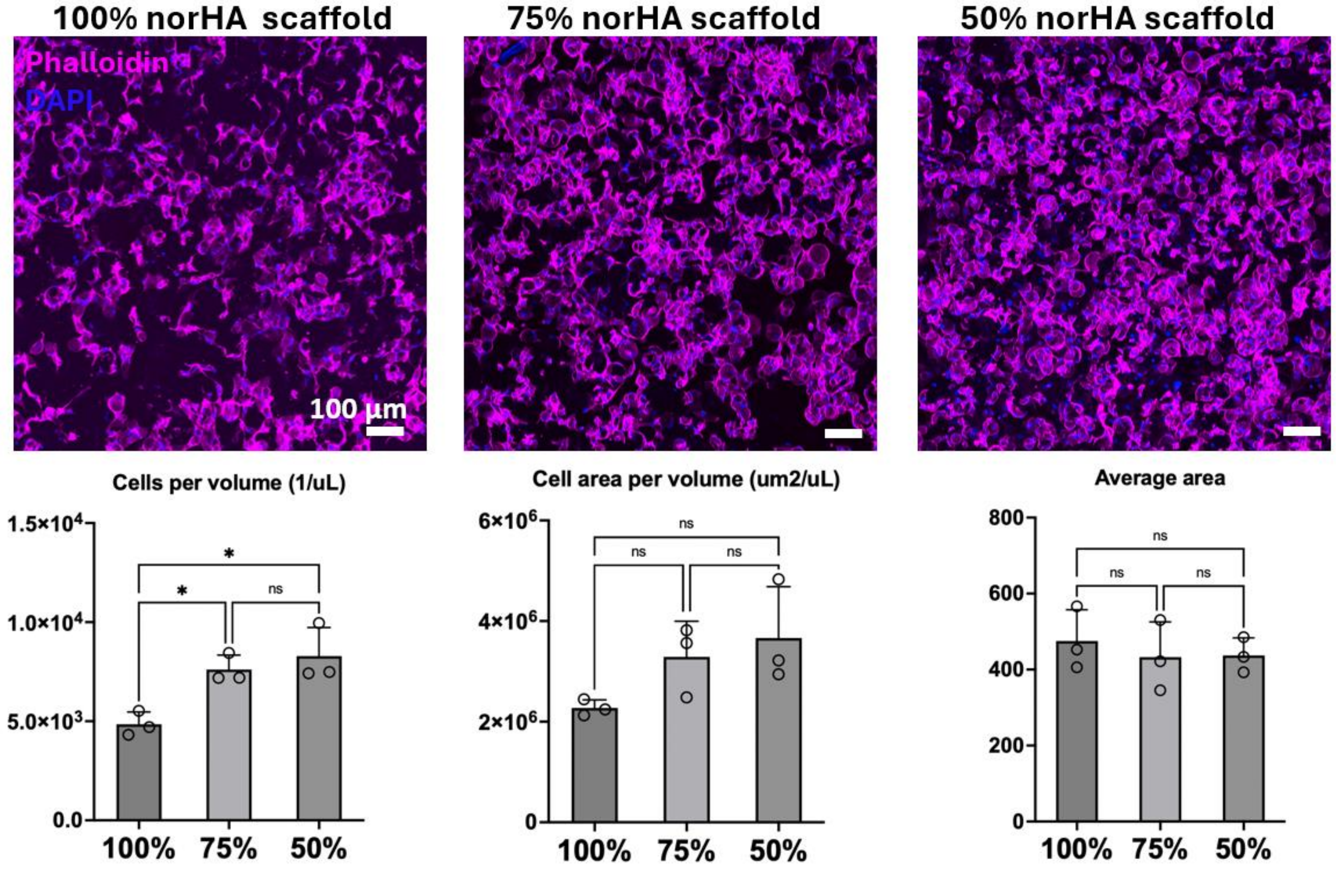

Figure 2. ***Top:*** max projection image (100 microns) of HUVECs cultured for 4 days in scaffolds of varying compositions. ***Bottom:*** from left to right: number of cells per scaffold volume based on nucleus count; total cell area per volume based on actin stain; and average cell area.

~10% (100% norHA scaffold) to ~25% (75% norHA scaffold). Further increase in porosity upheld the trend of increasing cell numbers but was not statistically significant. Quantification of cell area did not show a significant difference in average individual area (Figure 2), suggesting that cell spreading was not significantly altered. Here, the heterogeneity of the scaffold (largest heterogeneity in 50% scaffold) did not appear to have a significant effect on proliferation, likely due to having less physical space on which to spread and grow as porosity increases: HUVECs did not seem to bridge the larger gaps between HMPs, but rather spread on the surfaces of the HMPs. Thus, while higher porosity provided higher surface area per volume, the available volume to HUVECs decreased as the trade-off.

Next, we wanted to understand cellular infiltration and migration within the scaffold. HUVEC and MSC spheroids were generated as described by Qazi et al[31]. Spheroids were randomly distributed in 100%, 75%, and 50% norHA scaffolds and cultured for 4 days before staining. Preliminary analysis showed that a small increase in total spheroid area was seen as porosity increased to ~25% (75% scaffold, Figure 3). Strikingly, spheroid cultured in 50% scaffold spread extensively into the surrounding space, and appeared to adopt a different morphology, with thinner but further reaching branches (Figure 3). Spheroid area analysis based on fluorescent presence showed marginal increases as porosity increased (Figure 3). This, however, did not adequately reflect the significantly larger spread area of the 50% scaffold spheroid. Hull area analysis, on the other hand, allowed us to quantify the area covered by the spreading spheroid (Figure 3), and showed that 50% scaffold had almost a magnitude increase in hull area compared to all other scaffolds. This result was somewhat unexpected and provides a stark contrast to our HUVEC culture results, where increase in porosity from the 75% scaffold to 50% scaffold provided little benefit. We contemplate that heterogeneity provided a significant effect on our infiltration and migration model, where, in contrast to cellular proliferation, cell outgrowth originates from an established structure (the spheroids). As cells are supported by the spheroid, they can benefit from the void area for unimpeded migration, in the meantime, smaller pores may act as support and help provide continuity among the large void volumes.

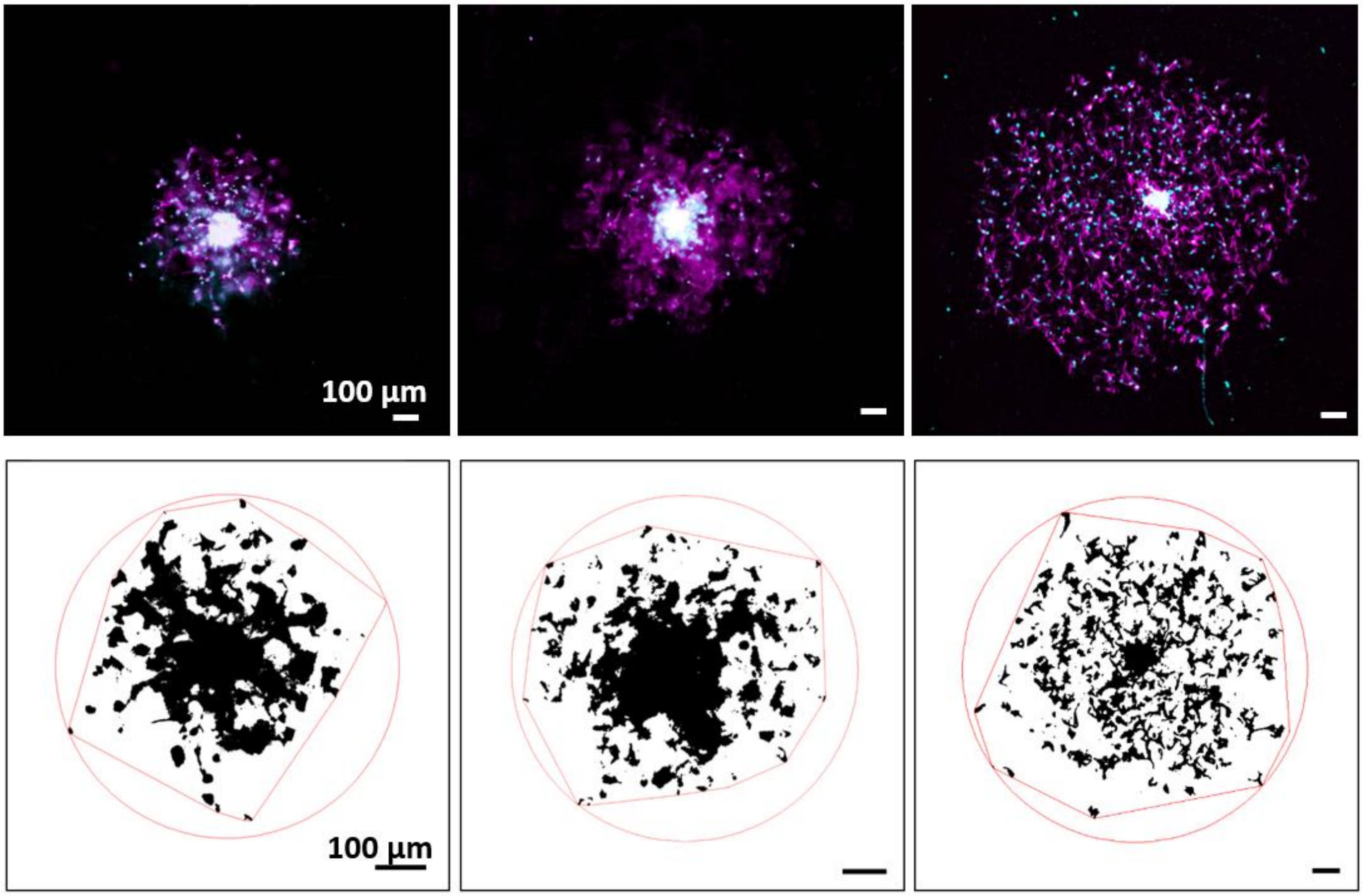

100% norHA scaffold   75% norHA scaffold   50% norHA scaffold

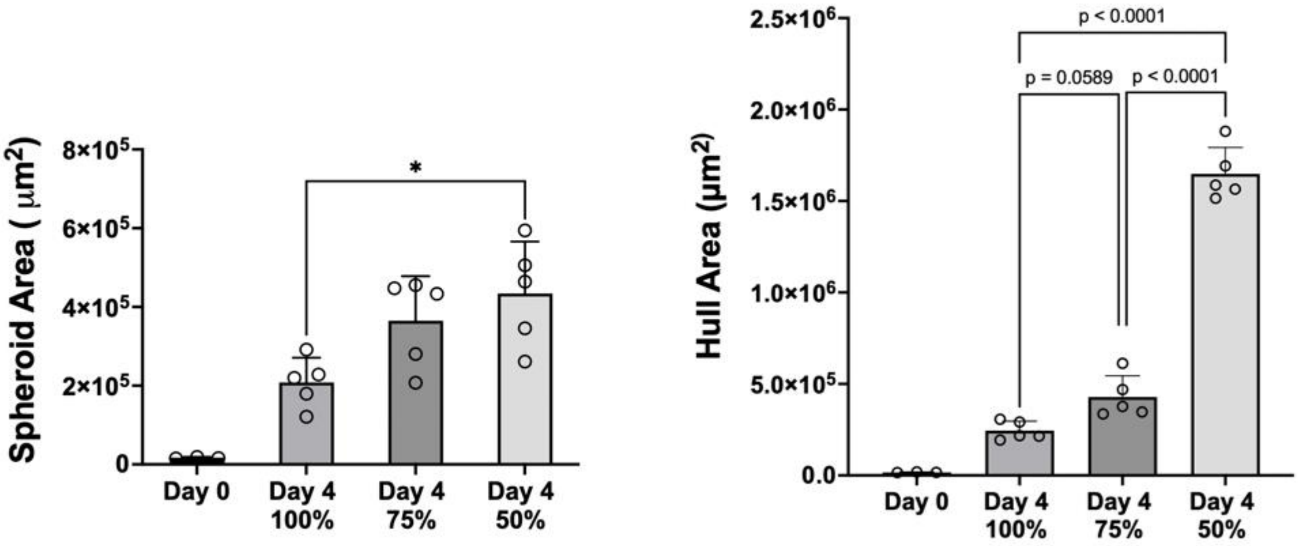

Figure 3. HUVEC/MSC spheroid infiltration assay. *Top and middle*: microscopy images of spheroids stained with phalloidin (magenta) and DAPI (cyan). *Bottom left:* spheroid area based on actin stain. *Bottom right:* convex hull area of spheroids.

More studies are needed to elucidate and assess the extent to which our scaffolds encourage infiltration, especially under a regenerative context *in vivo.* Current studies are being carried out in collaboration with Dr. Patrick Cottler at UVA, where our scaffolds with varying porosities have been injected and crosslinked subcutaneously in mice. The cellular infiltration and immune populations within the scaffolds will be assessed at 4 weeks post injection.

***In vitro* vascularization using porous granular hydrogel scaffolds:**

In addition to in vivo regeneration, we also wanted to explore the possibility of generating an in vitro vasculature system using granular hydrogels. So far, many 3D in vitro vasculature models are based on vasculogenesis in fibrin-based hydrogels[48-52] and other bulk hydrogels[53-55]. Granular hydrogels, on the other hand, can provide a versatile platform for in vitro studies due to 1) ease of cell incorporation, 2) modularity that allows the incorporation of heterogenous properties, and 3) printability or injectability that allow for easy incorporation of designed chemical gradients and printed channels.

At first, we utilized a co-culture of HUVECs and 3T3 fibroblasts, as co-culture of HUVECs and fibroblasts have been reported to successfully generate vasculature in vitro[50]. However, we quickly realized, from the morphology seen on 2D co-cultures, that growths of 3T3s quickly overtakes that of HUVECs in co-culture, which is somewhat expected as the doubling rate of 3T3 is at least two times faster than HUVECs. 3D co-culture carried out in 100% norHA scaffold showed extensive cell coverage on day 6 (Figure 4). We do not truly know the identity of these cells but posit they are likely fibroblasts. This, however, show cases the possible extensive formation of networks even in 100% scaffolds.

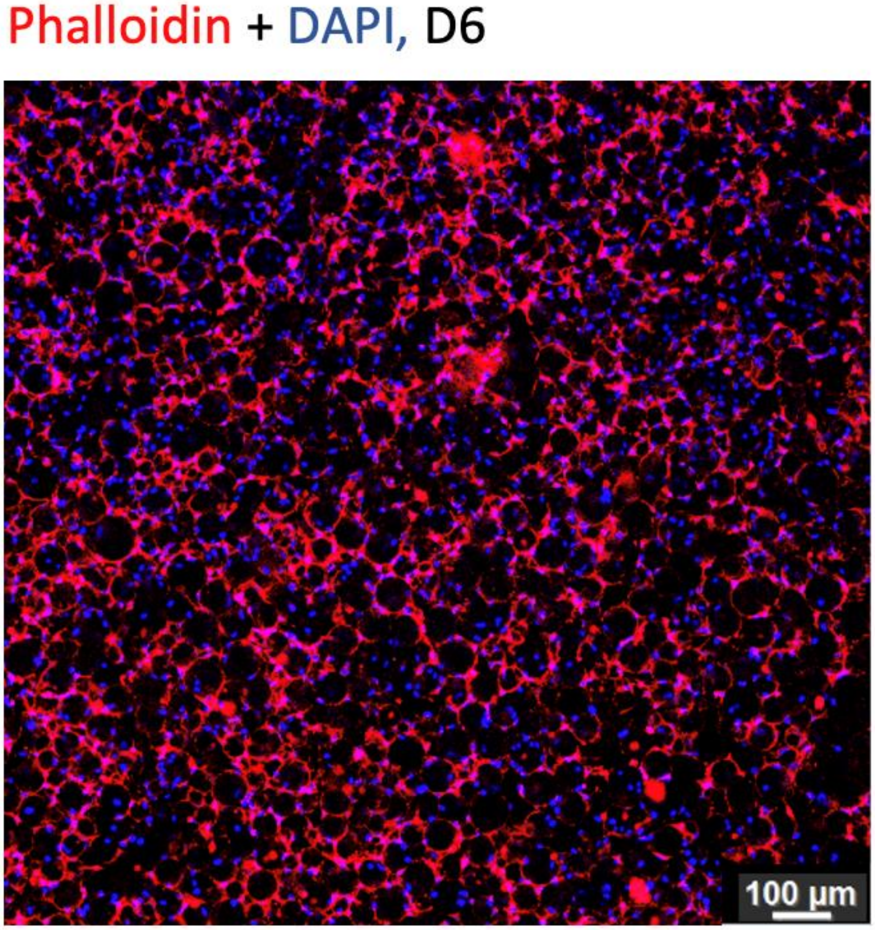

Figure 4. Actin and nuclear stain of HUVECs and 3T3 co-culture in a 100% norHA scaffold on day 6

We then switched to a co-culture of RFP-HUVECs and human bone marrow mesenchymal stromal cells (MSCs), a slower-growing cell type which have also shown success in generating *in vitro* vasculature under co-culture conditions[52]. A 5:1 co-culture of HUVECs to MSCs at a total density of 5 million cells per milliliter of scaffold was carried out in 100% norHA scaffolds only. To further encourage vascularization, we also supplemented the media with an addition of 50ng/mL VEGF-165. Some of the cultures were carried out for >20 days. However, in contrast to the extensive connections formed in the 3T3-HUVEC co-culture, we observed no formation of network-like structures over the period (Figure 5), and the addition of VEGF did not seem to have a meaningful impact in this system. Additionally, HUVEC cells seem to regress after day 14, with less cells in the field of vision by day 16 and day 20.

These results suggest that the inherent porosity from packed scaffolds were not enough to encourage in vitro vasculogenesis. We replicated the experimental conditions of in vitro vascularization using fibrin hydrogels[50]; however, the difference may lie in the signaling generated from HUVECs, which are more confined in fibrin gels and need to reorganize their local environment for movement.

By this time, we have tried numerous co-cultures, cell-seeding conditions, and media compositions and nothing seemed to be working. Around that time, however, we started having conversations with Dr. Lakeshia Taite, whose lab had shown the possibility of vasculogenesis on 2D and 3D PEG-based hydrogels using tethered VEGF-mimetic peptides[56-58]. They were able to show that by tethering a QK peptide sequence derived from VEGF onto the hydrogel surface, they can significantly increase vessel-like morphologies and tubule lengths with 2D HUVEC monoculture. This seemed a very promising revenue for us to pursue as cells spread on the 2D surfaces of our HMPs, rather than being encapsulated in a 3D nanomesh network. In collaboration with Dr. Taite's lab, we employed a thiol-PEG-QK molecule. The thiol functionality allowed us to attach PEG-QK to the surface of our norHA-based HMPs via thiol-norbornene reactivity.

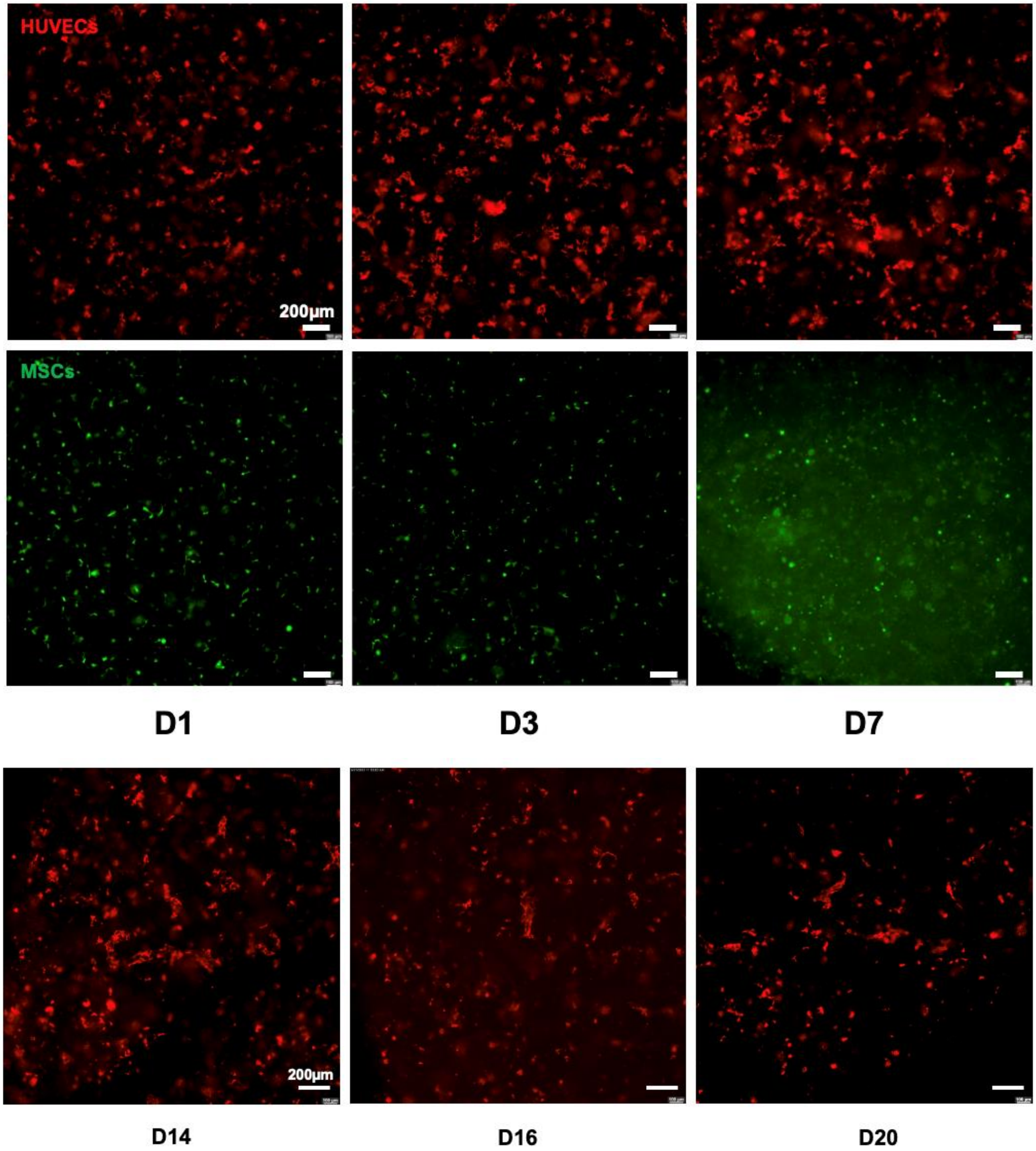

Figure 5. HUVEC/MSC co-culture on various days in 100% norHA scaffold. RFP-HUVECs are shown in red, and MSCs were stained with Celltracker green, which became diffused after one week as the MSCs proliferated. Number of HUVECs per field of view decreased observably as they stayed in culture longer.

To further increase the chances of *in vitro* vascularization, 75% norHA scaffold was chosen based on its positive response in our cell growth experiment, we think it represented the best balance of porosity and cellular growth (Figure 2). Additionally, we increased the total cell density to 11 million cells per milliliter of scaffold, with 10:1 HUVECs to MSCs ratio, and supplemented with the culture media with an additional 5% fetal bovine serum.

In vitro vascularization using 75% QK-tethered norHA scaffold with the condition mentioned above encouraged HUVEC spreading and yielded connecting networks. As shown in Figure 6, we start to identify large scale network formation around day 15 under brightfield microscopy. Compared to the sparse populations of HUVECs seen in norHA scaffolds (Figure 5), as culture time increased in QK-tethered scaffold, we were able to discern more cells among the particles and the change from individual cells to connected cells spread across the imaging field (Figure 6).

The scaffolds were cultured to 30 days to observe network stability as well as scaffold stability. The last brightfield image taken at day 25 is shown in Figure 7. We qualitative observe even more cells within the scaffold that appear to take up much of the interstitial space. CD31 staining on day 30 showed extensively interconnected CD31 positive cells in our scaffold. Figure 7 shows a representative max projected image of cell growth within the first 50 μm of our scaffold. We did notice; however, the cell density drops off at 50–100-μm depths (Figure 7). This could be due to cellular migration toward the surface where more nutrients are readily available, as well as due to exposure to small shear forces in the media during culture that enhanced proliferation. In another replicate scaffold with unintentionally uneven topology, we observed that the cells formed macrostructures reminiscent of tubules. However, we cannot conclude that structures or vasculature were truly formed without staining for markers such as VE-cadherin and functional testing.

This is, however, a promising start to elucidating the parameter needed for vasculogenesis in vitro. Notably, the stability of the scaffold and the number of cellular growths was tremendous. Especially compared to our previous results in 100% norHA scaffolds, the cell growth was quantitatively and qualitatively different.

I want to disclaim here that our findings in vascularization, though promising, are preliminary. Many further studies are needed to elucidate the formation of vasculature in granular hydrogels. Additionally, some of the data presented in the first part of this section precedes all cell culture studies presented in the prior sections of this chapter, the lack of comparison between groups is a result of continuously improving cell culture optimizations. For example, the early experiments using 100% norHA scaffols should be repeated with the updated protocol to make them truly comparable to our current groups. Further work should be done to elucidate the important parameters including porosity, tethered ligands (and lack thereof), cell seeding density, optimal co-culture cell types, and culture media. We believe that being able to reproducibly generate vasculature in our system will shed light on granular hydrogel design and the implications of pore characteristics. A successful in vitro vasculature system using the versatile granular hydrogels platform could also prove useful for mechanistic studies in vascular biology. And finally, QK-peptide-tethered HMPs can be used as an in vivo scaffold that encourages vascularization, as similar work has been done on QK-tethered PEG hydrogels.

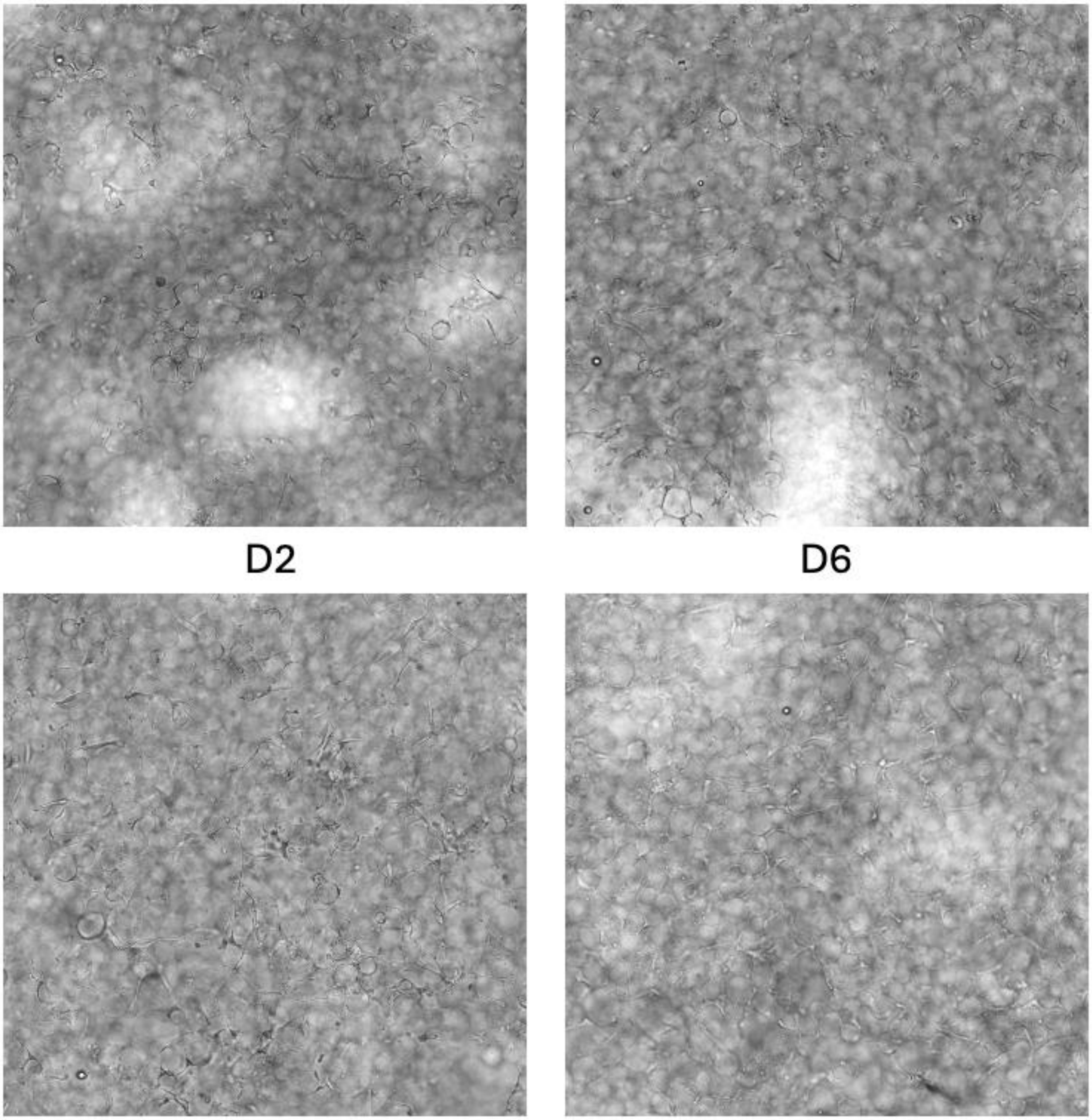

D2

D6

D12

D15

Figure 6. HUVEC/MSC co-culture in 75% norHA, QK-tethered scaffold on various days. BF images are shown here where network formation can be qualitatively discerned.

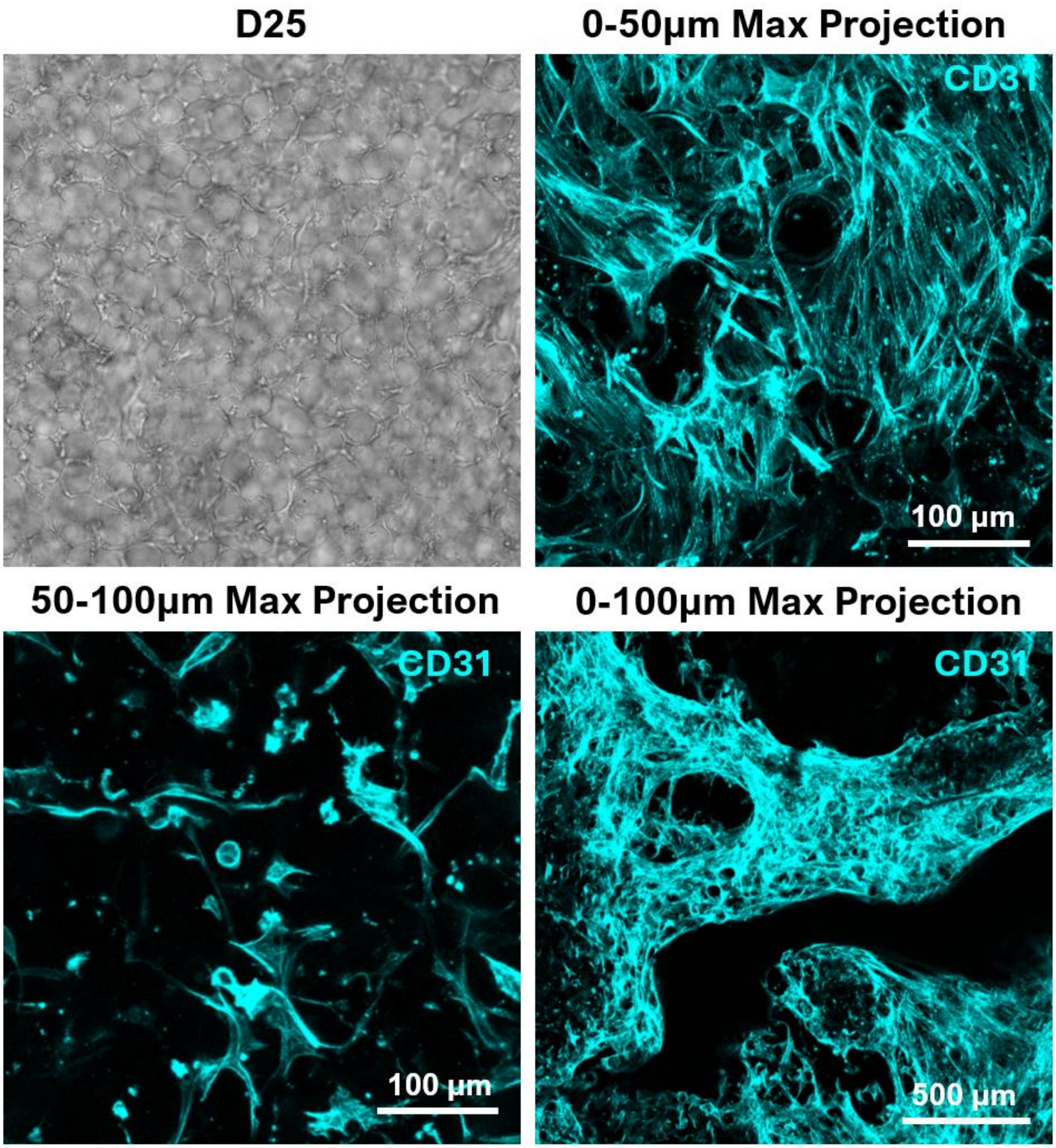

Figure 7. HUVEC/MSC co-culture in 75% norHA, QK-tethered scaffold on day 25 (Top left BF image) and day 30 (rest of the images).

Materials and Methods

HUVECs culture in granular hydrogel scaffolds

HUVECs (Lonza) were expanded first in TC flasks using EBM-2 media with the standard supplement kit (Lonza). HUVECs used in this experiment were kept between P4-P8. To generate various scaffold compositions, norHA HMPs and gelatin HMPs were mixed at 100:0, 75:25, or 50:50 volume ratios. Sterile filtered 10mM LAP in PBS and 162 mM DTT in PBS were added to adjust the final concentration to 1mM LAP and 2mM DTT. The mixtures were centrifuged at 21k rcf for 5 minutes and their supernatant discarded immediately before adding the cells.

HUVECs were detached using 0.05% Trypsin and counted. Number of HUVECs needed to achieve 10 million HUVECs per mL of scaffold were then pelleted by centrifuging at 300 rcf for 3 minutes. The pellet was then resuspended at roughly 100 million cells/mL, and pipette onto the surface of the jammed HMPs. The jammed HMPs were then gently mixed with the cells using a wide-bore pipette tip.

The cell-HMP mixture was then pipetted onto a confocal dish. An isopropanol-sterilized, sigmacote-treated glass slide is placed on top of the jammed cell-HMP mixture so that uniform, 1mm thick shapes are created. UV (365nm filtered) crosslinking was carried out at 10mW/cm2 for 1 minute. The treated glass slide was then removed, and the scaffold cultured for 4 days in EGM-2 media. Media change was carried out every 2 days.

Staining and imaging of HUVECs

After 4 days of culture, scaffolds with HUVECs were fixed in 4% paraformaldehyde (PFA) in PBS in the confocal dish. Permeabilization was then carried out using 0.1% Triton-X 100. Subsequently, blocking with 3% bovine serum albumin (BSA) in PBS was carried out for 2 hours. After blocking, phallodin was mixed with 3% BSA in PBS at 1:600 dilution and added to the fixed scaffold. This step is carried out at 4°C overnight. Phalloidin stained scaffolds were then washed with PBS 3 times, then DAPI in PBS (1:1000 dilution) was added to cells and let sit for 30 minutes. PBS washes were carried out 2 additional times before imaging.

Stained scaffolds hydrated with PBS were imaged using a Leica confocal microscope (Stellaris 5). Whole scaffolds or randomly selected regions were imaged using a 10x objective. All regions were imaged at 5 μm z-direction increments, for a total of 100 μm depth. The images were analyzed in FIJI. Cell number was analyzed based on DAPI-positive nuclei, and cell area was analyzed based on phalloidin positive areas. Statistical analysis was carried out in PRISM. One-way ANOVA with parametric assumption was used for all groups concerned in this experiment.

HUVEC/MSC spheroid culture in granular hydrogel scaffolds

HUVECs were cultured as described above in TC flasks. MSCs (donated by Dr. Ross Marklein and his team) were cultured in MSC basal media with the standard supplement kit (ATCC). HUVECs and MSCs P4-8 were used in this experiment. To from the spheroids, AggreWell-400 templated agarose microwells were first fabricated. HUVECs and MSCs were detached and mixed at a 2:1 number ratio and seeded in agarose microwells at a density of ~2000 cells per microwell. Centrifugation at 100rcf for 2 minutes was carried out to locate the cells to the bottom of the wells. The cells were then cultured for 48h in EGM-2 media to allow for spheroid formation.

Various scaffold compositions were generated as described above. Spheroid were retrieved from the agarose microwells and resuspended in PBS. Spheroids and PBS were then aspirated using a pipette and added to the jammed HMPs at 1:10 (spheroid+PBS : HMPs) volume ratio. The final density averages ~10 spheroids per 100 μL of HMPs. Spheroids and HMPs were then gently mixed and UV crosslinked using the same conditions as described above. The spheroids-loaded scaffolds were then cultured for 4 days in EGM2 media.

Staining using phalloidin and DAPI were carried out identically as described above. Confocal imaging and analysis in FIJI were carried out in the same fashion. Hull area analysis was carried out in FIJI using the “Hull and Circle” add-on. Statistical analysis was carried out in PRISM. One-way ANOVA was used with parametric assumption for spheroid area analysis and non-parametric assumption (Kruskal-Wallis) for Hull area analysis.

HUVEC-MSC co-culture for vasculogenesis in granular hydrogel scaffolds

HUVECs and MSCs were cultured as described above. To generate the scaffold used for vasculogenesis. NorHA HMPs with 2mM RGD and gelatin HMPs were mixed together at 75:25 volume ratio and centrifuged at 21k rcf. After discarding the supernatant, 10mM LAP, 162mM DTT, and 2mM SH-PEG-QK (5200 Da) were added to achieve a final concentration of 1mM LAP, 2mM DTT, and 1mM SH-PEG-QK. Desired numbers of

HUVECs and MSCs were pelleted to achieve a 10:1 HUVEC:MSC number ratio and a final seeding density of 11 million cells per mL HMP scaffold. The pellet was resuspended at ~ 100 million cells per mL then added to the top of the jammed HMPs. After gently mixing in the cells, UV crosslinking was carried out as described above. Cell culture in EGM2 was carried out for 30 days, with media changes every 2-3 days.

Staining was carried out similarly, with the addition of primary CD31 (rabbit with human reactivity) and donkey normal serum for blocking. Primary CD31 antibody was allowed to react overnight. Then, phalloidin and secondary antibody (donkey anti-rabbit) with fluorophore conjugation were added to the fixed scaffold and allowed to react overnight again. The rest of the staining procedure remained unchanged. Confocal imaging was carried out using a Leica confocal microscope (Stellaris 5). Entire scaffolds or select regions were imaged with 100 μm depth.

Final words:

I hope I have adequately conveyed my scientific journey to you so far. If I were to quickly summarize my PhD: it started from a deep dive into material chemistry and the bottom-up manipulation of single cells, then moving towards the development of a biomaterial scaffold as a top-down approach to influence cell behavior. We have showcased our scaffold system as a novel strategy to enable and extend the already broad possibilities of granular hydrogel scaffolds. I hope that this technology proves fruitful to the field of biomaterials, as well as towards a deeper appreciation of pore spaces in hydrogels.

For me, PhD – or life in general – is never always sunshine, nor always rain. The failures and struggles are always first to come to mind, but small, and sometimes big triumphs are spread throughout, to be found savored. The biggest triumphs to me, however, are those earned at the end of the struggles. In my almost 6 years at UVA, I have learned a tremendous amount both professionally and personally, from my struggles as well as triumphs. For that, I am grateful. I plan to continue to use my love for science toward contributing to the understandings and solutions for human health. And finally, thank you all for reading this document and being a part of my journey, I cannot express my gratitude enough in words.

References:

1. Seymour, A. J., Shin, S., & Heilshorn, S. C. (2021). 3D Printing of Microgel Scaffolds with Tunable Void Fraction to Promote Cell Infiltration. Advanced Healthcare Materials, 10(18), 2100644.
2. Chiu, Y. C., Cheng, M. H., Engel, H., Kao, S. W., Larson, J. C., Gupta, S., & Brey, E. M. (2011). The role of pore size on vascularization and tissue remodeling in PEG hydrogels. Biomaterials, 32(26), 6045–6051.
3. Jiang, B., Waller, T. M., Larson, J. C., Appel, A. A., & Brey, E. M. (2013). Fibrin-loaded porous poly(Ethylene Glycol) hydrogels as scaffold materials for vascularized tissue formation. Tissue Engineering - Part A, 19(1–2), 224–234.
4. Lu, D., Zeng, Z., Geng, Z., Guo, C., Pei, D., Zhang, J., & Yu, S. (2022). Macroporous methacrylated hyaluronic acid hydrogel with different pore sizes for in vitro and in vivo evaluation of vascularization. Biomedical Materials, 17(2), 025006.
5. Wu, X., Huo, Y., Ci, Z., Wang, Y., Xu, W., Bai, B., Hao, J., Hu, G., Yu, M., Ren, W., Zhang, Y., Hua, Y., & Zhou, G. (2022). Biomimetic porous hydrogel scaffolds enabled vascular ingrowth and osteogenic differentiation for vascularized tissue-engineered bone regeneration. Applied Materials Today, 27, 101478.
6. Betz, M. W., Yeatts, A. B., Richbourg, W. J., Caccamese, J. F., Coletti, D. P., Falco, E. E., & Fisher, J. P. (2010). Macroporous hydrogels upregulate osteogenic signal expression and promote bone regeneration. Biomacromolecules, 11(5), 1160–1168.

7. Itl, A. I., Ylnen, H. O., Ekholm, C., Karlsson, K. H., & Aro, H. T. (2001). Pore diameter of more than 100 μm is not requisite for bone ingrowth in rabbits. Journal of Biomedical Materials Research, 58(6), 679–683.
8. Karageorgiou, V., & Kaplan, D. (2005). Porosity of 3D biomaterial scaffolds and osteogenesis. Biomaterials, 26(27), 5474–5491.
9. Sicchieri, L. G., Crippa, G. E., de Oliveira, P. T., Beloti, M. M., & Rosa, A. L. (2012). Pore size regulates cell and tissue interactions with PLGA–CaP scaffolds used for bone engineering. Journal of Tissue Engineering and Regenerative Medicine, 6(2), 155–162.
10. Pruett, L. J., Kenny, H. L., Swift, W. M., Catallo, K. J., Apsel, Z. R., Salopek, L. S., Scumpia, P. O., Cottler, P. S., Griffin, D. R., & Daniero, J. J. (2023). De novo tissue formation using custom microporous annealed particle hydrogel provides long-term vocal fold augmentation. Npj Regenerative Medicine 2023 8:1, 8(1), 1–10.
11. Schaeffer, C., Pfaff, B. N., Cornell, N. J., Salopek, L. S., Shan, S., Viyar, J., Omesiete, W., Griffin, D. R., Cottler, P. S., & Degeorge, B. R. (2020). Injectable Microannealed Porous Scaffold for Articular Cartilage Regeneration. Annals of Plastic Surgery, 84(6), S446–S450.
12. Amini, A. R., Adams, D. J., Laurencin, C. T., & Nukavarapu, S. P. (2012). Optimally porous and biomechanically compatible scaffolds for large-area bone regeneration. Tissue Engineering - Part A, 18(13–14), 1376–1388.
13. Bai, F., Wang, Z., Lu, J., Liu, J., Chen, G., Lv, R., Wang, J., Lin, K., Zhang, J., & Huang, X. (2010). The correlation between the internal structure and

vascularization of controllable porous bioceramic materials in vivo: a quantitative study. Tissue Engineering. Part A, 16(12), 3791–3803.

14. Fan, C., & Wang, D. A. (2015). Effects of permeability and living space on cell fate and neo-tissue development in hydrogel-based scaffolds: a study with cartilaginous model. Macromolecular Bioscience, 15(4), 535–545.
15. Zeng, L., Yao, Y., Wang, D. A., & Chen, X. (2014). Effect of microcavitary alginate hydrogel with different pore sizes on chondrocyte culture for cartilage tissue engineering. Materials Science and Engineering: C, 34(1), 168–175.
16. Choi, S.-W., Zhang, Y., MacEwan, M. R., Xia, Y., Choi, S., Zhang, Y., MacEwan, M. R., & Xia, Y. (2013). Neovascularization in Biodegradable Inverse Opal Scaffolds with Uniform and Precisely Controlled Pore Sizes. Advanced Healthcare Materials, 2(1), 145–154.
17. Madden, L. R., Mortisen, D. J., Sussman, E. M., Dupras, S. K., Fugate, J. A., Cuy, J. L., Hauch, K. D., Laflamme, M. A., Murry, C. E., & Ratner, B. D. (2010). Proangiogenic scaffolds as functional templates for cardiac tissue engineering. Proceedings of the National Academy of Sciences of the United States of America, 107(34), 15211–15216.
18. Sussman, E. M., Halpin, M. C., Muster, J., Moon, R. T., & Ratner, B. D. (2014). Porous implants modulate healing and induce shifts in local macrophage polarization in the foreign body reaction. Annals of Biomedical Engineering, 42(7), 1508–1516.

19. Hwang, C. M., Sant, S., Masaeli, M., Kachouie, N. N., Zamanian, B., Lee, S. H., & Khademhosseini, A. (2010). Fabrication of three-dimensional porous cell-laden hydrogel for tissue engineering. Biofabrication, 2(3), 035003.

20. Somo, S. I., Akar, B., Bayrak, E. S., Larson, J. C., Appel, A. A., Mehdizadeh, H., Cinar, A., & Brey, E. M. (2015). Pore Interconnectivity Influences Growth Factor-Mediated Vascularization in Sphere-Templated Hydrogels. Tissue Engineering - Part C: Methods, 21(8), 773–785.

21. Teng, W., Long, T. J., Zhang, Q., Yao, K., Shen, T. T., & Ratner, B. D. (2014). A tough, precision-porous hydrogel scaffold: Ophthalmologic applications. Biomaterials, 35(32), 8916–8926.

22. Griffin, D. R., Weaver, W. M., Scumpia, P. O., di Carlo, D., & Segura, T. (2015). Accelerated wound healing by injectable microporous gel scaffolds assembled from annealed building blocks. Nature Materials 2014 14:7, 14(7), 737–744.

23. Anderson, A. R., Nicklow, E., & Segura, T. (2022). Particle fraction is a bioactive cue in granular scaffolds. Acta Biomaterialia, 150, 111–127.

24. Liu, Y., Suarez-Arnedo, A., Riley, L., Miley, T., Xia, J., & Segura, T. (2023). Spatial Confinement Modulates Macrophage Response in Microporous Annealed Particle (MAP) Scaffolds. Advanced Healthcare Materials, 12(26), 2300823.

25. Ataie, Z., Horchler, S., Jaberi, A., Koduru, S. v., El-Mallah, J. C., Sun, M., Kheirabadi, S., Kedzierski, A., Risbud, A., Silva, A. R. A. E., Ravnic, D. J., & Sheikhi, A. (2024). Accelerating Patterned Vascularization Using Granular Hydrogel Scaffolds and Surgical Micropuncture. Small, 20(8), 2307928.

26. Ataie, Z., Kheirabadi, S., Zhang, J. W., Kedzierski, A., Petrosky, C., Jiang, R., Vollberg, C., Sheikhi, A., Ataie, Z., Kheirabadi, S., Petrosky, C., Jiang, R., Sheikhi, A., Zhang, J. W., Vollberg, C., & Kedzierski, A. (2022). Nanoengineered Granular Hydrogel Bioinks with Preserved Interconnected Microporosity for Extrusion Bioprinting. Small, 18(37), 2202390.
27. Teng, W., Long, T. J., Zhang, Q., Yao, K., Shen, T. T., & Ratner, B. D. (2014). A tough, precision-porous hydrogel scaffold: Ophthalmologic applications. Biomaterials, 35(32), 8916–8926.
28. Chan, N. R., Hwang, B., Ratner, B. D., & Bryers, J. D. (2022). Monocytes contribute to a pro-healing response in 40 μm diameter uniform-pore, precision-templated scaffolds. Journal of Tissue Engineering and Regenerative Medicine, 16(3), 297–310.
29. Chan, N. R., Hwang, B., Mulligan, M. S., Ratner, B. D., & Bryers, J. D. (2024). Porous Precision-Templated 40 μm Pore Scaffolds Promote Healing through Synergy in Macrophage Receptor with Collagenous Structure and Toll-Like Receptor Signaling.
30. Hady, T. F., Hwang, B., Pusic, A. D., Waworuntu, R. L., Mulligan, M., Ratner, B., & Bryers, J. D. (2021). Uniform 40-μm-pore diameter precision templated scaffolds promote a pro-healing host response by extracellular vesicle immune communication. Journal of Tissue Engineering and Regenerative Medicine, 15(1), 24–36.

31. Qazi, T. H., Wu, J., Muir, V. G., Weintraub, S., Gullbrand, S. E., Lee, D., Issadore, D., Burdick, J. A., Qazi, T. H., Muir, V. G., Weintraub, S., Issadore, D., Burdick, J. A., Wu, J., Lee, D., & Gullbrand, S. E. (2021). Anisotropic Rod-Shaped Particles Influence Injectable Granular Hydrogel Properties and Cell Invasion. Advanced Materials, 2109194.

32. Tang, R. C., Shang, L., Scumpia, P. O., & di Carlo, D. (2023). Injectable Microporous Annealed Crescent-Shaped (MAC) Particle Hydrogel Scaffold for Enhanced Cell Infiltration. Advanced Healthcare Materials, 2302477.

33. Riley, L., Cheng, P., & Segura, T. (2023). Identification and analysis of 3D pores in packed particulate materials. Nature Computational Science 2023 3:11, 3(11), 975–992.

34. Chaudhuri, O., Cooper-White, J., Janmey, P. A., Mooney, D. J., & Shenoy, V. B. (2020). Effects of extracellular matrix viscoelasticity on cellular behaviour. Nature, 584(7822), 535–546.

35. Chaudhuri, O., Gu, L., Klumpers, D., Darnell, M., Bencherif, S. A., Weaver, J. C., Huebsch, N., Lee, H. P., Lippens, E., Duda, G. N., & Mooney, D. J. (2016). Hydrogels with tunable stress relaxation regulate stem cell fate and activity. Nature Materials, 15(3), 326–334.

36. Grolman, J. M., Weinand, P., & Mooney, D. J. (2020). Extracellular matrix plasticity as a driver of cell spreading. Proceedings of the National Academy of Sciences, 202008801.

37. Engler, A. J., Sen, S., Sweeney, H. L., & Discher, D. E. (2006). Matrix Elasticity Directs Stem Cell Lineage Specification. Cell, 126(4), 677–689.

38. Majedi, F. S., Hasani-Sadrabadi, M. M., Thauland, T. J., Li, S., Bouchard, L.-S., & Butte, M. J. (2020). T-cell activation is modulated by the 3D mechanical microenvironment. Biomaterials, 120058.

39. Sadtler, K., Wolf, M. T., Ganguly, S., Moad, C. A., Chung, L., Majumdar, S., Housseau, F., Pardoll, D. M., & Elisseeff, J. H. (2019). Divergent immune responses to synthetic and biological scaffolds. Biomaterials, 192, 405–415.

40. Hannan, R. T., Peirce, S. M., & Barker, T. H. (2018). Fibroblasts: Diverse Cells Critical to Biomaterials Integration. ACS Biomaterials Science and Engineering, 4(4), 1223–1232.

41. Liu, Y. J., le Berre, M., Lautenschlaeger, F., Maiuri, P., Callan-Jones, A., Heuzé, M., Takaki, T., Voituriez, R., & Piel, M. (2015). Confinement and Low Adhesion Induce Fast Amoeboid Migration of Slow Mesenchymal Cells. Cell, 160(4), 659–672.

42. Lou, J., Stowers, R., Nam, S., Xia, Y., & Chaudhuri, O. (2018). Stress relaxing hyaluronic acid-collagen hydrogels promote cell spreading, fiber remodeling, and focal adhesion formation in 3D cell culture. Biomaterials, 154, 213–222.

43. Park, J. S., Chu, J. S., Tsou, A. D., Diop, R., Tang, Z., Wang, A., & Li, S. (2011). The effect of matrix stiffness on the differentiation of mesenchymal stem cells in response to TGF-beta Biomaterials, 32(16), 3921–3930.

44. Rajagopalan, P., Marganski, W. A., Brown, X. Q., & Wong, J. Y. (2004). Direct comparison of the spread area, contractility, and migration of balb/c 3T3 fibroblasts

adhered to fibronectin- and RGD-modified substrata. Biophysical Journal, 87(4), 2818–2827.

45. Yin, Y., He, X. T., Wang, J., Wu, R. X., Xu, X. Y., Hong, Y. L., Tian, B. M., & Chen, F. M. (2020). Pore size-mediated macrophage M1-to-M2 transition influences new vessel formation within the compartment of a scaffold. Applied Materials Today, 18, 100466.

46. Tylek, T., Blum, C., Hrynevich, A., Schlegelmilch, K., Schilling, T., Dalton, P. D., & Groll, J. (2020). Precisely defined fiber scaffolds with 40 μm porosity induce elongation driven M2-like polarization of human macrophages. Biofabrication, 12(2), 025007.

47. Mehdizadeh, H., Sumo, S., Bayrak, E. S., Brey, E. M., & Cinar, A. (2013). Three-dimensional modeling of angiogenesis in porous biomaterial scaffolds. Biomaterials, 34(12), 2875–2887.

48. Shin, Y., Jeon, J. S., Han, S., Jung, G. S., Shin, S., Lee, S. H., Sudo, R., Kamm, R. D., & Chung, S. (2011). In vitro 3D collective sprouting angiogenesis under orchestrated ANG-1 and VEGF gradients. Lab on a Chip, 11(13), 2175–2181.

49. Shun Zhang, Zhengpeng Wan, & D. Kamm, R. (2021). Vascularized organoids on a chip: strategies for engineering organoids with functional vasculature. Lab on a Chip, 21(3), 473–488.

50. Whisler, J. A., Chen, M. B., & Kamm, R. D. (2014). Control of perfusable microvascular network morphology using a multiculture microfluidic system. Tissue Engineering - Part C: Methods, 20(7), 543–552.

51. Ben-Shaul, S., Landau, S., Merdler, U., & Levenberg, S. (2019). Mature vessel networks in engineered tissue promote graft–host anastomosis and prevent graft thrombosis. Proceedings of the National Academy of Sciences of the United States of America, 116(8), 2955–2960.

52. Lesman, A., Rosenfeld, D., Landau, S., & Levenberg, S. (2016). Mechanical regulation of vascular network formation in engineered matrices. In Advanced Drug Delivery Reviews (Vol. 96, pp. 176–182). Elsevier B.V.

53. Blache, U., Metzger, S., Vallmajo-Martin, Q., Ehrbar, M., Martin, I., & Djonov, V. (2016). Dual Role of Mesenchymal Stem Cells Allows for Microvascularized Bone Tissue-Like Environments in PEG Hydrogels. Advanced Healthcare Materials, 5(4), 489–498.

54. Leslie-Barbick, J. E., Saik, J. E., Gould, D. J., Dickinson, M. E., & West, J. L. (2011). The promotion of microvasculature formation in poly(ethylene glycol) diacrylate hydrogels by an immobilized VEGF-mimetic peptide. Biomaterials, 32(25), 5782–5789.

55. Chen, Y. C., Lin, R. Z., Qi, H., Yang, Y., Bae, H., Melero-Martin, J. M., & Khademhosseini, A. (2012). Functional Human Vascular Network Generated in Photocrosslinkable Gelatin Methacrylate Hydrogels. Advanced Functional Materials, 22(10), 2027–2039.

56. Leslie-Barbick, J. E., Moon, J. J., & West, J. L. (2009). Covalently-Immobilized Vascular Endothelial Growth Factor Promotes Endothelial Cell Tubulogenesis in

Poly(ethylene glycol) Diacrylate Hydrogels. Journal of Biomaterials Science, Polymer Edition, 20(12), 1763–1779.

57. Leslie-Barbick, J. E., Saik, J. E., Gould, D. J., Dickinson, M. E., & West, J. L. (2011). The promotion of microvasculature formation in poly(ethylene glycol) diacrylate hydrogels by an immobilized VEGF-mimetic peptide. Biomaterials, 32(25), 5782–5789.

58. Leslie-Barbick, J. E., Shen, C., Chen, C., & West, J. L. (2011). Micron-scale spatially patterned, covalently immobilized vascular endothelial growth factor on hydrogels accelerates endothelial tubulogenesis and increases cellular angiogenic responses. Tissue Engineering - Part A, 17(1–2), 221–229.